

Thermoelectric Bismuth-related Nanowires Based on Anodic Aluminum Oxide Membranes

Dissertation

zur Erlangung des akademischen Grades

doctor Ingenieurwissenschaften (Dr. –Ing.)

vorgelegt der

Zentrum für Ingenieurwissenschaften

der Martin-Luther-Universität Halle-Wittenberg

Von Jongmin Lee

Geboren am 23. Jan 1977 in Seoul, Südkorea

Gutachter/ in

- 1.
- 2.

Halle(Saale), den 15. Apr. 2009

Contents

I. Introduction

I. 1 Thermoelectric Effect.....	2
I. 2 Improved Thermoelectric Performance of Nanowires.....	3
I. 3 Thermoelectric Materials	5
I. 4 Electrochemical Deposition in Alumina Template.....	6

E. Experimental Procedures: Basics

9

E. 1 AAO Membrane Preparation.....	9
E. 2 Metal (Au) Electrode Preparation	11

Chapter 1

13

Bismuth Telluride Nanowire Growth	13
1. 1 Review of Electrodeposition of Bi ₂ Te ₃ Films and Nanostructures.....	13
1. 2 Introduction to Bismuth Telluride Nanowire Growth	14
1. 3 Experimental Procedures.....	15
1. 4 Results and Discussion	17
1. 5 Conclusions of Chapter 1	25

Chapter 2

27

Bismuth Nanowire Growth with ALD of SiO ₂	27
2. 1 Introduction	27
2. 2 Electronic Band Structure of Bismuth.....	28
2. 3 Transition from Semimetal to Semiconductor.....	31
2. 4 Atomic Layer Deposition	32
2. 5 Experimental Procedures.....	34
2. 6 Results and Discussion	37
2. 7 Conclusions of Chapter 2	43

Chapter 3

44

Annealing Bi ₂ Te ₃ Nanowires for Improving the Crystalline Structure	44
3. 1 Annealing of Bi ₂ Te ₃ Nanowires.....	44
3. 2 Energy-Dispersive X-ray Spectroscopy (EDX)	45
3. 3 Crystalline Structure of Bi ₂ Te ₃ Nanowires	48
3. 4 Conclusions of Chapter 3	51

Chapter 4	52
Optical Characterization of Bi Nanowires.....	52
4. 1 The Preparation for Optical Characterization.....	52
4. 2 Conclusions of Chapter 4	55
Chapter 5	57
Electrical Characterization of Bi ₂ Te ₃ and Bi Nanowires.....	57
5. 1 Electrical Conductivity	57
5. 2 2-Point Measurement for Bi ₂ Te ₃ Nanowire Arrays	57
5. 3 2-Point Measurements for Bi Nanowire Arrays	61
5. 4 2-Point Measurement at a Single Bi ₂ Te ₃ Nanowire.....	64
5. 5 4-Point Measurement of Single Bi ₂ Te ₃ Nanowire	69
5. 6 Conclusions of Chapter 5	71
Chapter 6	72
Measurement of the Seebeck Coefficient in Bi ₂ Te ₃ Nanowires	72
6. 1 Seebeck Coefficient.....	72
6. 2 Preparation for the Measurement of Seebeck Coefficient.....	74
6. 3 Seebeck Coefficient Variations for Bi ₂ Te ₃ Nanowires	75
6. 4 Conclusions of Chapter 6	78
Chapter 7	81
Rough Bi ₂ Te ₃ Nanowires Fabrication in Pulse-anodized AAO.....	81
7. 1 Fabrication of Pulse-anodized AAO Membrane	82
7. 2 Fabrication of Rough Bi ₂ Te ₃ Nanowires	83
7. 3 Conclusions of chapter 7	85
Summary	86
Bibliography	90
Lebenslauf	100
Acknowledgements	101

I. Introduction

Nowadays the long-term ‘energy crisis’ is getting a serious issue and is closely tied to environmental problems. The growing world population, rising standard of living and the limited supply of fossil fuels, which accounts for 85% of the world’s energy needs, have an impact on global energy security, economics and climate.^[1, 1] In addition to energy conservation and increased efficiency in the use of energy, affordable, reliable and sustainable energy production, especially renewable energy, will be essential to enhance global peace and growing our economies while at the same time ensuring that we pass on a clean planet to future generations. Until now, fossil fuels, such as coal and oil etc., are still consumed too much. Furthermore, the environmental problem due to the increasing demands for fossil fuels became so serious that the need for research on alternative energy sources is becoming urgent.

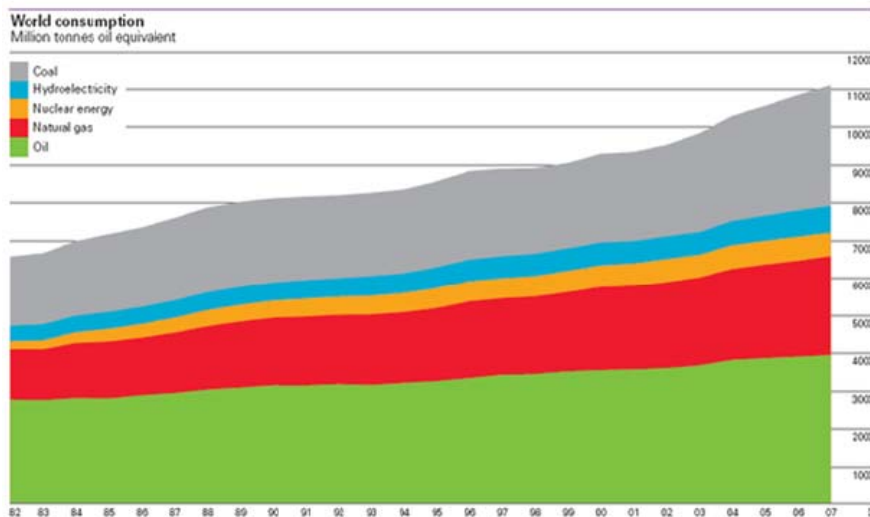


Figure I.1 A trend to global consumption of energy for the last 2.5 decades (in million tons of oil equivalent) [BP Statistical Review of World Energy 2008, 18. JUNE. 2008]

Many candidates have been considered as possible replacement of fossil fuels, such as hydroelectricity, solar energy, wind energy, geothermal energy and biomass. Among them, thermoelectric energy, which involves the conversion between thermal energy and electrical energy, and provides a method for heating and cooling materials, is expected to play an increasingly important role in meeting the energy challenge of the future. Furthermore, thermoelectric energy systems are supposed to be environmentally friendly and considered as a so-called ‘Green Technology’. Additionally,

thermoelectricity rapidly finds applications like portable refrigerators and electronic component coolers.

I. 1 Thermoelectric Effect

The thermoelectric effect is the direct conversion of temperature difference to electric voltage and vice versa. On the scale of atoms, an applied temperature difference causes a charged carrier in the materials, whether they are electrons or holes, to diffuse from the hot side to the cold one. Finally, this results in a higher charge carrier concentration at the hot end.

The Seebeck effect describes the conversion of a temperature difference directly into electricity. If the temperature difference ΔT between two ends of a material is small, then the thermopower (or Seebeck coefficient) of a material is defined as,^[1, 2] $S = \frac{\Delta V}{\Delta T}$.

If a heat source is provided, the thermoelectric device may function as a power generator, a schematically shown in figure I.2. The heat source will drive electrons in the n-type element toward the cooler region, thus creating a current through the circuit. Holes in the p-type element will then flow in the direction of the current. The current can then be used to power a load, thus converting the thermal energy into electrical energy.

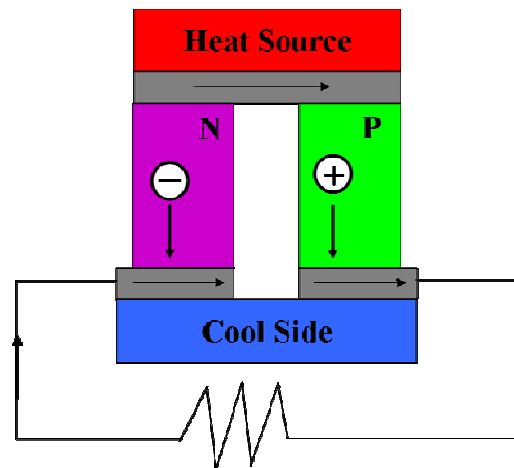


Figure I. 2. The Seebeck effect (thermoelectric generator)

The Peltier effect is the reverse phenomenon of the Seebeck effect. If a current I flows through the circuit, heat is generated at one side and absorbed at the other side. If a power source is provided, the thermoelectric device may act as a cooler, like shown in figure I. 3. Electrons in the n-type element will move opposite to the technical direction

of the current and holes in the p-type element will move in the technical direction of the current, both removing heat from one side of the device.

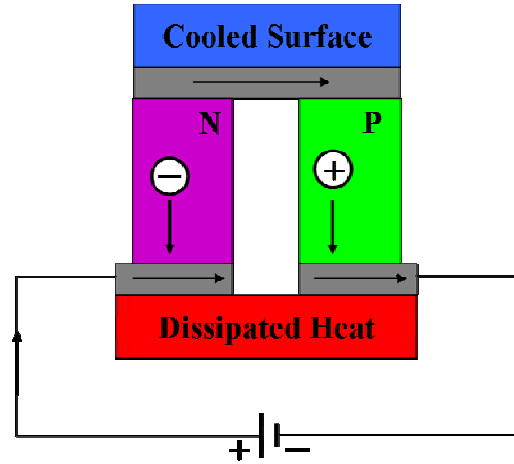


Figure I. 3. The Peltier effect (thermoelectric cooler)

I. 2 Improved Thermoelectric Performance of Nanowires

The efficiency of thermoelectric energy conversion is determined by the thermoelectric figure of merit (FOM), ZT , where T is the absolute temperature and Z is defined as

$$Z = \frac{S^2 \delta}{\kappa} \quad [1.2]$$

S is the Seebeck coefficient, δ is the electrical conductivity and $\kappa = \kappa_e + \kappa_l$ is

the thermal conductivity, which includes contributions from electronic carriers (κ_e) and from the lattice vibration (κ_l). To increase efficiency, it is necessary to increase S and δ as well as to decrease κ at the same time. However, since the quantities S , δ and κ for conventional 3D crystalline systems are interrelated, it is very difficult to control these variables independently so that ZT could be increased. This is because an increase in S normally results in a decrease in δ , and a decrease in δ produces a decrease in the electronic contribution to κ , following the Wiedemann-Franz law.^[1.3] However, if the dimensionality is decreased, the new variable of length scale becomes available for the control of material properties. As the size approaches the nano scale, it is possible to cause a dramatic differences in the density of electronic states, as shown in figure I.4, allowing new opportunities to vary S , δ and κ quasi-independently when the length scale is small enough to give rise to quantum-confinement effects as the number of atoms in certain direction (x , y , or z) becomes small.^[1.4]

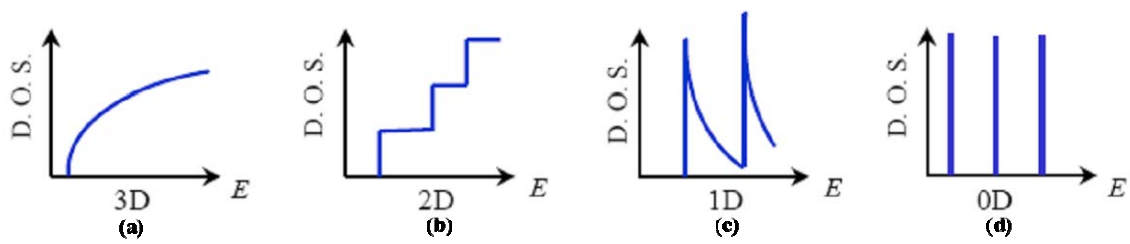


Figure I. 4. Electronic DOS for (a) a bulk 3D semiconductor, (b) a 2 D quantum well, (c) a 1 D nanowire or nanotube and (d) a 0 D quantum dot

Furthermore, the many internal interfaces found in nanostructure could be designed so that the thermal conductivity will be reduced more than the electrical conductivity, based on differences in their respective scattering length.^[1.5] This serves to filter out the low-energy electrons at the interfacial energy barriers and allows the development of nanostructured materials with enhanced ZT, suitable for thermoelectric applications. The descriptive schematic is shown in figure I. 5 below.

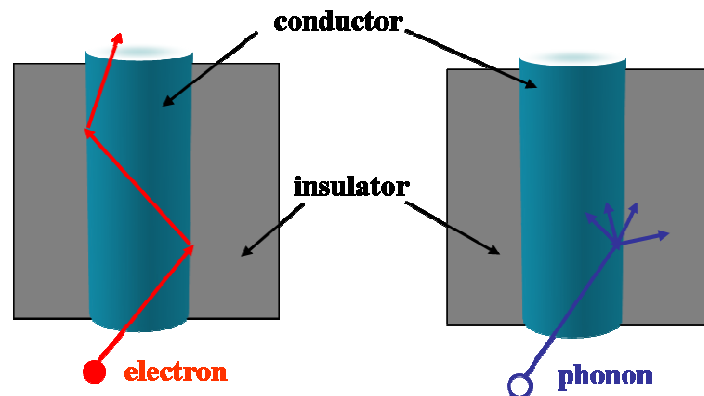


Figure I. 5. Different charge carrier scattering due to high surface to volume ratio effect for low dimensional nanostructures

In conclusion, reduced dimensionality offers one strategy for increasing ZT relative to bulk values.^[1.6,7] Low dimensionality provides: (1) a method for enhancing the density of states near E_f , leading to an increase of the Seebeck coefficient, (2) opportunities to take advantage of the anisotropic Fermi surface in multi-valley cubic semiconductors, (3) opportunities to increase the boundary scattering of phonons at the barrier-well interfaces, without as large an increase in electron scattering at the interface, (4) opportunities for increased carrier mobility at a given concentration when quantum confinement conditions are satisfied, so that modulation doping and δ -doping can be utilized.^[1.8]

I. 3 Thermoelectric Materials

Electrical conductivity is one of the parameters that is used in the classification of thermoelectric materials. The electrical conductivity is a reflection of the charge carrier concentration. All three parameters which make up the figure of merit are functions of carrier concentration. The electrical conductivity increases with an increase in carrier concentration as shown in figure I. 6.^[1,4] while the Seebeck coefficient decreases, with the power factor ($\alpha^2 \cdot \delta$) maximizing at a carrier concentration of around $10^{25}/\text{cm}^3$. The electronic contribution to the thermal conductivity κ_e , which in thermoelectric materials is generally around 1/3 of the total thermal conductivity, also increases with carrier concentration. All this indicate that the figure of merit is maximal at carrier concentrations which correspond to semiconducting materials.

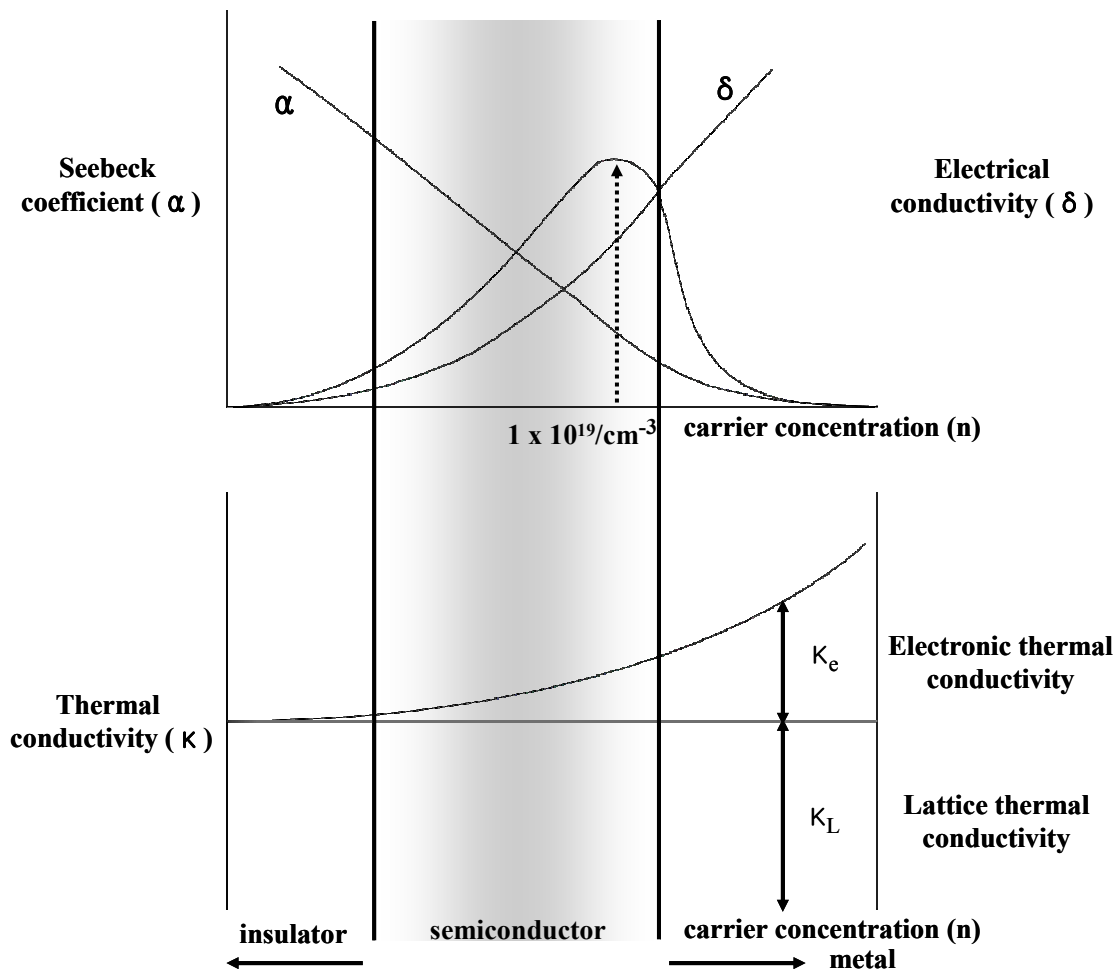


Figure I. 6. Schematic of electrical conductivity, Seebeck coefficient, power factor and thermal conductivity as a function of carrier concentration

Established thermoelectric materials can be divided into three groups. Each depends on the operating temperature range, as shown in figure I. 7. Alloys based on bismuth with antimony (Sb), tellurium (Te) and selenium (Se) are referred to as low-temperature materials. These are the materials commercially employed in thermoelectric refrigeration and have no serious contenders for applications over this temperature regime. The intermediate temperature range is the regime of materials based on lead telluride (PbTe) while thermoelements employed at the highest temperatures are fabricated from silicon (Si)-germanium (Ge) alloys and operate up to 1300K.^[1.4]

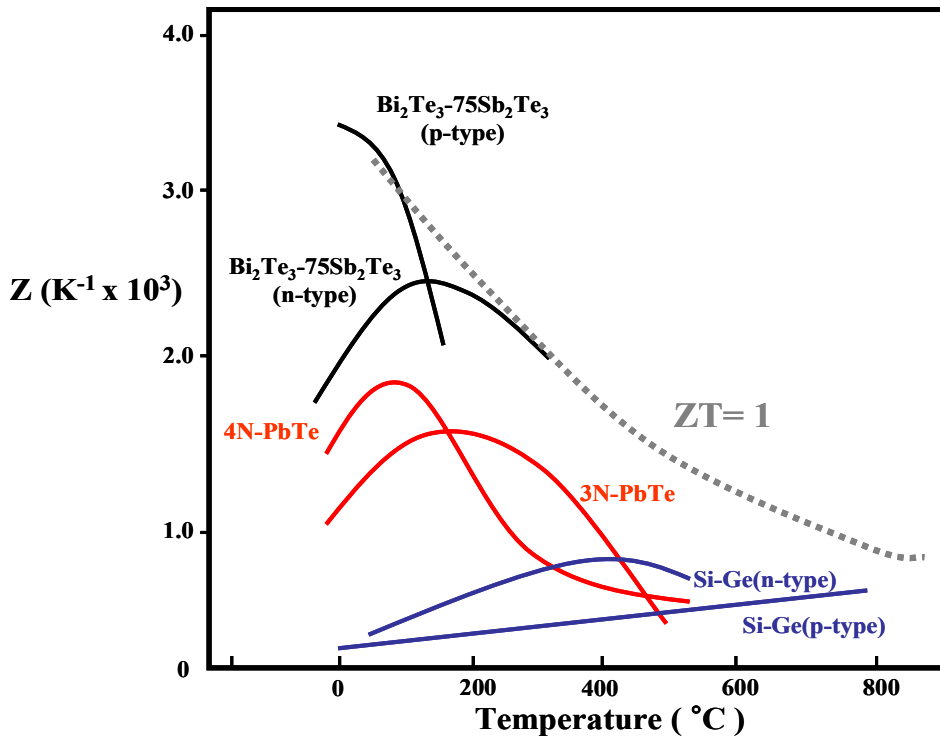


Figure I. 7. Performance of the established thermoelectric materials dependence on the Temperature

Among them, Bi-related materials show relatively higher figures of merit ($ZT \approx 1$ at room temperature). Therefore, Bi-related materials, especially Bi_2Te_3 , are widely used for thermoelectric coolers even though a ZT exceeding 3 is needed in order for a cooler to compete in terms of efficiency with a compression cooling device such as a chlorofluorocarbon (CFC)-based refrigerator.^[1.6] In addition, one material with very high potential in fundamental research has been bismuth (Bi) for many years due to the high Seebeck coefficient of the Bi L-point electron carriers.^[1.7]

I. 4 Electrochemical Deposition in Alumina Template

The most prevalent and versatile method of fabricating thermoelectric nanowires is their synthesis in porous templates. A variety of appropriate template structures have been reported. The most prominent systems are ion-track-polymer membranes,^[1.9] macroporous silicon,^[1.10] diblock-copolymer membranes^[1.11] and ordered porous alumina-oxide membranes.^[1.12] However, polymer based template has a disadvantage of poor thermal stability at 200°C and limited thickness (2~3µm) depending on the material. In particular, the fabrication of anodic aluminum oxide (AAO) template is well developed. This AAO membranes offer good mechanical, chemical (against acid) and thermal stability as well as tunable pore dimensions over a wide range of diameters (~20 to 200 nm) and length (>100 µm).

Many types of synthesis approaches for the preparation of thermoelectric materials have been reported previously, such as pressure injection,^[1.13] vapor-phase deposition,^[1.14] metal organic chemical vapor deposition,^[1.15] hot wall epitaxy,^[1.16] sputtering,^[1.17] and cyclic electrodeposition.^[1.18] Among the directly templated approaches, electrochemical deposition is one of the most popular techniques to fabricate nanowires of metals and intermetallic compounds.^[1.19] It offers the advantages of cost efficiency, rapid deposition rate, relatively easy tuning ability of the nanowire stoichiometry, and uniform growth.^[1.20] Up to now, three different electrodeposition techniques have been applied to the fabrication of thermoelectric Bi₂Te₃ nanowire arrays: galvanostatic,^[1.21] potentiostatic^[1.22] and pulsed electrodeposition.^[1.20]

In this thesis, thermoelectric bismuth and bismuth telluride nanowires are fabricated based on anodized aluminum oxide (AAO) membranes as a template by electrochemical deposition, especially pulsed electrodeposition in bismuth telluride nanowires. Bismuth telluride nanowires are annealed at different temperatures for improving the crystalline structure of nanowires after the fabrication of nanowires in AAO as an approach to the enhancement of the thermoelectric figure of merit ZT though it finally turned out that an increased Seebeck coefficient is not observed and the electrical conductivity can not be measured due to an oxide layer covering the nanowires. The thermoelectric properties of bismuth telluride nanowires, which are electrical conductivity and Seebeck coefficient, are characterized. The thermal conductivity of nanowire could not be measured for the nanowires in the porous membranes. The thermal conductivity measurement is essentially required for the investigation of enhanced thermoelectric efficiency which derives from the fabrication of low dimensional thermoelectric materials. However, unfortunately, the efforts for the thermal conductivity measurement of nanowire arrays or single nanowires are extremely high (microstructure platform

with effective lithographical preparation steps + nanowire positioning and contacting (single nanowire) and thin film type of measurement (nanowire arrays with alumina matrix by 3 Omega method) at present technology that the thermal conductivity of the nanowire can not be measured in this thesis. This is caused by the low thermal conduction contrast between the nanowires and the alumina matrix due to the 10% porosity of anodic aluminum oxide (AAO) membrane (the overall thermal conductivity is the function of alumina template with porosity and nanowires themselves following the equation,^[1,23]

$$k_{\text{tot}} = k_{\text{AAO}} \cdot (1 - \Phi) + k_{\text{nanowire}} \cdot \Phi. \quad (\Phi = \text{porosity of the template})$$

It should be mentioned that very few groups worldwide managed to measure the thermal conductivity of nanowires.

For the investigation of quantum confinement phenomena of bismuth nanowires due to the size effect, bismuth nanowires with different diameter are fabricated in pore size modified AAO membranes. The pore size was reduced systematically by atomic layer deposition (ALD).

The electrical conductivity for bismuth telluride nanowire arrays and individual nanowire was measured. The optical and electrical characterization for Bi nanowire arrays with different diameter (200, 50 and 30nm) was also performed in order to understand the transition from semimetal to semiconductor.

In the last part of the thesis (chapter 7), the fabrication of rough bismuth telluride nanowires is discussed. It is expected that the roughness can play an important role to reduce the thermal conductivity of nanowires, as reported for rough silicon nanowire.^[1,24] Bismuth telluride nanowires with rough surfaces were fabricated based on pulsed potential anodized alumina membrane, in which the pore diameter was periodically modulated by means of the alternative use of mild and hard anodization.

E. Experimental Procedures: Basics

E. 1 AAO Membrane Preparation

Nanoporous anodic aluminum oxide (AAO) membranes with self-organized hexagonal arrays of uniform parallel nanopores have been used for the growth of bismuth and bismuth telluride nanowire arrays. Prior to anodization of aluminum, aluminum foils with a thickness of 5 mm are electropolished in a mixture solution of perchloric acid (HClO₄) and ethanol (C₂H₅OH) with volumetric ratio 1:3. The undesired aluminum oxide and other contaminated layers deposited onto the aluminum chips are removed via an electropolishing process. The electropolishing is performed with applied voltage of 20 V, which connected to Pt wire counter electrode and Al working electrode, during 4 min.

A cleaned Al foil is anodized in different electrolytes, 0.3M oxalic (H₂C₂O₄) or 1 wt% phosphoric (H₃PO₄) acid. Herein, a two-step anodization^[E.1] is commonly adopted to obtain well-ordered arrays of hexagonal pore structures. Independent of the electrolyte used, the anodic terminal is connected to Al while the cathodic terminal is connected to a platinum wire for the anodization of aluminum. After the first anodization, poorly ordered alumina pore structures formed on Al with different pore diameters depending on the electrolyte used and on the applied voltage. Before the second anodization, alumina membrane has to be selectively etched in a mixture solution of 1.8 wt% H₂CrO₄ and 6 wt% H₃PO₄. Then, the alumina matrix is dissolved leaving the hexagonal texture for the enhanced ordering at the second anodization. The experimental conditions are summarized in the table E.1 below.

Solt'n	Conc.	V [V]	1 st anodization		Chromic acid T[°C]/Time[h]	2 nd anodization	
			T[°C]	Time[h]		T[°C]	Time[h]
H ₂ C ₂ O ₄	0.3 M	40	7~8	24	45 / 15	2	10
H ₃ PO ₄	0.5 wt	195	0.5	2~3	45 / 15	-	-
	1.0 wt %	195	1.5	21~22		1.5	10

Table E.1. Two-step anodization conditions used

As summarized in the table, anodization is performed under constant voltage since the interpore distance is strongly related to the applied voltage ($D_{ip}=2.5nmV^{-1}$).^[E.2] Figure E.

1 shows a top surface view of AAO membranes prepared by two-step anodization in 0.3 M oxalic (A) and phosphoric (B) acid. The pore diameter and interpore distance of the left and the right image are about 50 and 200 nm as well as 100 and 500 nm, respectively.

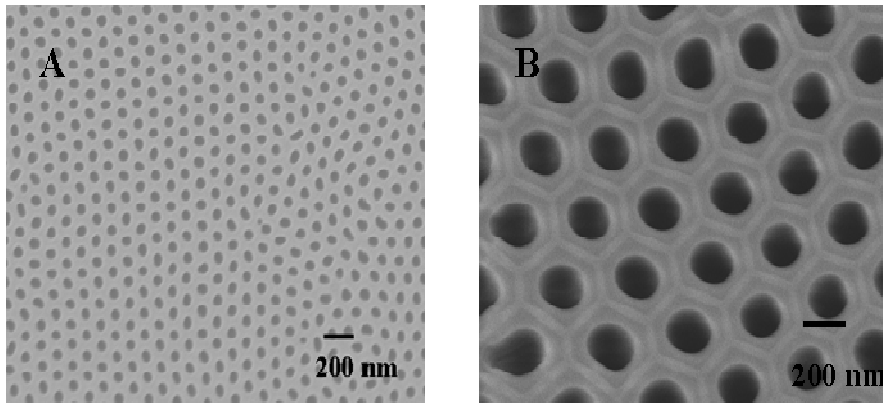


Figure E. 1. Top surface view after two-step anodization from an Al_2O_3 pore structure formed in 0.3M oxalic (A) and 1 wt% phosphoric acid (B)

After the 2nd anodization of aluminum, it is difficult to electrochemically fill the pores with thermoelectric nanowires since the bottom of the AAO is naturally blocked by a barrier layer. Therefore, it is necessary to open the barrier layer. Here, a step-wise voltage reduction method is selected, even though several methods were previously reported.^[E.3] The step-wise voltage reduction is based on field-assisted chemical dissolution of a barrier layer. The barrier layer thickness can be reduced by lowering the anodization voltage. As the anodization voltage is reduced to a sufficiently low value, an effective removal of the barrier layer occurs and detachment of AAO from the Al chip can be achieved. A voltage reduction is followed by a slow recovery of corresponding current, during which the barrier layer is thinned by the formation of new branched pores with a size and spacing appropriate to the reduced voltage. Typically, the voltage reduction is carried out by progressively stepping down the initial voltage down to < 0.05 V in negative increments of 5% of the existing voltage as shown in figure E. 2.

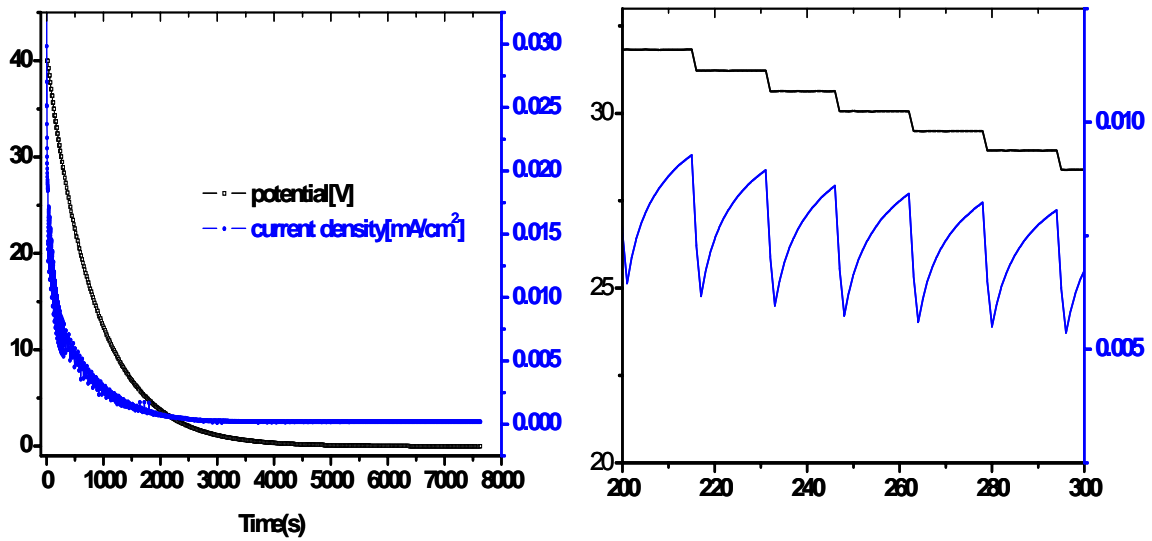


Figure E. 2. Current and voltage behavior of AAO prepared in 0.3 M oxalic acid during step-wise voltage reduction process

The AAO membranes often still stick to the Al chips after the completion of the step wise voltage reduction process. For the complete separation from the Al substrate, immersion of the AAO membrane into an etchant with stronger dissolving power for alumina can facilitate an isolation of the AAO membrane. Typically, 5 wt% phosphoric acid has been used as an appropriate etchant at room temperature for 5~10 min. On the other hand, this process leads to a pore widening, in particular partial dissolution or even destruction of the AAO membrane for long time immersion into an etchant can occur. Released AAO membranes are a nanochannel structure with both sides open. These free standing AAO membranes are ready for their application as a template for the growth of thermoelectric bismuth or bismuth telluride nanowires after the deposition of a metal electrode of the bottom of AAO membranes.

E. 2 Metal (Au) Electrode Preparation

After the barrier layer has been opened, a metal layer is fabricated by sputtering and electrodeposition at the bottom of the AAO membrane. Au is selected as a metal electrode. Au is sputtered at 20 mA power for 150 s by a conventional sputter and subsequently electrodeposited by galvanostatic electrodeposition at a $1\text{mA}/\text{cm}^2$ current density from aqueous Au electroplating solution (Aurura 5000). The overall procedure of AAO membrane and metal electrode fabrication procedure is illustrated in figure E.3.

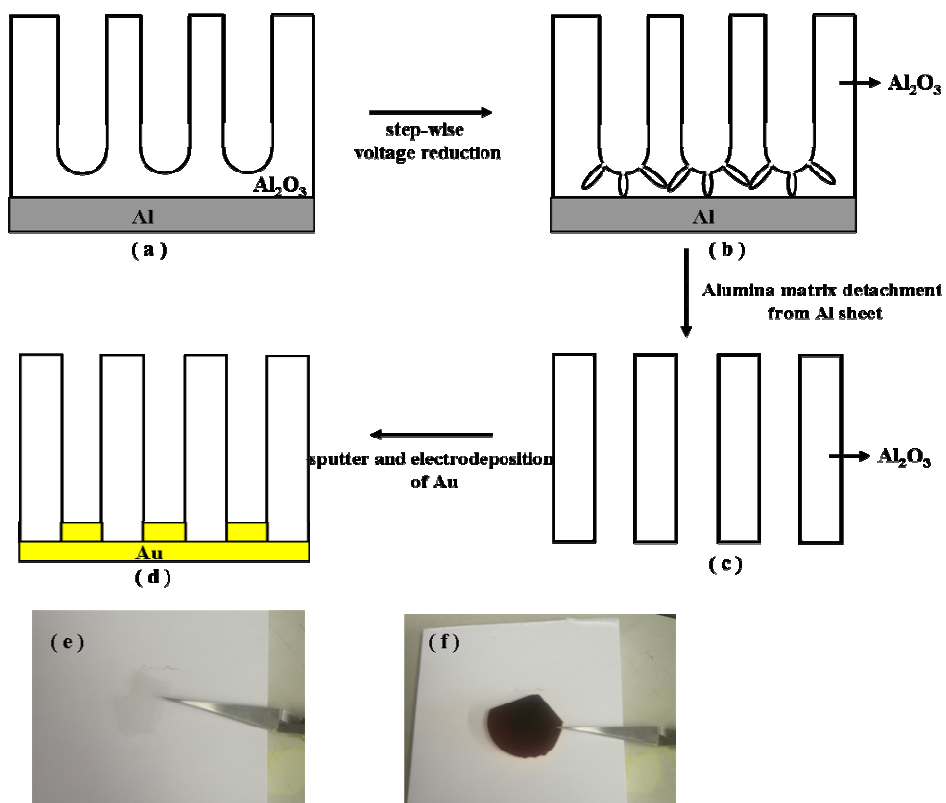


Figure E. 3. Schematic diagram of overall fabrication procedure of AAO membrane and Au electrode (a-d). (e) Nanochannel structured AAO membrane detached from Al substrate, (f) Au electrode fabricated on AAO membrane by sputter and electrodeposition

Chapter 1

Bismuth Telluride Nanowire Growth

In this chapter our experimental results on the growth of bismuth telluride nanowires will be presented. The crystalline structure of electrochemically deposited nanowires is demonstrated depending on the electrodeposition type, such as galvanostatic, potentiostatic and pulsed electrodeposition with different relaxation (or off) time. Thermoelectric characterization will be discussed in chapters 4, 5 and 6.

1. 1 Review of Electrodeposition of Bi_2Te_3 Films and Nanostructures

Electrodeposition of Bi_2Te_3 has mostly been carried out from acidic nitric baths. Takahashi et al first investigated the electrodeposition of Bi_2Te_3 thin films on Ti sheets, correlating the deposition conditions and film composition.^[1.1,2] Magri et al.^[1.3] and Michel et al.^[1.4,5] later improved the Bi_2Te_3 electrodeposits by controlling the deposition potential and electrolyte concentration. Whether Bi_2Te_3 films showed a Bi-rich or a Te-rich nature, depends on the applied potential. Other bismuth telluride thin film studies include those of Titters et al.^[1.6] who reported the galvanostatic electrodeposition of Bi_2Te_3 films onto nickel substrates from nitric acid electrolyte. Only n-type (Te-rich) semiconductors were observed under the experimental conditions.

Bi_2Te_3 nanowires have been almost exclusively electrodeposited by templated-directed

techniques, and in most cases using the deposition conditions from thin film investigations. The applied potentials have been shown to depend upon the electrolyte concentration and material of the seed layer. Prieto et al.^[1.7] and Sander et al.^[1.8] investigated the potentiostatic electrodeposition of Bi_2Te_3 nanowires. The nanowires were deposited at -0.46V vs. Hg/HgSO_4 (sat. K_2SO_4). Approximately 80% of the pores were filled by Bi_2Te_3 nanowires. A more thorough investigation of the influence of mass transport on electrodeposition of Bi_2Te_3 nanowires into alumina templates was conducted by Wang et al.^[1.9] by means of a rotating disk electrode. The nanowires were deposited potentiostatically and the rotation rate varied from 400 to 1400 rpm. They found that mass transport of electrolytes into alumina templates of high aspect ratio (more than 3000) played a significant role in determining the composition of nanowires. Zhang's group^[1.10] extended their pulsed electrodeposition method to fabrication of Bi_2Te_3 nanowires with anodized alumina. As-deposited nanowires were highly oriented with $\{015\}$ planes along the growth direction. The composition was close to the stoichiometric composition.

Finally, Menke et al.^[1.11,12] reported the fabrication of Bi_2Te_3 nanowires without an alumina template by using cyclic electrodeposition. They synthesized the nanowires by the step edge selective electrodeposition on highly oriented pyrolytic graphite (HOPG) surface. The applied potential program, referred to as cyclic electrodeposition/stripping, consisted of three steps: (1) mild oxidation of the basal plane step edges on a piece of HOPG at $+0.8\text{V}$ (vs. SCE) for 5s, (2) nucleation of Bi_2Te_3 nanoparticles along the oxidized step edges at -0.60V for 5 ms, (3) co-deposition of Bi_2Te_3 and excess bismuth during a cathodic potential scan from $+0.3$ to -0.05V , and subsequent stripping of excess bismuth during an anodic potential scan from -0.05 to $+0.30\text{V}$, producing stoichiometric Bi_2Te_3 deposits.

1. 2 Introduction to Bismuth Telluride Nanowire Growth

Many candidate thermoelectric materials have been investigated, such as Bi, $\text{Bi}_{1-x}\text{Sb}_x$, $\text{Bi}_{2-x}\text{Sb}_x\text{Te}_3$, and $\text{Bi}_2\text{Te}_{3-y}\text{Se}_y$. Thin films grown by various techniques have been reported previously.^[1.13-15] Similarly, nanowire arrays fabricated by various techniques have been reported, too.^[1.16-19] Among these various thermoelectric materials, bismuth telluride (Bi_2Te_3) and its derivative compounds are very attractive candidates for thermoelectric applications near room temperature.

Many syntheses for the preparation of thermoelectric materials have been reported

previously. In particular, pulsed electrodeposition offers the advantage of uniform growth of Bi_2Te_3 nanowires. This homogeneous growth of Bi_2Te_3 nanowires in the pulsed electrodeposition is influenced by the relaxation (off) time of pulsed electrodeposition. Additionally, this method is especially suitable for the uniform growth of nanowires into high aspect ratio nanopores.^[1,20,21]

Another advantage of pulsed electrodeposition is related to its tuning of the crystalline structure compared with DC plating.^[1,22] In pulse plating, since the pulsed current density is usually considerably higher than the corresponding DC density, leading to a higher concentration of atoms on the surface during deposition compared to DC deposition. This results in an increased nucleation rate and therefore in a finer grained structure.^[1,23]

In this chapter, we will discuss the fabrication method of Bi_2Te_3 nanowire arrays in AAO and the relationship between the crystalline structure and electrodeposition method. In particular, the relaxation time length of pulsed electrodeposition and homogeneous growth of Bi_2Te_3 nanowires by pulsed electrodeposition will be discussed, too.

1.3 Experimental Procedures

Prior to the growth of Bi_2Te_3 nanowires, cyclic voltammetry (CV) was employed in order to find an optimum potential for the deposition of Bi_2Te_3 nanowires for potentiostatic and potential pulsed electrodeposition. An Au layer was prepared by galvanostatic plating onto a silver plate (purity 99.9%) for CV measurement. The adsorption and desorption behavior between cations in aqueous electrolyte (Bi^{3+} and HTeO_2^+) and Au layer was determined in the operating potential (-0.9 and 0.9V) and the scan rate was 20mV/s.

The overall procedure of Bi_2Te_3 nanowire fabrication in AAO is described in figure 1.1. Firstly, free standing AAO membranes were prepared after two-step anodization in 0.3M oxalic acid and subsequently a step-wise voltage reduction. In order to grow Bi_2Te_3 nanowire, the Au electrode was coated by conventional sputtering onto the top of the AAO. In addition, the Au electrode with a thickness of 3~5 μm as a working electrode on the top of AAO was subsequently galvanostatically deposited from a Au electrodeposition solution under a cathodic current density of $1\text{mA}/\text{cm}^2$ onto the sputtered Au layer. Bi ions provided from 0.021M $\text{Bi}(\text{NO}_3)_3 \cdot 5\text{H}_2\text{O}$ and 0.03M HTeO_2^+ ions from Te powder (purity 99.999%) were dissolved in 2.75M HNO_3 and the pH of

the electrolyte was adjusted to less than 1 (0.8 ~ 0.9) with HNO₃. The Bi₂Te₃ nanowires were grown by galvanostatic electrodeposition under a cathodic constant current density of 2.5 mA/cm² (abbreviated “gal”), by potentiostatic electrodeposition at an applied potential of +60 mV (abbreviated “pot”) and by potential pulsed electrodeposition at +60 mV with pulse time 5 ms and off time (0 V) 10, 20, 30, and 50 ms, respectively (abbreviated pu 10, pu 20, pu 30, and pu 50). The schematic of the pulsed electrodeposition process is described in figure 1.2.

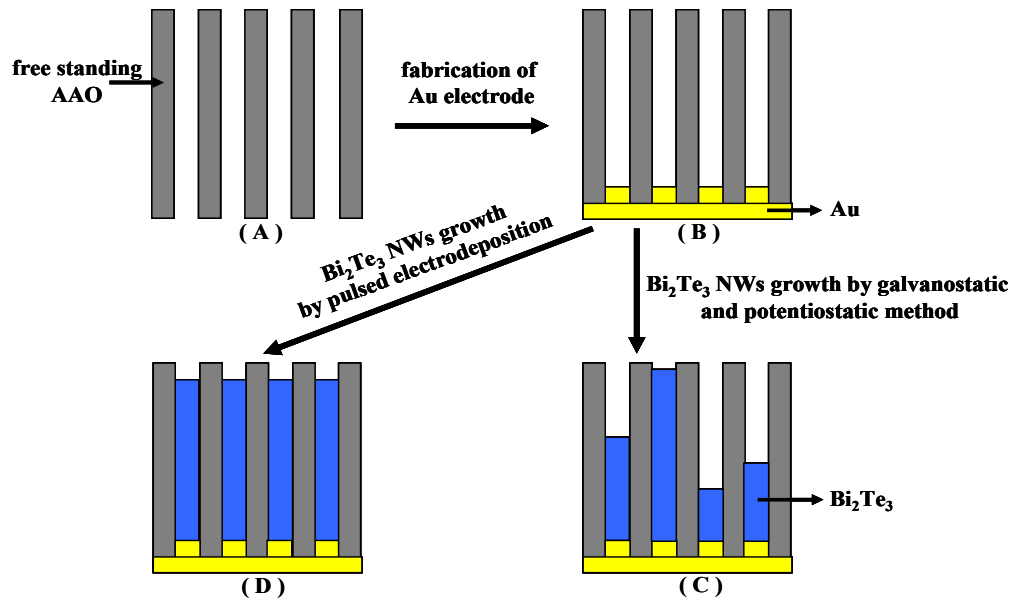


Figure 1.1. Schematic on the fabrication procedure of Bi₂Te₃ nanowires in AAO by electrochemical deposition. (A): free standing as-prepared AAO, (B): preparation of Au electrode, (C) and (D): filling Bi₂Te₃ nanowires in AAO by different electrodeposition types, respectively

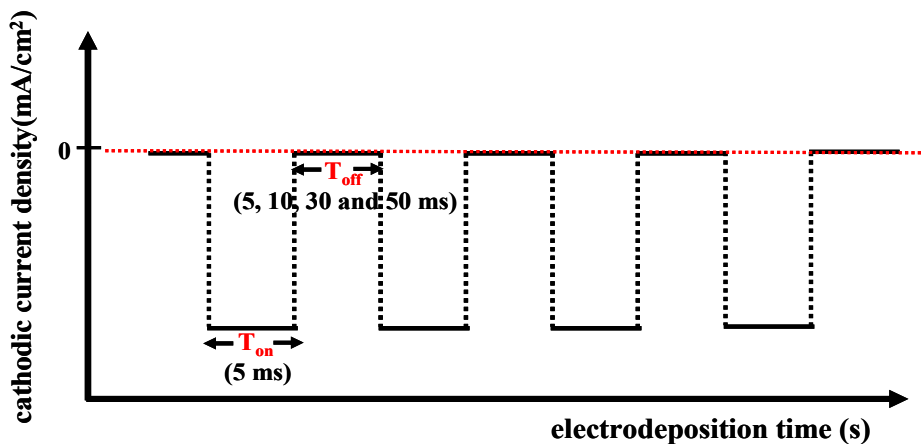


Figure 1.2. Illustration of pulsed electrodeposition with different relaxation (off) time, y axis displays the corresponding current density from applied pulsed potential

The electrodeposition processes were performed with the PAR model 263A potentiostat/galvanostat with a three electrode-configuration, in which a Pt wire was used as a counter electrode and Ag/ AgCl/ KCl (sat'd) as a reference electrode.

X-ray diffractometry (XRD, Philips with Cu K α radiation, $\lambda=1.5406\text{\AA}$) was employed to assess the crystalline structure of the Bi₂Te₃ nanowire arrays after removing the Au layer in an Au etching solution (KI₃). Transmission electron microscopy (TEM), high resolution transmission electron microscopy (HRTEM) and selected area electron diffraction (SAED) also were used to determine the crystalline structure of the nanowire arrays. The AAO matrix and the Au electrode layer were dissolved in 2M NaOH solution and the Au etching solution, respectively and nanowires were purified by DI water several times for TEM observations. A droplet of solution was placed on a carbon grid and allowed to dry at room temperature. Scanning electron microscopy (SEM, JSM 6340F) was used to determine the morphology of Bi₂Te₃ nanowires. An energy dispersive x-ray spectrometer [EDX (JEOL, JEM-2100)] attached to the TEM was used to investigate the composition of the Bi₂Te₃ nanowire arrays.

1. 4 Results and Discussion

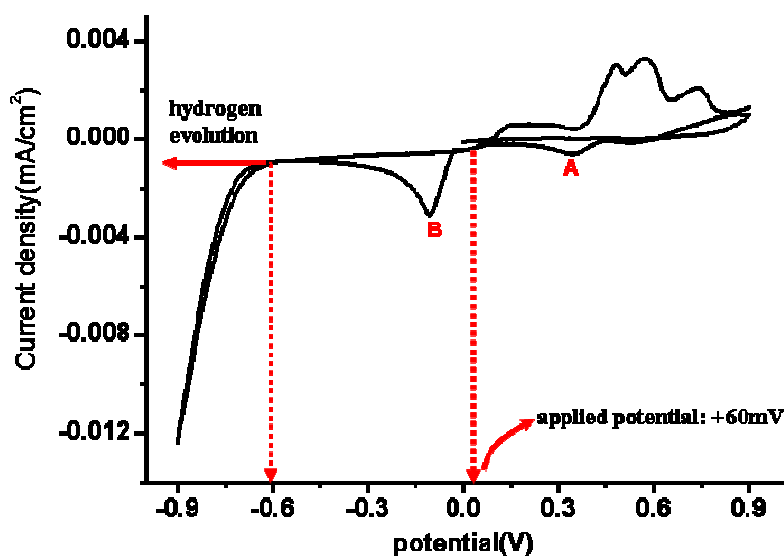
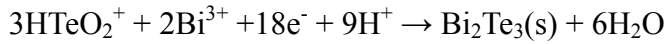
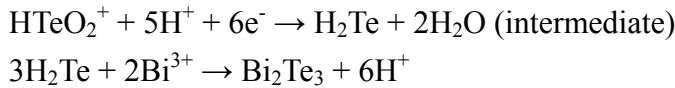


Figure 1.3. Cyclic Voltammetry (CV) of Au working electrode deposited by electrochemical deposition on silver plate in 0.021M Bi(NO₃)₃·5H₂O, 0.03M HTeO₂⁺ and 2.757M HNO₃ solution in the operating voltage between -900 and +900mV. (scan rate: 20mV/s, surface area: 1.13cm², reference electrode: Ag/ AgCl/ KCl(sat'd))

Figure 1.3. shows the cyclic voltammogram (CV) of the $\text{Bi}^{3+}/\text{HTeO}_2^+$ electrolyte between the operating potentials -0.9V and $+0.9\text{V}$. The aim of the CV is to determine an optimized potential at potentiostatic and potential pulsed electrodeposition as well as to investigate the behavior of Bi^{3+} and HTeO_2^+ ions for preventing codeposition.^[1,24] Two reduction peaks (labeled as peak A and B) were observed in the cathodic scan at $+350\text{ mV}$ and -11 mV . Peak A is attributed to the reduction of HTeO_2^+ and Bi^{3+} to Bi_2Te_3 according to the following reaction:



We assume that direct deposition of Bi_2Te_3 occurred instead of the codeposition of $\text{Bi}(\text{s})$ and $\text{Te}(\text{s})$ because of the negative Gibbs free energy of formation of Bi_2Te_3 ($\Delta G_0^f = -899.088\text{ kJ/mol}$). The reduction peak B is attributed to the formation of the Bi_2Te_3 via an intermediate step according to the following reactions.^[1,24]



There is another reduction part at the potential of less than -600 mV , which is due to the onset of hydrogen evolution. When a more negative potential of -600 mV was applied, the Bi_2Te_3 film on the silver plate was floating after electrodeposition due to poor adhesion caused from vigorous hydrogen evolution in the electrolyte. The optimized reduction potential was determined as $+60\text{ mV}$ allowing the continuous growth of Bi_2Te_3 nanowire for potentiostatic as well as for pulsed potential electrodeposition.^[1,25,26]

Figure 1.4(a) shows the schematic structure of Bi_2Te_3 nanowires grown in the AAO membrane. Bi_2Te_3 nanowires were grown from the Au layer in the AAO by galvanostatic, potentiostatic and pulsed electrodeposition. Inhomogeneous nanowire growth was observed in the galvanostatic and potentiostatic electrodeposition methods. Figure 1.4(b), (c) and (d) show the cross-sectional scanning electron micrographs of Bi_2Te_3 nanowire arrays grown with different types of electrochemical deposition. The inhomogeneity of the nanowires grown by galvanostatic and potentiostatic electrodeposition (Δh_{gal} and Δh_{pot} , as shown in figure 1.4(b) and (c)) reached about 45%. In other words, several nanowires that grew faster than others reached the top surface of AAO earlier and formed the overgrown Bi_2Te_3 film. This then prevents the continuous further growth of other nanowires. For uniform nanowire growth, pulsed

electrodeposition is much more effective.

Additionally, figure 1.5(A) shows the corresponding current density profile as the potentiostatic electrodeposition is applied for the growth of Bi_2Te_3 nanowire. The cathodic current density is suddenly increased at approximately 2800 seconds. As outlined before, the nanowires are growing inhomogeneously while the corresponding current from the applied constant potential (+60 mV) is distributed to the every Au electrode until 2800 seconds. As a result, few nanowires grown faster than most other nanowires have reached the top surface of the AAO at that time. Finally from 2800 seconds, onwards this results in the formation of an overgrown Bi_2Te_3 film which prevents further continuous nanowires growth of the still shorter nanowires. The film feature like lettuce shown in figure 1.5(B) is typical Bi_2Te_3 film shape.

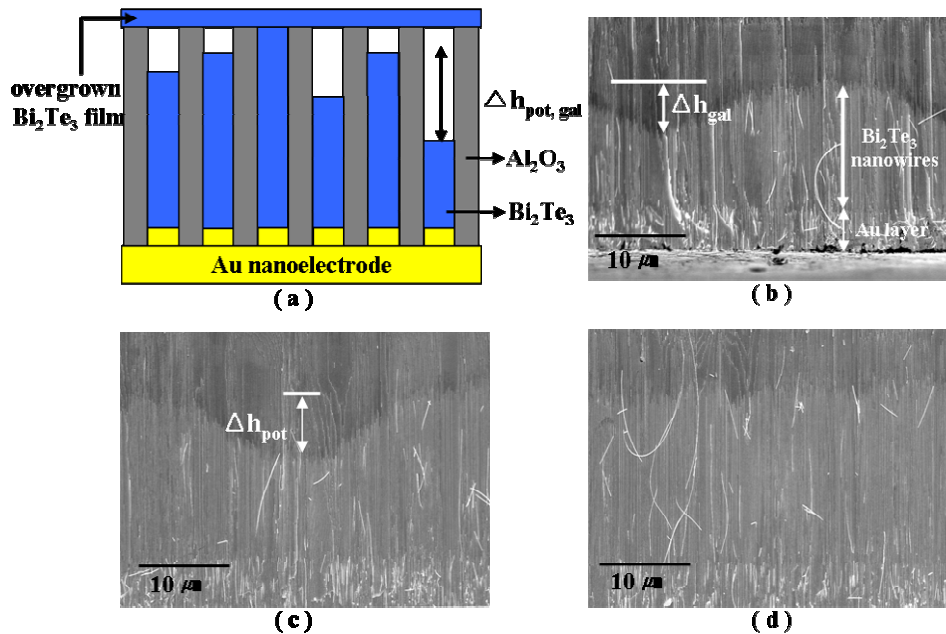


Figure 1.4. Schematic of Bi_2Te_3 nanowire growth (Δh describes an inhomogeneous Bi_2Te_3 nanowires growth in the galvanostatic and potentiostatic methods) in the free standing AAO (a), cross-section of Bi_2Te_3 nanowire arrays grown by the different electrochemical deposition types, respectively. [(b): galvanostatic (2.5 mA/cm^2), (c): potentiostatic (+60 mV), (d): pulsed electrodeposition (off time: 30 ms)]

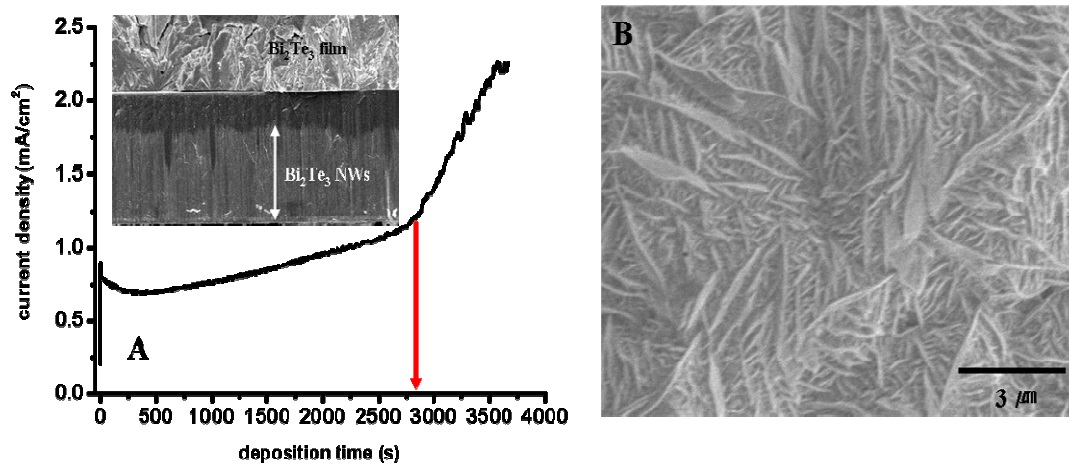


Figure 1.5. (A) Current density profile during potentiostatic electrodeposition for Bi_2Te_3 nanowire growth. Inset SEM image shows the cross-sectional view of Bi_2Te_3 nanowire grown by potentiostatic electrodeposition and (B) top surface view of inset image (A) after 2800 seconds (red arrow)

This observation could be explained by mass transport effects.^[1,22] The limitation of the useful range of pulse conditions due to mass transport effects arises from the depletion of cations at the deposition interface as shown in figure 1.6.

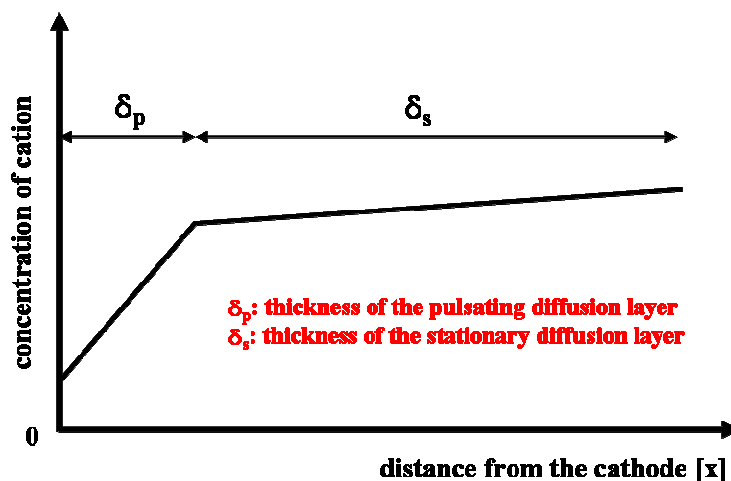


Figure 1.6. A plot illustrating the cation concentration profile in the two diffusion layer during pulsed electrodeposition

In the vicinity of the cathode the concentration pulsates with the pulse current, decreasing during the pulses and relaxing in the interval between them. Thus a pulsating diffusion layer exists close to the cathode. If the duration of the pulse is short, the

diffusion layer does not have time to extend very far into the electrolyte and in particular does not extend to the region where convection takes over the mass transport. Therefore the cation deposited during the pulse must be transported from the bulk of the solution towards the pulsating diffusion layer by diffusion, which means that a concentration gradient also builds up into the bulk of the electrolyte. The thickness of this diffusion layer corresponds essentially to that would be established under the same hydrodynamic conditions in DC electrolysis. Through this outer diffusion layer, cations are also supplied towards the cathode during the off-time and this supply allows the relaxation of the pulsating diffusion layer during the off-time. The outer diffusion layer is essentially stationary.

The two distinct diffusion layers are related to two kinds of limitations. The depletion of the cationic concentration in the pulse plating diffusion layer limits the pulse current density, and the depletion of the cationic concentration in the outer diffusion layer limits the average current density. Since the concentration gradient in the pulsating diffusion layer can be very high, increasing with shorter pulse length, the pulse current density can reach extremely high values without decrease of current efficiency. There is a quantitative relation between the maximum pulse duration as far as the current efficiency is concerned and the pulse current density. This maximum pulse duration is called transition time.^[1.27]

In conclusion, during electrodeposition, the concentration of metal ions (Bi^{3+} and HTeO_2^+) at the cathode interfaces decreases with electrodeposition time. This problem can be improved in the pulsed electrodeposition, as the relaxation time (t_{off}) plays an important role in the recovery and redistribution of the metal ion concentration at the cathode interface during the off-time. In addition, the relaxation time limits the hydrogen evolution occurring at the surface of AAO during electrodeposition.^[1.28]

Figure 1.7 shows the XRD patterns of Bi_2Te_3 nanowire arrays. First of all, no peaks were observed for elemental Bi and Te, indicating that only the Bi_2Te_3 phase is present. Au [111], [200] and [222] orientation peaks are detected due to imperfect removal of the Au electrode layer. One orientation, the [110] peak, dominates in all samples. It is evident that the Bi_2Te_3 nanowire arrays have a highly preferred orientation peak along the [110] axes perpendicular to the bottom of the AAO. Prieto et al. reported that Bi_2Te_3 nanowire arrays grow preferentially in the [110] direction.^[1.7] We used the Harris texture coefficient to describe the degree of preferred orientation quantitatively.^[1.29] The texture coefficient ($\text{TC}_{(\text{hkl})}$) is defined as

$$TC_{(hkl)} = (I_{hkl} / I_{hkl}^0) / \left[(1/N) \sum (I_{hkl} / I_{hkl}^0) \right],$$

where I_{hkl} and I_{hkl}^0 are the relative diffraction intensities of the plane (hkl) in the experimental and standard reference (JCPDS, No.15-0863), respectively. N is the number of reflection faces in the diffraction pattern. If the TC is larger than 1.0, it indicates that the (hkl) plane is a preferred orientation of the crystallites. Table 1.1 summarizes the texture coefficient value obtained for each sample for the (110) plane. As shown in Table 1.1, the value of $TC_{(110)}$ is larger than 1.0 in the pu 50 sample.

Sample	gal (2.5 mA/cm ²)	pot (+60 mV)	pu 10	pu 20	pu 30	pu 50
Texture coefficient	0.77	0.81	0.68	0.82	0.98	1.633

Table 1.1. Harris texture coefficients of various Bi₂Te₃ nanowire arrays grown under different electrodeposition types.

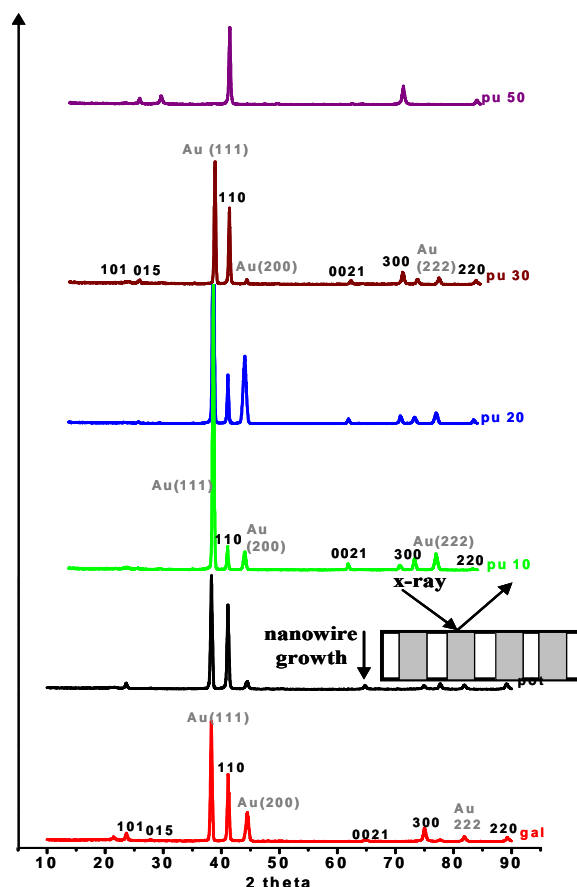


Figure 1.7. XRD patterns of the Bi₂Te₃ nanowire arrays fabricated with different electrochemical deposition types. [gal: galvanostatic (2.5 mA/cm²), pot: potentiostatic (+60 mV), pu 10, 20, 30, and 50: pulsed electrodeposition with relaxation time 10, 20, 30, and 50 ms]

This result shows the (110) plane of the pu 50 sample to be the preferred orientation. Among them, the TC of Bi₂Te₃ nanowires grown by pulsed electrodeposition are relatively larger than those grown by other electrodeposition techniques, indicating that the pulsed electrodeposition is a more effective method to grow a highly oriented crystalline Bi₂Te₃ nanowire arrays into AAO.

Table 1.2 summarizes the value of grain sizes calculated by Scherer's formula. In addition the grain size of every Bi₂Te₃ nanowire grown by different types of electrodeposition displays in the range of pore diameter (50nm). Scherer's equation is expressed as follows:

$$D = \frac{k\lambda}{\beta \cos \theta}$$

where λ is the wavelength of radiation (1.54 Å), k a constant (0.94), β the full width at half-maximum and θ the diffraction angle.^[1,30]

	gal	pot	pu 10	pu 20	pu 30	pu 50
grain size	31.35 nm	29.82 nm	32.42 nm	33.43 nm	32.43 nm	32.44 nm

Table 1.2. Grain size of Bi₂Te₃ nanowire grown by different types of electrodeposition obtained from Scherer's formula (β obtained from XRD data)

Figure 1.8 shows typical TEM micrographs and the corresponding SAED patterns of our Bi₂Te₃ nanowires. The diameter of nanowires (40 nm) is equal to the pore size of the AAO templates. Figure 1.8(a) shows the polycrystalline structure of nanowires grown by the potentiostatic method (a similar image results from the galvanostatic method). The Bi₂Te₃ nanowires grown by pulsed electrodeposition have an almost single crystalline structure consistent with the XRD results. As compared to pulsed electrodeposition with different relaxation times, the crystallinity of Bi₂Te₃ nanowires is enhanced and attains a nearly single crystalline structure with increasing relaxation time. The SAED pattern of pu 30 and 50 samples, especially, indicate the rhombohedral space group ($a = 4.385 \text{ \AA}$ and $c = 30.48 \text{ \AA}$) and a single crystalline structure.

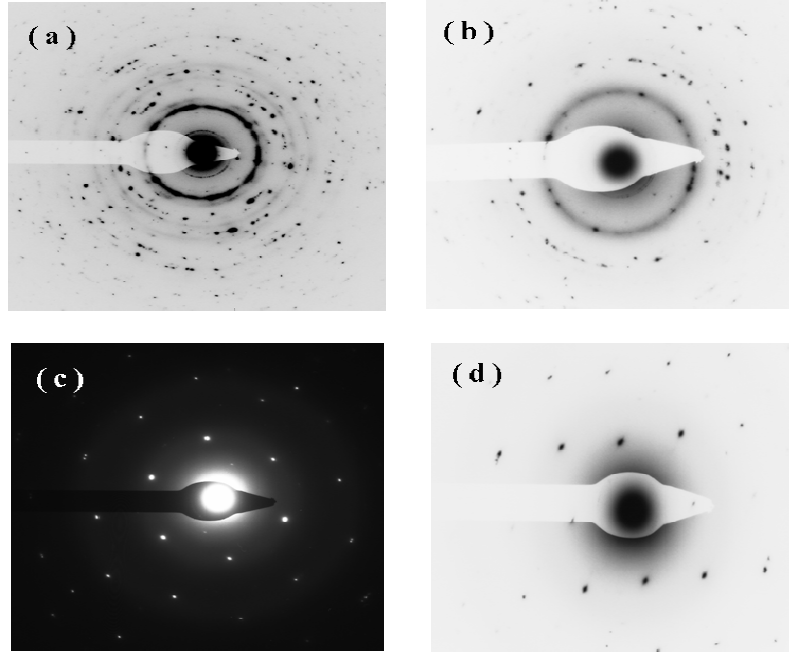


Figure 1.8. Selected area electron diffraction (SAED) patterns of Bi_2Te_3 nanowires prepared by (a) potentiostatic, (b) pulsed electrodeposition with 10 ms (pu 10), (c) with 30 ms (pu 30), and with (d) 50 ms (pu 50) relaxation times, respectively

This phenomenon is attributed to recrystallization during the relaxation time at pulsed electrodeposition.^[1,31] Firstly, the increased pulsed current amplitude as compared to the usual DC amplitude, leads to increased atom concentrations, corresponding to equation [1] to a higher overpotential and therefore, according to equation [2], to higher nucleation rates:

$$\eta_k = \frac{RT}{ZF} \ln \frac{C_{ad}^0}{C_{ad}}, [1],$$

C_{ad}^0 / C_{ad} : atom concentration ratio, η_k = crystallization overpotential

$$V = k_1 \exp\left(-\frac{k_2}{|\eta|}\right), [2]$$

V: nucleation rate, k_1 : proportionality constant and k_2 related to the amount of energy needed for two dimensional nucleation.

In other words, pulsed electrodeposition, when the pulse amplitude is higher than the galvanostatic and potentiostatic electrodeposition amplitude, favors the formation of new crystal nuclei rather than the building-up of existing crystals. In pulse plating, a decrease in the grain size of deposits can therefore be expected. Secondly, the interval

between two pulses, the off-time, has sometimes been called the “dead time”. Evidence has shown, however, that the off time can in fact sometimes be a very active period with respect to crystallization.^[1.32] An increase in off time results in grain growth because of recrystallization during sufficient off-time. The most plausible explanation is that the bigger grains are thermodynamically more stable. If sufficient time is allowed to the system, the most stable state will be reached.^[1.31]

Typical HRTEM images of an individual Bi_2Te_3 nanowire grown by pulsed electrodeposition with 30 and 50 ms relaxation times are shown in Figure 1.9. Interplanar distances of about 0.322 nm and 0.219 nm are visible, consistent with the interplanar distances of the [015] and [110] planes, respectively, confirming the XRD data. In addition, [110] is the preferred orientation direction of Bi_2Te_3 nanowire grown by pulsed electrodeposition with 50 ms relaxation time.

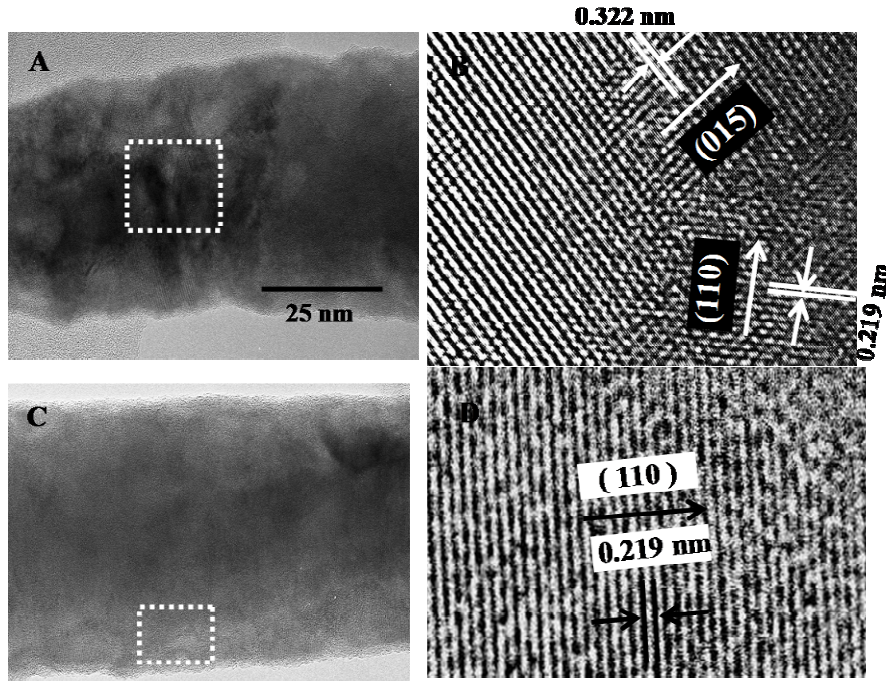


Figure 1.9. HRTEM micrographs of single Bi_2Te_3 nanowires prepared by pulsed electrodeposition with 30 ms (A and B), and 50 ms relaxation time (C and D)

1.5 Conclusions of Chapter 1

Thermoelectric Bi_2Te_3 nanowires were successfully fabricated in well ordered AAO prepared by a two-step anodization process. Galvanostatic, potentiostatic and pulsed electrodeposition types for the fabrication of nanowire arrays were compared. Pulsed

electrodeposition is a very effective method to develop a homogeneous and highly crystalline structure of the Bi_2Te_3 nanowires. Additionally, sufficiently long relaxation times allow to form a high crystallinity due to grain growth attributed to recrystallization. Therefore, Bi_2Te_3 nanowires grown with relatively long relaxation times between deposition pulses, such as a 30 and 50 ms, show a highly preferred orientation along the [110] directions and are close to single crystalline.

Chapter 2

Bismuth Nanowire Growth with ALD of SiO₂

In this chapter bismuth (Bi) nanowires with different diameter are electrochemically fabricated in AAO membranes with reduced pore diameters. The diameter of the pores in AAO membranes is reduced down to 30 nm by atomic layer deposition of SiO₂, leading to the diameter of Bi nanowires. In addition, the crystalline structure and compositional analysis of Bi nanowire with surrounded size-controllable SiO₂ nanotube structure is demonstrated.

2. 1 Introduction

Bismuth is an attractive thermoelectric material because of its very large anisotropy of the three ellipsoidal constant energy surfaces for electrons, their high carrier mobility, the very light effective mass components ($m_{\text{eff}} = 0.001m_e$ to $0.26m_e$ depending on the crystalline direction)^[2.1] that can be exploited for achieving a high electrical conductivity, and the heavy mass components that can be exploited to obtain a heavy density of states (DOS) effective mass since the electrons in bismuth have a highly anisotropic Fermi surface.^[2.2] Since bismuth is a semimetal, it has a low Seebeck coefficient S , because of the approximate cancellation of the electrons and hole contribution to S .^[2.3] It was, however, recognized^[2.4] early on that, if bismuth could be prepared in the form of a semiconductor with either only electron or only hole carriers, it should be a very promising thermoelectric material, as it is discussed elsewhere.^[2.5]

For Bi nanowires with a small enough diameter (less than 50 nm expected in theoretical work)^[2.6] to show quantum confinement effects, the nanowires have to undergo a transition from a semimetal with a small band overlap to a semiconductor with a small indirect bandgap, thus allowing the unusual electronic properties of bismuth to be available in a semiconductor as well as a semimetal.^[2.7] For the quantum confinement to occur, the sample size has to be smaller than the mean free path and de Broglie wavelength of the conduction electrons. Then the electrons are quantum confined and the electronic bands split into subbands.^[2.1] The subbands are split by the energy which is inversely proportional to the effective mass of the charge carriers m and the wire diameter d squared: $\Delta E \approx \hbar^2 \pi^2 / (m * d^2)$.^[2.8] For that reason, Bi is an adequate material for the investigation of quantum confinement effects (QCE) because of its large mean free path (~250 nm at 300K)^[2.9] and an anisotropic small effective mass (varying from 0.001 to 0.26 m_0 , depending on the crystalline direction).^[2.10] In principal, bulk Bi is a semimetal with a very small band overlap energy ($E_g = 38$ and 98 meV at 0 and 300 K, respectively).^[2.11] In Bi nanostructures, the mechanism by which bismuth can be converted into a semiconductor is the size-dependent semimetal-semiconductor transition.^[2.12,13] This transition affects the electronic properties of bismuth significantly, which may be desirable for some applications^[2.14] such as an improvement of thermoelectric efficiency caused by enhanced thermoelectric power (or Seebeck coefficient).

We employed atomic layer deposition of silica nanotubes for the reduction of the nanoscale diameter in porous AAO. Atomic layer deposition is especially suited to nanostructure, since it is controlled by surface chemistry rather than mass transport from the gas phase.^[2.15] The conformal growth resulting from the “self-limiting” nature of the ALD surface chemistry is important for uniform deposition on high aspect ratio structure and porous materials.^[2.16] In addition, ALD is the deposition method of choice to overcome the limits of the minimum pore diameter. The established region of anodization of aluminum reported by now is in the range of 20 to 200 nm (pore diameter) depending on the electrolyte used and the applied voltage.^[E.1] ALD is an appropriate technique to fabricate smaller pore diameters for nanowires deposited in these modified AAO membranes.

2. 2 Electronic Band Structure of Bismuth

Bismuth as a semimetal has a characteristic A15 rhombohedral structure^[2.17] with a band overlap between the conduction band (electron pocket) at the L-points in the

Brillouin zone and the valence band (hole pocket) at the T-point in the Brillouin zone. The locations of the electron and hole carrier pockets are shown in figure 2.1.

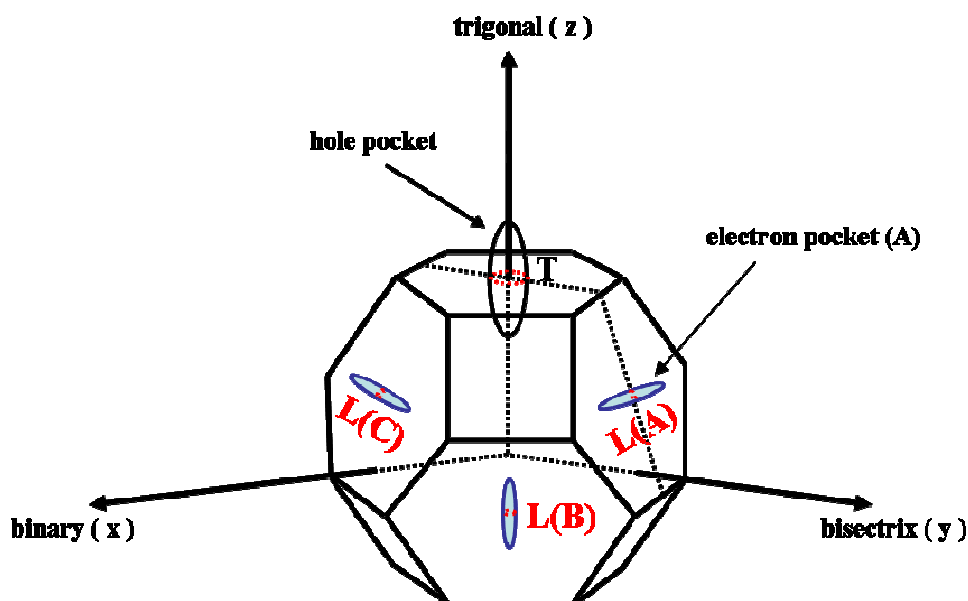


Figure 2.1. The Brillouin zone of bismuth with the Fermi surfaces of the three electron pockets at the L-points and one T-point hole pocket

An important feature of Bi is its highly non-parabolic electronic energy bands at the L-points. These bands are separated by a small energy gap, $E_g = 13.6$ meV at $T=0$ K. It is the strong coupling between these L-point bands that give rise to the non-parabolicity.^[2,18] The L- and T-band structure overlap is shown in figure 2.2.

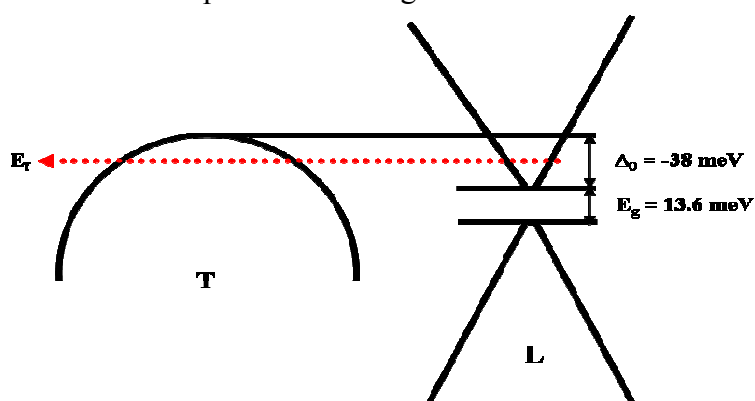


Figure 2.2. An illustration of the bulk Bi band structure at the L-points and T-point near the Fermi energy level, displaying the band overlap Δ_0 of the L-point conduction band and the T-point valence band. The L-point electrons are separated from the L-point holes by a small bandgap E_g

As known in the smallest effective masses of Bi, the effective mass components of the L-point conduction band are $m_{e1}=0.00118 m_0$, $m_{e2}=0.263 m_0$, $m_{e3}=0.00516 m_0$ and $m_{e4}=0.0274 m_{e0}$, where m_0 is the free electron mass.^[2.19] The effective mass components are calculated for nanowires with various crystalline orientations in reference^[2.20,21] and listed in table 2.1. These small mass components lead to very large quantum bound state energies.^[2.18]

As mentioned earlier, the small effective mass of the charge carriers makes it relatively easy to investigate the effects of quantum confinement, since the energy separations between the subbands of the quantum energy levels are large. In Bi, the variation of these energy levels with diameter is large enough to induce a semimetal-semiconductor transition, as will be discussed in the next section.

In addition, concerning the non-parabolic band at the L-point, most of the band parameters in Bi are strongly temperature dependent. The effective masses of the electrons and holes in the L-point bands vary by a factor of 6 between 0 and 300 K, and are given by^[2.22]

$$(m_e(T))_{ij} = \frac{(m_e(T))_{ij}}{1 - 2.94 \times 10^{-3} T + 5.56 \times 10^{-7} T^2} \quad (1)$$

Mass Component		Trigonal	Binary	Bisectrix	(012)	(101)
e- pocket A	m_x	0.1175	0.0023	0.0023	0.0029	0.0024
	m_y	0.0012	0.2659	0.0012	0.0012	0.0012
	m_z	0.0052	0.0012	0.2630	0.2094	0.2542
e- pocket B	m_x	0.1175	0.0023	0.0023	0.0016	0.0019
	m_y	0.0012	0.0016	0.0048	0.0125	0.0071
	m_z	0.0052	0.1975	0.0666	0.0352	0.0526
e- pocket C	m_x	0.1175	0.0023	0.0023	0.0016	0.0019
	m_y	0.0012	0.0016	0.0048	0.0125	0.0071
	m_z	0.0052	0.1975	0.0666	0.0352	0.0526
hole pocket	m_x	0.0590	0.6340	0.6340	0.1593	0.3261
	m_y	0.0590	0.0590	0.0590	0.0590	0.0590
	m_z	0.6340	0.0590	0.0590	0.2349	0.1147

Table 2.1. Effective mass components perpendicular and parallel to the nanowires axis for carrier pockets in Bi nanowires with various crystalline orientations at 77K. This table was taken directly from reference^[2.20,21]

The direct bandgap at the L-point, E_g , does also depend on the temperature.^[2.22]

$$E_g = 13.6 + 2.1 \times 10^{-3}T + 2.5 \times 10^{-4}T^2 \text{ (meV)} \quad (2)$$

Also, the energy band overlap Δ_0 of the bands varies as a function of temperature from -38 meV for a temperature below 80 K to -104 meV at 300 K. The temperature dependence of the band overlap is given by^[2.23]

$$\Delta_0 = -38 - 0.044(T-80) + 4.58 \times 10^{-4}(T-80)^2 - 7.39 \times 10^{-6}(T-80)^3 \text{ [T > 80 K]} \quad (3)$$

(-38 (meV) [T < 80 K])

2.3 Transition from Semimetal to Semiconductor

As bulk bismuth is prepared in the form of nanowires with certain diameter, the energy levels of the electrons confined to a nanowire are quantized leading to a quite different density of states. Hence, the quantized bound state energies can be deduced from Schrödinger's equation for a particle confined by an infinite potential. Therefore the subbands energies are shifted relative to the bulk band edges in Bi by the amount of the quantized bound state energies. For the conduction band the subband energies are shifted up and for the valence band the energy is shifted down. Since the lowest subband is non-zero, this quantization splits the conduction and valence bands apart. For Bi nanowires with a diameter less than 50 nm, this splitting is sufficient to cause a transition from semimetal to semiconductor.^[2.24] As the quantum wire diameter decreases below a critical size, as shown in figure 2.3, a semimetal-semiconductor transition should then occur. In this way the material, which is not a good thermoelectric material in bulk form, could become an attractive low-dimensional thermoelectric material.

To sum up, the reduction of diameter of Bi nanowires is necessary to investigate the quantum confinement effects. However, the pore diameter of pores in AAO anodized from 0.3M oxalic acid is limited to around 40 nm. Consequently, as already explained, ALD plays an important role in the reduction of the diameter of Bi nanowires.

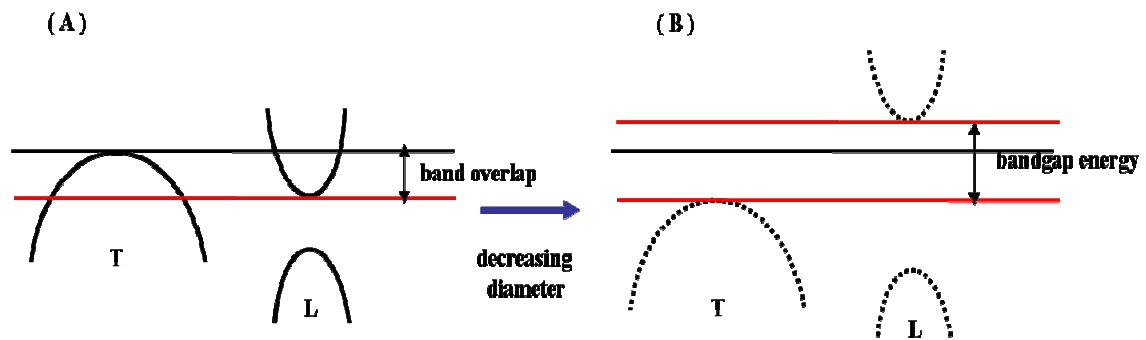


Figure 2.3. Schematic diagram of the quantized band structure of a Bi nanowire. Transition from semimetal to semiconductor as the lowest conduction band at L-point moves up and the highest bands at T point move down in energy due to the reduction of diameter of Bi nanowire. (A); the band structure of Bi nanowire with above 50nm diameter and (B): the band structure of Bi nanowire with below 50nm diameter

2. 4 Atomic Layer Deposition

Atomic Layer Deposition (ALD) is a film deposition technique that is based on the sequential use of self-limiting gas-solid reactions.^[2.25,26] The growth of material layers by ALD consists of repeating the following characteristic four steps;

- (1) A self-limiting reaction of the first precursor (Reactant 1)
- (2) A purge or removal of the non-reacted precursors and the gaseous reaction by-products
- (3) A self-limiting reaction of second precursor (Reactant B) –or another treatment to activate the surface again for the reaction of the first precursor
- (4) A purge or removal

Steps 1~4 constitute one cycle of ALD. Two particularly important characteristics of ALD are that the surface reaction must be complementary and self-limiting. “Complementary” means each of the two precursors must prepare the surface for its reaction with the other vapor, so that the deposition cycles can be repeated. And “self-limiting” means that the amount of material deposited in each of the reaction steps is saturation.^[2.27] Precursor chemistries and process conditions are chosen such that no further reaction takes place other than on the surface which is completely saturated. Surface saturation guarantees the self-limiting nature of ALD. Figure 2.4 shows

schematically the general process of ALD.

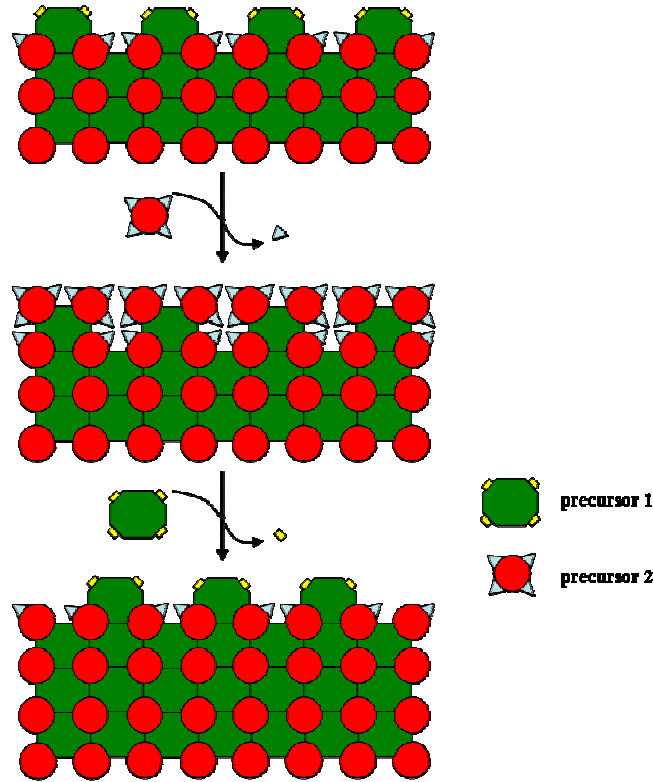


Figure 2.4. Schematic illustration of one cycle of ALD (First, a dose of vapor from precursors 1 is brought to the surface of a substrate onto which a film is to be deposited. Then any excess unreacted vapor of that precursor is purged. Next, a vapor dose of the precursor 2 is brought to the surface and allowed to react, and the excess is also purged)

ALD processes have been developed for manufacturing many types of solid inorganic materials. From the different types of inorganic materials grown by ALD, oxides have been the type most often investigated such as aluminum oxide (Al_2O_3)^[2.28], titanium oxide (TiO_2)^[2.29], iron oxide (Fe_2O_3)^[2.30] and tin oxide (SnO_2)^[2.31]. Among them, silicon dioxide (SiO_2) is chosen for the film deposition in the porous AAO membranes. Aluminum oxide could have been chosen due to the affinity with AAO. However, the thermal conductivity of silicon dioxide [$1.38\text{W}/(\text{m}\cdot\text{K})$] is much smaller than that of aluminum oxide [$36\text{W}/(\text{m}\cdot\text{K})$] and of other oxides (e.g. titanium oxide [$8.4\text{W}/(\text{m}\cdot\text{K})$]).^[2.32] The thermoelectric efficiency [figure of merit] is inversely proportional to the thermal conductivity. In addition a bismuth oxide shell structure sometimes forms on the outer surface of Bi nanowires after release from the AAO membrane.^[2.33] However,

after deposition of an insulating SiO_2 in AAO by ALD, this film might act as an oxidation protection layer.

2.5 Experimental Procedures

The whole process for the electrochemical deposition of Bi nanowires in size-reduced AAO by ALD of SiO_2 is schematically described in figure 2.5.

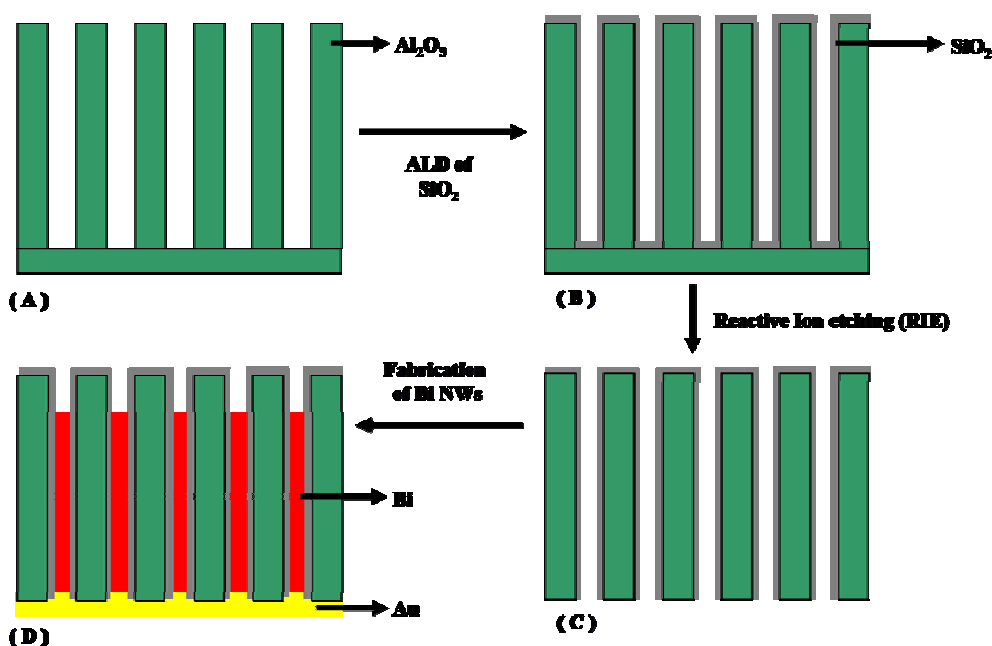


Figure 2.5. Schematic illustration of the fabrication procedure of size reduced Bi nanowires; (A) AAO fabricated by two-step anodization from 0.3 M oxalic acid, (B) ALD of SiO_2 in as-prepared AAO for the reduction of diameter, (C) RIE in order for open the bottom of barrier layer of AAO and SiO_2 nanotube and (D) electrochemical deposition of Bi nanowire by potentiostatic method after the preparation of Au electrode, which is sputtered and electrodeposited

Atomic layer deposition of SiO_2 . AAO membranes with pores of 50 and 200 nm diameter were prepared by two-step anodization, following previously reported procedures,^[E.1] was prepared as a template for ALD of SiO_2 . ALD was carried out in a Savannah 100 system from Cambridge Nanotech operating with Ar as carrier gas. For the ALD of SiO_2 nanotubes in AAO, we followed an established procedure.^[2,34] 3-aminopropyltriethoxysilane, water and ozone as a precursor were employed for the deposition of the SiO_2 layer inside AAO. For ALD, all of the precursors successively

were exposed for the adsorption to the substrate and purged for the removal of excess gas in turns, respectively. One ALD cycle of SiO₂ is summarized in table 2.2.

The first gaseous precursor, 3-aminopropyltriethoxysilane [H₂N(CH₂)Si(OC₂H₅)₃] was introduced in the chamber and chemisorbed to the hydrophilic modified surface (-OH) of the alumina matrix. In the next, water was inserted for the removal of the remaining ethyl arm and recombination as -OH groups, so called ‘hydrolysis’. Subsequently, the aminoalkyl group was eliminated by the introduction of the last precursor, ozone and then purging the by-product, CO₂, NO_x and H₂O.^[2,34] This is the whole reaction sequence of one ALD cycle of SiO₂ as described in figure 2.6.

After the deposition of the SiO₂ nanotubes in AAO, the bottom of the silica tubes and the barrier layer of AAO were removed in a reactive ion etching (RIE) machine (Si220 model, Sentech) using a mixture of CF₄/O₂ at p = 12 mTorr, P = 200W, with corresponding flow rates of 42/5 mL/min. The RIE process lasted about 50 minutes in order to subsequently deposit electrochemically Bi nanowires in the modified AAO membranes.

Time(s)	Designation	silane valve	H ₂ O valve	O ₃ valve	Pump valve
2	silane (pulse)	open	closed	Closed	Closed
30	silane (exposure)	closed	closed	Closed	Closed
20	silane (purge)	closed	closed	Closed	Open
1	water (pulse)	closed	open	Closed	Closed
30	water (exposure)	closed	closed	Closed	Closed
20	water (purge)	closed	closed	Closed	Open
0.2	ozone (pulse)	closed	closed	Open	Closed
30	ozone (exposure)	closed	closed	Closed	Closed
20	ozone (purge)	closed	closed	Closed	Open

Table 2.2. One ALD cycle procedure of SiO₂

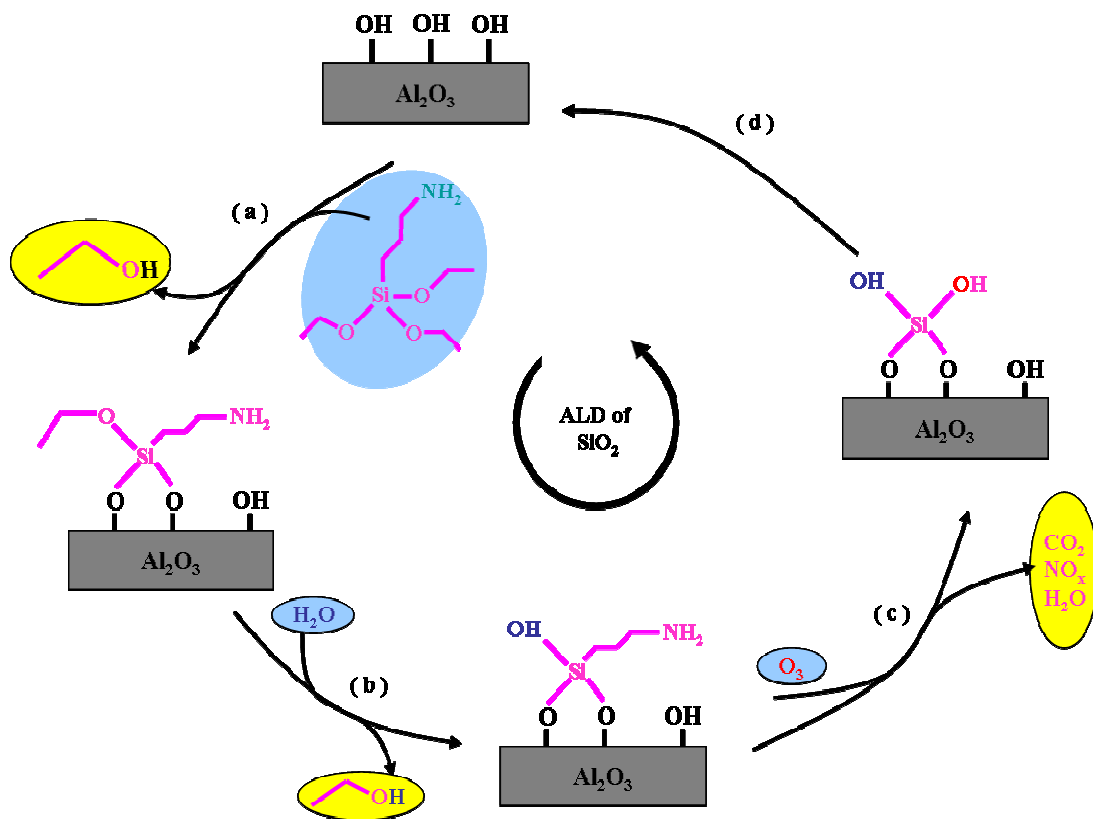


Figure 2.6. One cycle of ALD of SiO_2 from 3 precursors (a) Anchoring: surface hydrophilic groups cleave Si-OEt bonds of the first precursor under self-catalysis, leading to chemisorption with surface functional groups, b) Hydrolysis: ethoxy groups removed by self-catalysis, c) Oxidation: the aminoalkyl arm is removed by the third precursor, d) Completion of one cycle of ALD^[2,34]

Synthesis of Bi nanowires. Prior to the deposition of Bi nanowires, an Au electrode was prepared at the bottom of the AAO membrane using sputtering and constant current density (1 mA/cm^2) electrochemical deposition. In the next step, cyclic voltammetry (CV) was performed as a preliminary experiment to find an optimum potential for the electrochemical deposition of Bi nanowires. The operating potential was between -0.5 and 0.5 V and the scan rate was 20 mV/s. Bi nanowires were deposited by potentiostatic (constant potential) deposition at an applied voltage of -35 mV deduced from CV data. This electrodeposition was performed in the PAR model 263A Potentiostat/Galvanostat with a three electrode-configuration, in which a Pt wire was used as a counter electrode and Ag/ AgCl/ KCl (sat'd) as a reference electrode. Bi ions provided from 0.021 M $\text{Bi}(\text{NO}_3)_3 \cdot 5\text{H}_2\text{O}$ were dissolved in 1.2 M HNO_3 .

Characterization. X-ray diffractometry (XRD, Philips with Cu $K\alpha$ radiation, $\lambda=1.5406\text{\AA}$) was employed to assess the crystalline structure of the Bi nanowire arrays. Transmission electron microscopy (TEM), high resolution transmission electron microscopy (HRTEM) and selected area electron diffraction (SAED) were also used to determine the crystalline structure of nanowire arrays. The AAO matrix and the Au electrode layer were dissolved in 2M NaOH solution and an Au etching solution (KI_3), respectively. Subsequently, the nanowires were purified by DI water several times for TEM observation. A droplet of solution was placed on a carbon grid and allowed to dry at room temperature. Scanning electron microscopy (SEM, JSM 6340F) was used to observe the morphology of Bi nanowires. An energy dispersive x-ray spectrometer [EDX (JEOL, JEM-2100)] attached to the TEM was used to investigate the composition of the Bi nanowire surrounded with SiO_2 . Using the FT-IR (Fourier Transform Infrared Technique), the absorption was measured from free standing Bi nanowires holding together by a partially etched AAO matrix. The Bi nanowires were coated with SiO_2 nanotubes.

2. 6 Results and Discussion

Figure 2.7 shows the procedure of an initial pore diameter reduction before (Figure 2.7 A) and after (Figure 2.7 B) ALD of SiO_2 from as prepared AAO membranes with pore diameters of 50 nm (the pores are widened during the detachment process of the AAO membrane in 5 wt% phosphoric acid). After 120 cycles of ALD, the pore diameter is reduced down to 30 nm maintaining the interpore distance of as prepared AAO membranes (~ 110 nm). Figure 2.7 C shows uniform deposition of the SiO_2 layer through the whole channel structure up to an aspect ratio of 400 (50 nm diameter and 20 μm thickness). SiO_2 nanotubes released from their alumina matrix, with an outer diameter of 50 nm and a wall thickness of 10 nm are shown in Figure 2.7 D. Based on Figure 2.7 D, we can calculate the deposition rate of SiO_2 . After 120 cycles of ALD, the wall thickness of the SiO_2 nanotubes shows about 10 nm indicating that the rate is quite high: A deposition rate of 0.8 $\text{\AA}/\text{cycle}$ is calculated compared to the “ideal” ALD reaction with a deposition rate of 1 $\text{\AA}/\text{cycle}$.^[2,35]

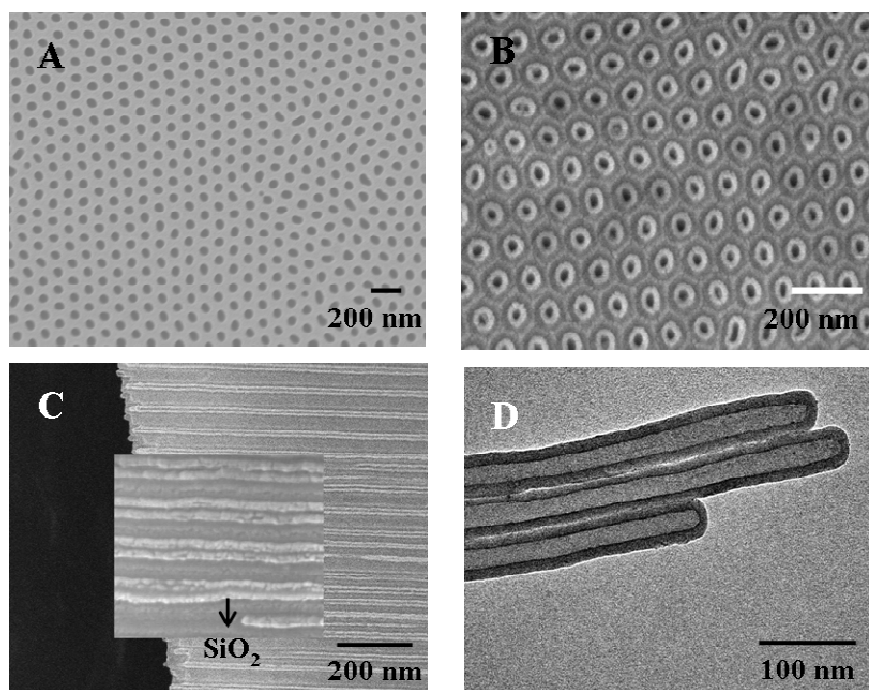


Figure 2.7. SiO₂ nanotubes prepared in AAO; (A) as-prepared AAO from 0.3M oxalic acid, (B) top surface view after 120 cycles of ALD of SiO₂, (C) a cross sectional image of (B) and (D) SiO₂ nanotubes released from AAO after etching in 5 wt% H₃PO₄

Figure 2.8 shows cyclic voltammetry (CV) of the Bi³⁺ included electrolyte between the operating potentials -0.5V and +0.5V. The aim of the CV is to determine an optimized potential at potentiostatic electrodeposition as well as to investigate the behavior of Bi³⁺ ions from the electrolyte in the operating potential. One reduction and one oxidation peak (labeled as peak A and B) were observed in the cathodic scan at -45 mV and 0.15 V. The optimized reduction potential was determined as -45 mV allowing the continuous growth of Bi nanowires for potentiostatic electrodeposition. The reduction phenomena can occur from Bi³⁺ to Bi(s) due to an application of its appropriate potential.

Figure 2.9 shows the typical morphology of Bi nanowires based on AAO membranes without an ALD of SiO₂ layers. Figure 2.9(A) displays a high filling of Bi nanowires with a diameter of 50 nm. Ion milling was carried out for the removal of the overgrown Bi film onto AAO prepared in 0.3 M oxalic acid. Figure 2.9(B) shows an array of Bi nanowires, holding together with the bottom Au electrode, with a diameter of 200 nm in partially etched AAO prepared from 1 wt% phosphoric acid. The AAO membrane is partially etched in 5 wt% phosphoric acid for 30 min. It is evident that our electrodeposition condition is suitable for depositing high aspect ratio Bi nanowires into the pores of AAO.

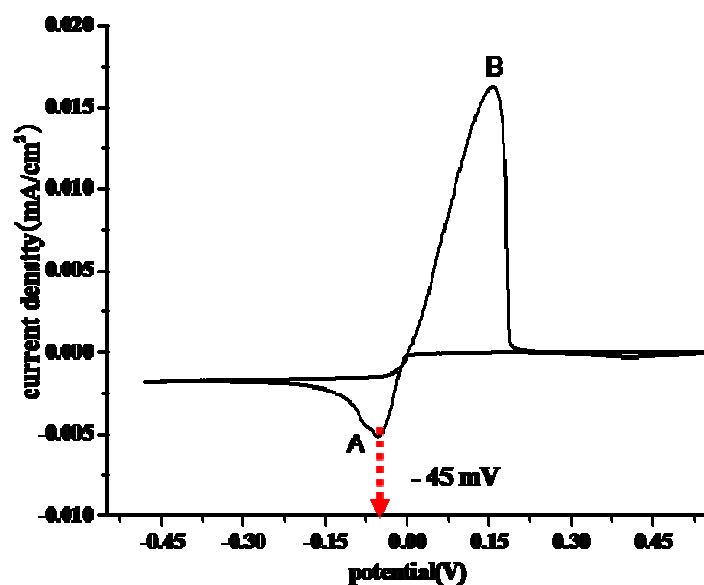


Figure 2.8. Cyclic Voltammetry (CV) of the Au working electrode deposited by electrochemical deposition on a silver plate in a mixture solution of 0.021 M $\text{Bi}(\text{NO}_3)_3 \cdot 5\text{H}_2\text{O}$ and 1.2 M HNO_3 in the operating voltage between -0.5 and +0.5 V. (scan rate: 20mV/s, surface area: 1.13cm^2 , counter electrode: Pt wire and reference electrode: Ag/ AgCl/ KCl(sat'd))

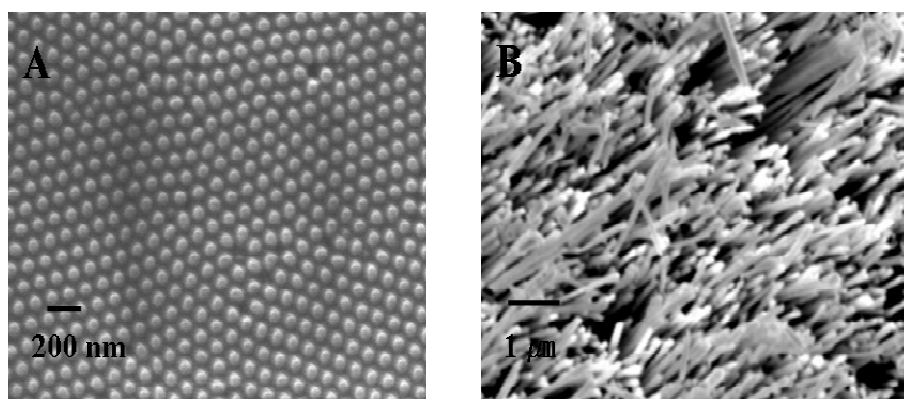


Figure 2.9. The morphology of Bi nanowire arrays; (A) top surface view of Bi nanowires grown in AAO membranes prepared from 0.3 M oxalic acid after ion milling and (B) Bi nanowire arrays grown in AAO membranes prepared from 1 wt% phosphoric acid after partially etching of the AAO matrix in 5 wt% H_3PO_4

A cross-sectional SEM image of Bi nanowires and a TEM image of a free standing single Bi nanowire surrounded by a SiO_2 shell are shown in figure 2.10. In addition the composition of the Bi- SiO_2 structure nanowires was analyzed by EDX (Figure 2.10 C).

The SiO₂ layer is coated uniformly along the entire Bi nanowire as shown in Figure 2.10 B. EDX (Figure 2.10 C) reveals that Bi, Si and O are detected in this structure.

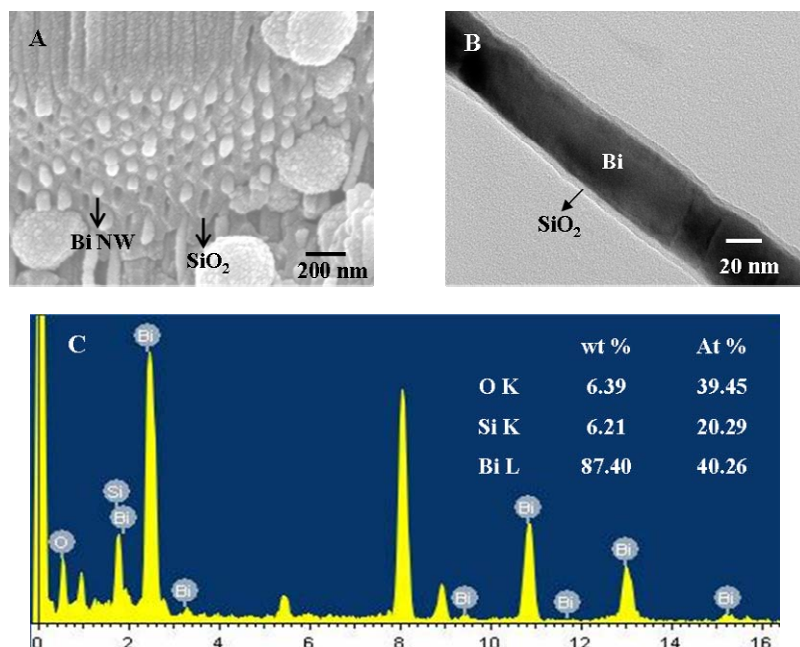


Figure 2.10. Electron microscopy (SEM and TEM) of Bi nanowires growth in SiO₂ coated AAO and EDX analysis; (A) a cross-sectional view of Bi nanowires in AAO with ALD of SiO₂, (B) single isolated Bi nanowire from AAO with ALD of SiO₂ and (C) elemental composition (Bi, Si and O) of Bi nanowires surrounded by SiO₂ layers, determined by EDX

Figure 2.11 shows the XRD patterns of Bi nanowire arrays with different wire diameters (30, 50 and 200 nm). The Au (111) orientation peak is still detected due to an imperfect removal of the Au electrode layer. An inset SEM image in Figure 2.11 confirms that the Au layer still remained after the selective removal of the Au electrode by wet chemical etching. In general, all of the peaks are located close to the peak of bulk Bi, revealing that the Bi nanowires with different diameters exhibited all a rhombohedral structure with $a=4.52 \text{ \AA}$, $c=11.17 \text{ \AA}$ and a space group of $R\bar{3}m$.^[2,36] Nevertheless several localized weak peaks exist in Bi nanowires of 200 nm diameter. Every Bi nanowire shows a similar crystalline structure. Independently the peaks detected at less than 26° originated from the AAO membrane. One orientation [110] peak dominates in all Bi nanowire arrays with different diameters. It is evident that the Bi nanowire arrays show a highly preferred orientation peak along the [110] axes perpendicular to the bottom of the AAO pores. Additionally, no peaks of SiO₂ were observed, indicating that the SiO₂

layer formed by ALD is amorphous. This will be confirmed in the next HRTEM figure.

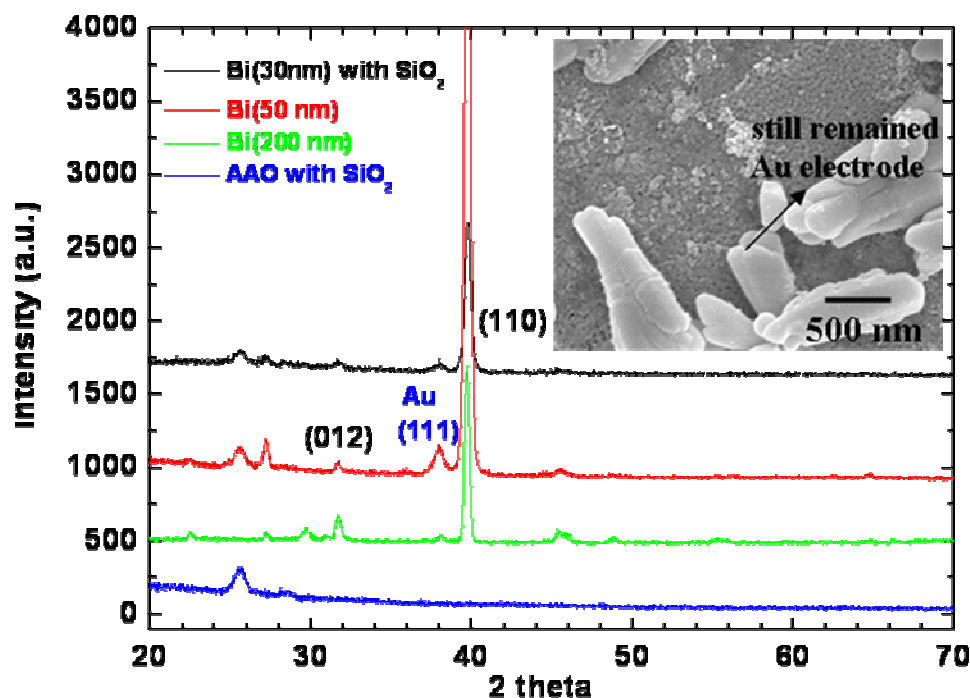


Figure 2.11. X-ray diffraction pattern of Bi nanowires with and without SiO₂ layer. For comparison, the XRD pattern of an unfilled AAO with SiO₂ coated pore walls is also shown. (The Au peak at (111) comes from the remnants of the gold bottom electrode (see inset).

As shown in figure 2.12, the crystalline structure is further investigated by TEM and corresponding SAED patterns. Figure 2.12(B) shows the corresponding SAED of figure 2.12(A), which shows arrays of Bi nanowires (30 nm diameter) coated by SiO₂ nanotubes (10 nm wall thickness). Figure 2.12(C) displays the SAED of Bi nanowire arrays with a diameter of 200nm. The observed intensities in the diffraction patterns show a correlation with wire diameters and are indicative of the polycrystalline nature of the wires. Based on these patterns, one can determine the growth planes (012) and (110). This observation will be confirmed by HRTEM in the next figure.

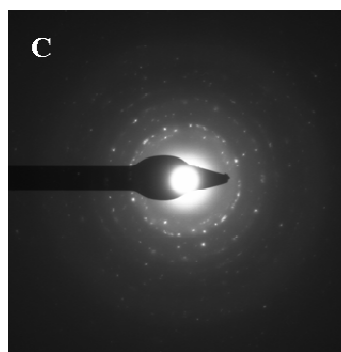
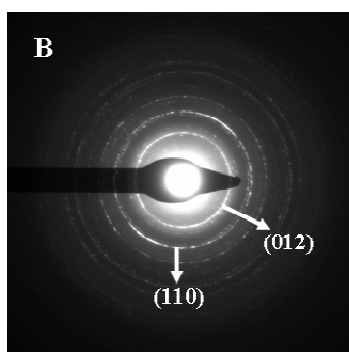


Figure 2.12. TEM image of Bi nanowire arrays (30 nm diameter) with SiO₂ coating (10 nm) (A) and corresponding selected area diffraction pattern (SAED) (B) as well as (C); SAED of Bi nanowire arrays with a diameter of 200 nm

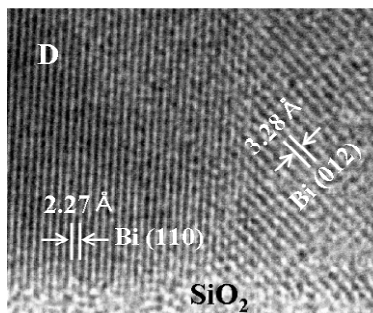
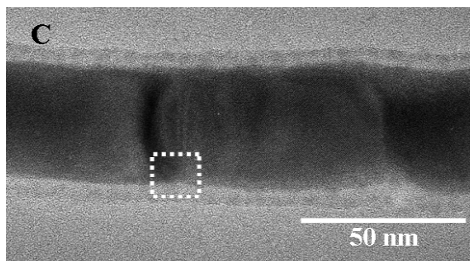
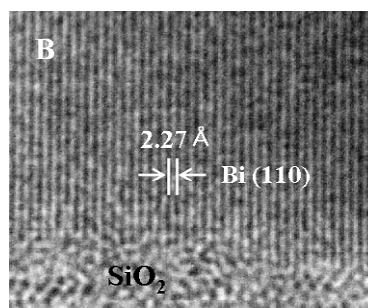
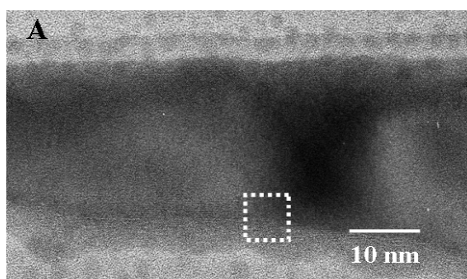


Figure 2.13. (A) and (C) TEM image of a single Bi nanowire surrounded by SiO₂, (B) and (D) high resolution TEM (HRTEM) images corresponding to (A) and (C), respectively

Figure 2.13 shows typical TEM micrographs and the corresponding magnified HRTEM pictures of Bi nanowires. The diameter of the Bi nanowire (30 nm) is equal to the pore size of the AAO template after ALD of SiO₂. Figure 2.13 (B) shows the HRTEM of the dotted rectangle area in the corresponding figure 2.13(a). The crystalline structure indicates the (110) oriented plane perpendicular to the nanowire growth direction. Another Bi nanowire shows that two oriented types of lateral planes (110) and (012) coexist in the selected rectangular area (Figure 2.13 (D)). As shown in Figure 2.13 (D), interplanar distances of 2.27 and 3.28 Å are visible, consistent with the interspacing of the (110) and (012) planes, respectively. Similar to Figure 2.13 (B), the (110) plane is perpendicular to nanowire axes whereas the (012) plane is tilted around 45° to the nanowire axes. These two HRTEM images are in good agreement with previous XRD data (figure 2.11), which showed a preferred oriented [110] direction and a weak intensity of the [012] direction in Bi nanowires with ALD of SiO₂.

2. 7 Conclusions of Chapter 2

Bi nanowires with different diameters were embedded in AAO and modified AAO membranes by ALD of SiO₂. SiO₂ nanotubes were very uniformly deposited with a high aspect ratio (more than 100) in AAO membranes. The thickness of the SiO₂ film was precisely controlled by the cycle number of ALD. Bi nanowires were well grown by potentiostatic electrochemical deposition at an optimized applied potential (-45 mV). All the Bi nanowires were of polycrystalline nature and [110] oriented grains as well as [012] grains coexisted in the 30 nm diameter wires. In addition, the coated SiO₂ nanotubes were amorphous.

Chapter 3

Annealing Bi₂Te₃ Nanowires for Improving the Crystalline Structure

In this chapter an approach is demonstrated for the enhancement of the electrical properties of Bi₂Te₃ nanowires. Bi₂Te₃ nanowires are annealed at different temperatures in order to improve their crystalline structure. It is expected that the annealing process affects the recrystallization of the Bi₂Te₃ nanowires along with a reduction of crystalline defects as well as an increase of the carrier concentration, leading to an improvement of the electrical conductivity.

3.1 Annealing of Bi₂Te₃ Nanowires

As discussed in chapter 1, Bi₂Te₃ nanowires grown by pulsed electrodeposition with 50 ms of relaxation time (μ 50) were chosen for the annealing process because of their good crystalline structure and homogeneous degree of pore filling.

For the annealing of the nanowires, a differential thermal analysis has been conducted in order to investigate the decomposition phenomena of the Bi₂Te₃ material embedded in the alumina matrix at the annealing temperature. Differential Scanning Calorimetry (DSC) is employed to detect thermal transitions in the material. When Bi₂Te₃ material decomposes as the temperature is increased, DSC analysis can also identify the temperature at which this process begins and the various stages in the thermal decomposition. The technique depends on a measurement of the heat evolved or

absorbed when a material undergoes a phase transition or a chemical reaction.

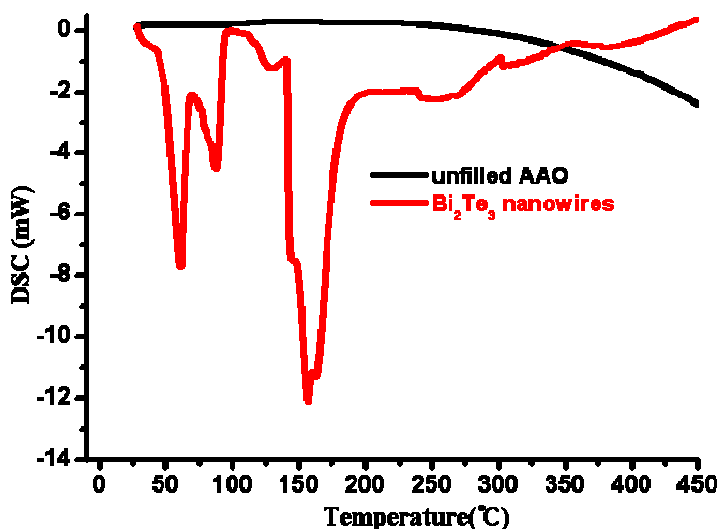


Figure 3.1 DSC curves of Bi₂Te₃ nanowires grown by pulsed electrodeposition in a pure AAO membrane prepared from 0.3 M oxalic acid

Figure 3.1 shows the temperature dependence of the differential heat flows of the as-prepared Bi₂Te₃ nanowires in a AAO membrane and an unfilled AAO membrane in the temperature range of 30 to 450 °C with heating rate of 5 °C/min. One can see that the first phase transition associated with an exothermic peak takes place at around 55 °C and a second one around 155 °C. The second peak's position is similar to that given in a previous report (ca. 130 °C) ^[3.1] On the other hand, the unfilled AAO membrane is much more stable in this temperature range. It starts to recrystallize around 300 °C. Hence, Bi₂Te₃ nanowires are annealed at 150, 250 and 400 °C. The annealing of the nanowires is performed in an Ar atmosphere with 2 mbar pressure for 4 hrs. Before starting a temperature increase, the pre-flow time is sustained for 30 min in order to eliminate all contaminations in the tubular chamber.

3. 2 Energy-Dispersive X-ray Spectroscopy (EDX)

After the bismuth telluride nanowires are annealed at different temperatures, elemental analysis is performed with EDX by a line scan of individual nanowires as well as overgrown bismuth telluride films on AAO membranes.

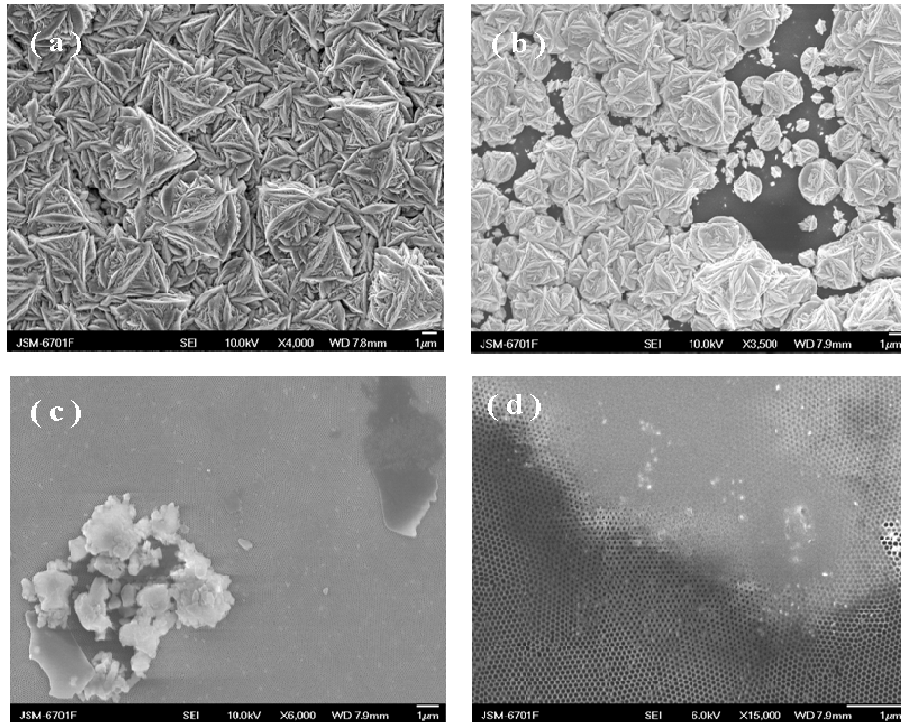


Figure 3.2. The morphology changes of overgrown bismuth telluride film with increasing annealing temperature (before annealing (a), 150°C (b), 250°C (c) and 400°C (d))

	pu 50	150°C	250°C	400°C
Bi (at %)	41.28	39.44	44.51	50.11
Te (at %)	58.72	60.56	55.49	49.89
Atomic ratio (Te / Bi)	1.422	1.535	1.246	0.995

Table 3.1. Bi and Te atomic percentage of overgrown bismuth telluride film annealed at different temperatures

The morphology of the overgrown bismuth telluride film is changing with increasing annealing temperature as shown in figure 3.2. The overgrown bismuth telluride film is peeled off in the samples annealed above 250°C. This might be due to the high vapor pressure of the Te compound during annealing in the Ar atmosphere. The vapor pressure of tellurium is given in table 3.2. As shown in table 3.2, the vapor pressure of Te is much higher than that of Bi. Therefore, there is a high possibility that Te compounds vaporize during the annealing process at high temperatures. The data of table 3.1 show that the Te concentration decreases with increasing annealing temperature.

temperature (°C)	130	330	450
pressure (m bar)	5.9×10^{-11}	9.6×10^{-4}	1.8×10^{-1}

Table 3.2. Vapor pressure of tellurium (Te) as a function of temperature ($P_{\text{Bi}} = 6.27 \times 10^{-6}$ mbar at 280°C)^[3,2]

Next, the individual bismuth telluride nanowires are investigated by an elemental analysis with a line scan EDX attached at the TEM system.

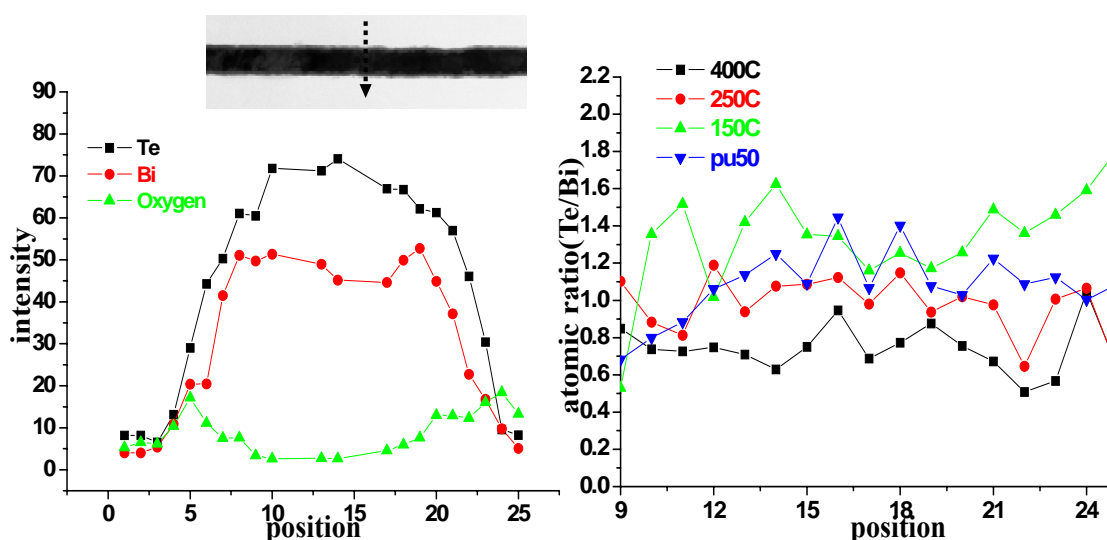


Figure 3.3. EDX of an individual bismuth telluride nanowire annealed at different temperatures [(a); intensity and (b); atomic ratio (Te / Bi)]

As the annealing temperature increases, the Te component decreases similarly as for previous EDX data of the overgrown film. The composition of the pu 50 and the 150°C sample shows similarly Bi_2Te_3 and the transformation into Bi_4Te_5 (250°C) and Bi_4Te_3 (400°C) with increasing annealing temperature. The phase change will be confirmed by the following XRD and TEM data. In addition, the formation of a bismuth oxide layer on the outer surface of nanowires is confirmed by figure 3.3 (a). The positions 4 and 24 at the x-axis show a fluctuation of the oxygen intensity and a plateau of the bismuth intensity by the line scan inside the nanowire. It indicates that a bismuth oxide (Bi_2O_3) layer only forms in the outer surface of the nanowire as a shell structure during the annealing process. In a previous report by E. J. Menke et al.,^[3,3] it was found from XPS (X-ray photoelectron spectroscopy) data for freshly prepared nanowires that the oxide structures are quickly covered with a mixed bismuth and tellurium oxide layer resulting from the air oxidation at the surface of the Bi_2Te_3 nanowires. On the basis of the layered

oxide structure model suggested by Bando et al.^[3.4], the inelastic mean free paths of the photoelectrons^[3.5] it is estimated that within an hour of air exposure the oxide structure consists of layers of Bi_2O_3 and TeO_2 that are 2.2 and 1.1nm thick, respectively.

In particular, several black spots (crystallites) are observed in the bismuth telluride nanowire annealed at 250°C. Therefore, line scans have been performed especially focused on this area, as shown in figure 3.4. As shown in figure 3.4 (a), the intensity of bismuth is decreased significantly at a certain point as well as the intensity of Te is increased simultaneously. It is a decisive proof that the composition of crystallites shows relatively pure Te (tellurium). In addition, the atomic ratio is also higher (6) than in other areas of this nanowire (ca. 1.0) and the stoichiometrical value is increased (1.5), both indicating a Te rich chemical state through this crystallite area.

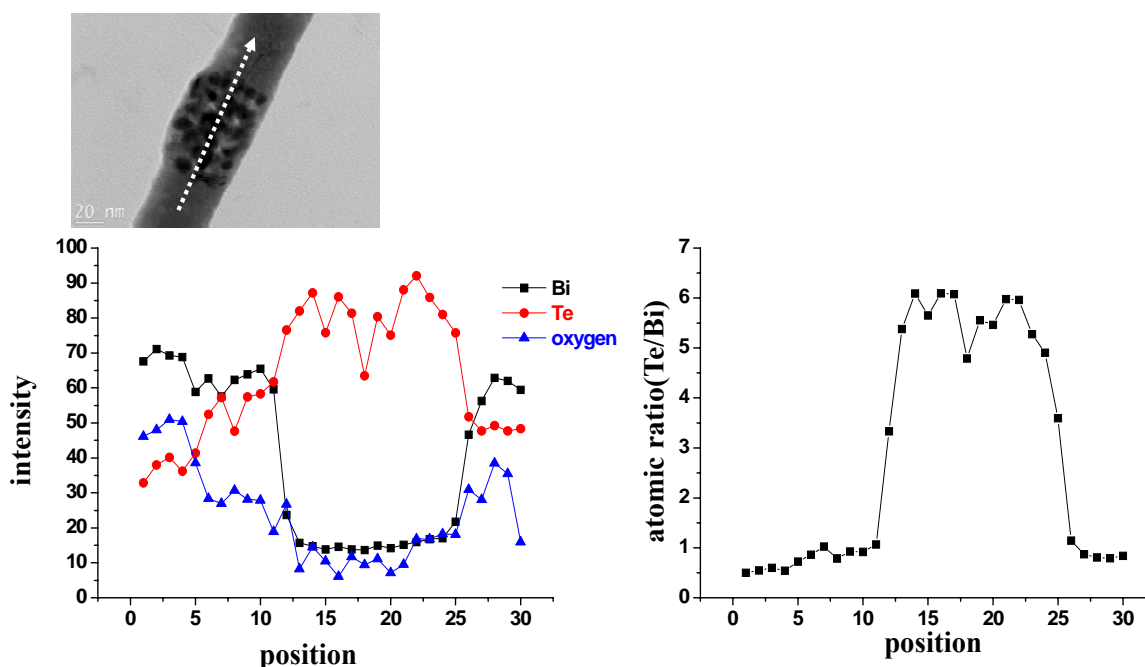


Figure 3.4. EDX of an individual bismuth telluride nanowire annealed at 250°C (line scan performed inside the nanowire)

3.3 Crystalline Structure of Bi_2Te_3 Nanowires

Figure 3.3 shows the XRD patterns of Bi_2Te_3 nanowire arrays annealed at different temperatures. Pu 50 and bismuth telluride nanowire arrays annealed at 150°C show a similar crystalline structure (rhombohedral ($R\bar{3}m$) space group, $a=4.385 \text{ \AA}$ and $c = 30.48 \text{ \AA}$, ref. JCPDS No.150863). The highly preferred direction $[110]$ is shown with

different intensity. However, as the temperature increases (250 and 400°C), Au ([111] and [220]) and new bismuth telluride phase (Bi_4Te_5 and Bi_4Te_3) peaks appear due to a recrystallization of the nanowires and loss of tellurium (Te) during the annealing process, remaining the rhombohedral ($P\bar{3}m1$ and $R\bar{3}m$) space group ($a = 4.41 \text{ \AA}$, $c = 54.33 \text{ \AA}$ and $a = 4.451 \text{ \AA}$, $c = 41.88 \text{ \AA}$, ref. JCPDS No.220115 and 330216), respectively. Furthermore, Bi_4Te_3 [110] peak shifts negatively ca. 0.3° (40.88°) in comparison with other phase's [110] peak, in agreement with reference JCPDS No.330216.

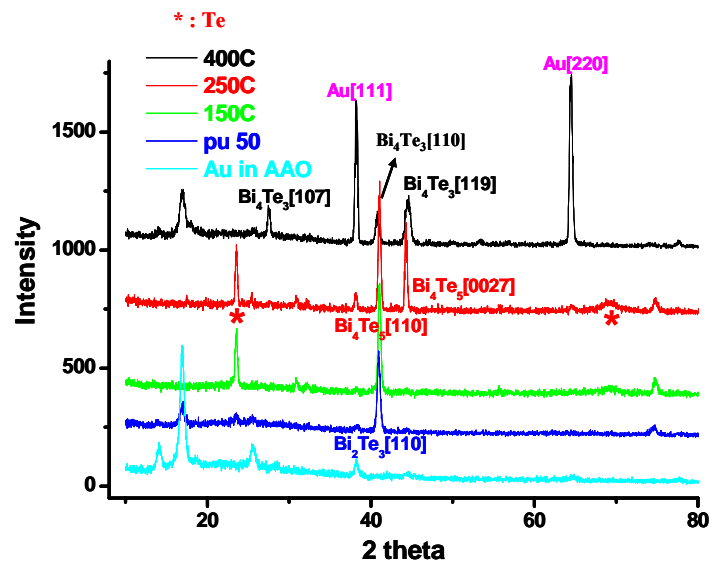


Figure 3.5. XRD patterns of the Bi_2Te_3 nanowire arrays annealed at different temperature

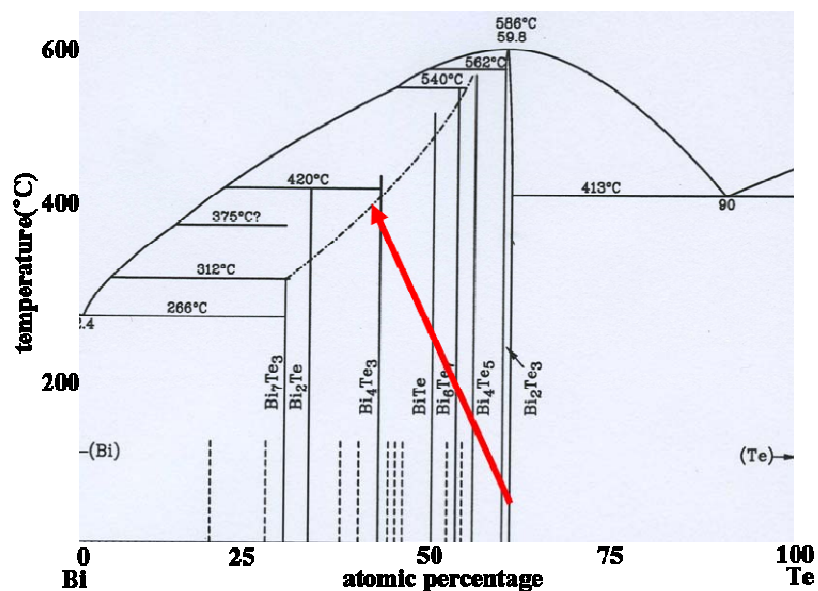


Figure 3.6. Phase diagram of binary alloy Bismuth-Tellurium as a function of temperature^[3,2]

Bismuth telluride nanowires as fabricated are in the Bi_2Te_3 phase and transform during the annealing steps into Bi_4Te_5 and Bi_4Te_3 with increasing annealing temperature as shown in figure 3.6. This fact (bismuth telluride phase changes with increasing annealing temperature) is in agreement with previous EDX data as well as with selected area electron diffraction patterns.

SAED pattern of different bismuth telluride nanowire(s) are shown in figure 3.7.

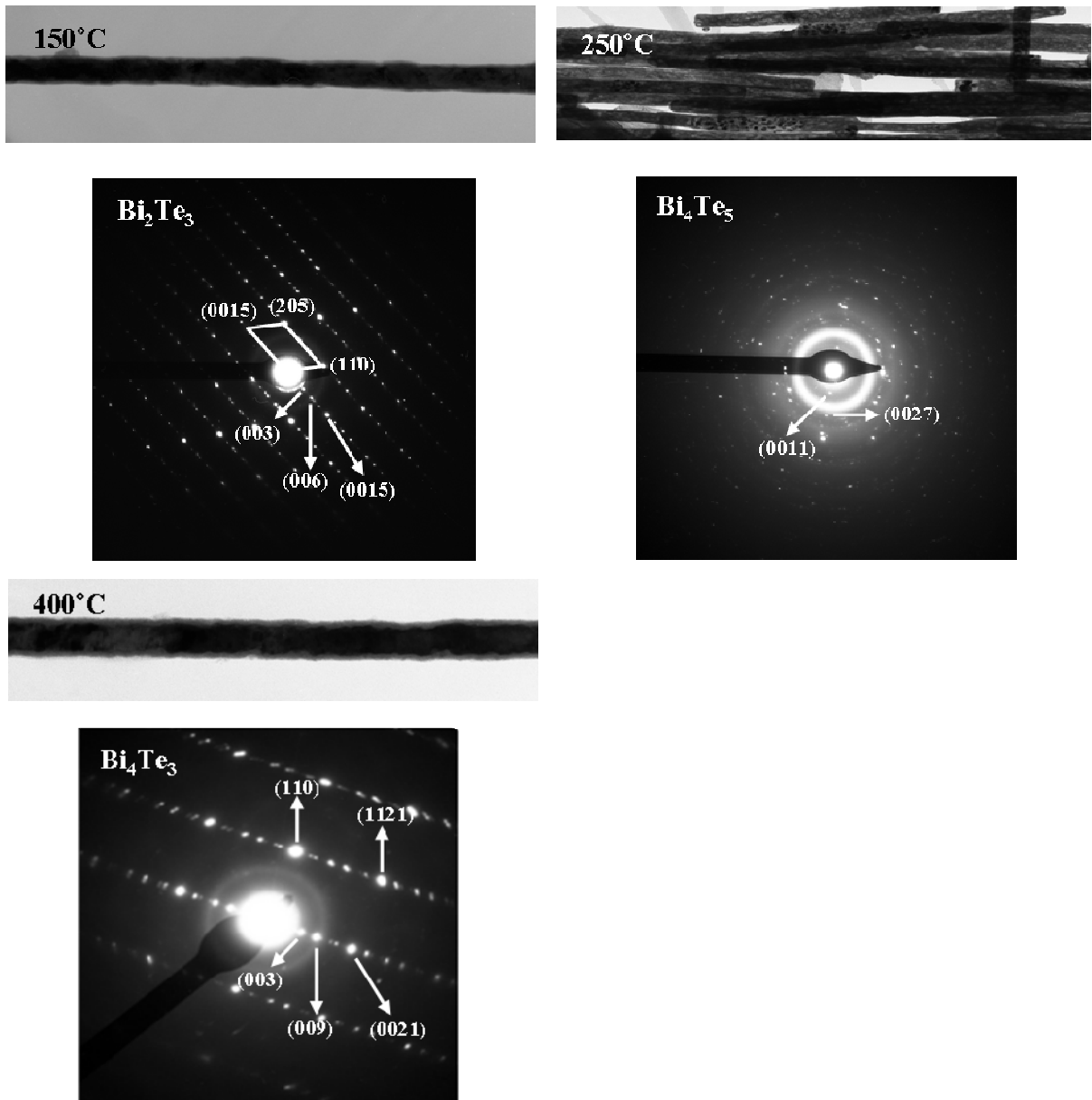


Figure 3.7. TEM and corresponding selected area diffraction pattern (SAED) of bismuth telluride nanowire(s) annealed at different temperatures

In the case of bismuth telluride nanowires annealed at 150°C, the SAED pattern consisting of bright spots indicates the single crystalline structure of the nanowire, which can be indexed to (205), (110) and (0015) as the hexagonal Bi_2Te_3 phase (rhombohedral ($\bar{R}\bar{3}m$) spacing group). In addition, this nanowire is crystallized with the c-axis (00 l) growth perpendicular to the nanowire. However, in the case of 250°C annealing, the SAED pattern shows a polycrystalline structure. The main reason might be the mixture of a Bi_4Te_5 phase (rhombohedral ($\bar{P}\bar{3}m1$) spacing group) and Te phase crystallites. The indexes of (0011) and (0027) are observed in the corresponding SAED pattern, indicating similar c-axis growth like bismuth telluride nanowires annealed at 150°C. At last, the SAED pattern of bismuth telluride nanowires annealed at 400°C shows the single crystalline structure again. This phenomenon might be caused by recrystallization of Te crystallites and subsequent transformation to a more stable bismuth telluride phase (Bi_4Te_3). The SAED pattern consisting of bright spots also indicates the single crystalline structure, which can be indexed to (110), (1121) and (0021) as a Bi_4Te_3 phase (rhombohedral ($\bar{R}\bar{3}m$) spacing group).

3. 4 Conclusions of Chapter 3

Bi_2Te_3 nanowires grown by pulsed electrochemical deposition are annealed at different temperatures (150, 250 and 400°C) according to thermal analysis (DSC). The Te concentration is decreasing with increasing annealing temperature and Te crystallites are observed inside nanowires annealed at 250°C. Consequently, the phase change of nanowires takes place with increasing annealing temperature ($\text{Bi}_2\text{Te}_3 \rightarrow \text{Bi}_4\text{Te}_5 \rightarrow \text{Bi}_4\text{Te}_3$). The electron diffraction pattern of the nanowires indicates the single crystalline structure despite of a phase change, except that a polycrystalline structure is found in the nanowires annealed at 250°C due to a coexistence of Te crystallites and the Bi_4Te_5 phase. Consequently, bismuth telluride nanowire arrays need to be annealed at Te ambient atmosphere with a sufficiently high overpressure (which should be optimized) of Te in order to prevent the evaporation of tellurium compounds.

Chapter 4

Optical Characterization of Bi Nanowires

In this chapter the optical absorption of bismuth nanowire arrays is investigated. This optical property of bismuth nanowire arrays in partially etched AAO is studied by means of Fourier Transform-Infrared Spectroscopy (FT-IR). According to the band edge shift depending on the diameter of bismuth nanowires in the FT-IR data, the transition from a semi-metallic to a semiconducting phase, as mentioned in chapter 2, is experimentally demonstrated, indicating a good agreement with theoretical models.^[4.1-4]

4. 1 The Preparation for Optical Characterization

After fabrication of Bi nanowires with different diameters in AAO membranes and the AAO membranes with SiO₂ nanotubes, the template is partially removed by mechanical and wet etching methods. The preparation procedure is illustrated in figure 4.1. Due to the inhomogeneous growth of Bi nanowires from potentiostatic electrochemical deposition, an overgrown Bi film forms on the top surface of the AAO matrix and some part of the AAO remains unfilled. Therefore, ion milling and mechanical polishing by alumina polishing suspension (Pro.656, Gatan) have been performed for the removal of the overgrown film. Additionally, the bottom of the Au electrode is also eliminated by an Au etching solution (KI₃). Finally, the AAO membrane is partially etched away in 5 wt% phosphoric acid.

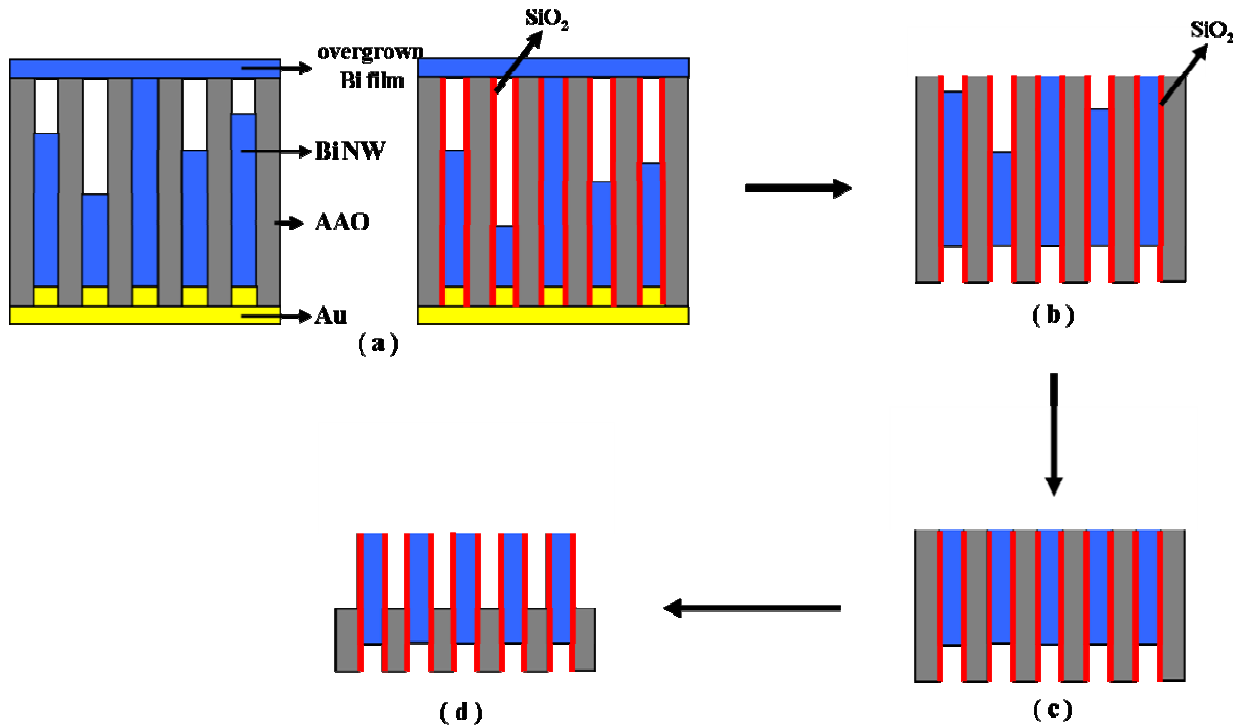


Figure 4.1. Schematic diagram of the preparation procedure for the optical characterization of bismuth nanowire arrays with different diameter

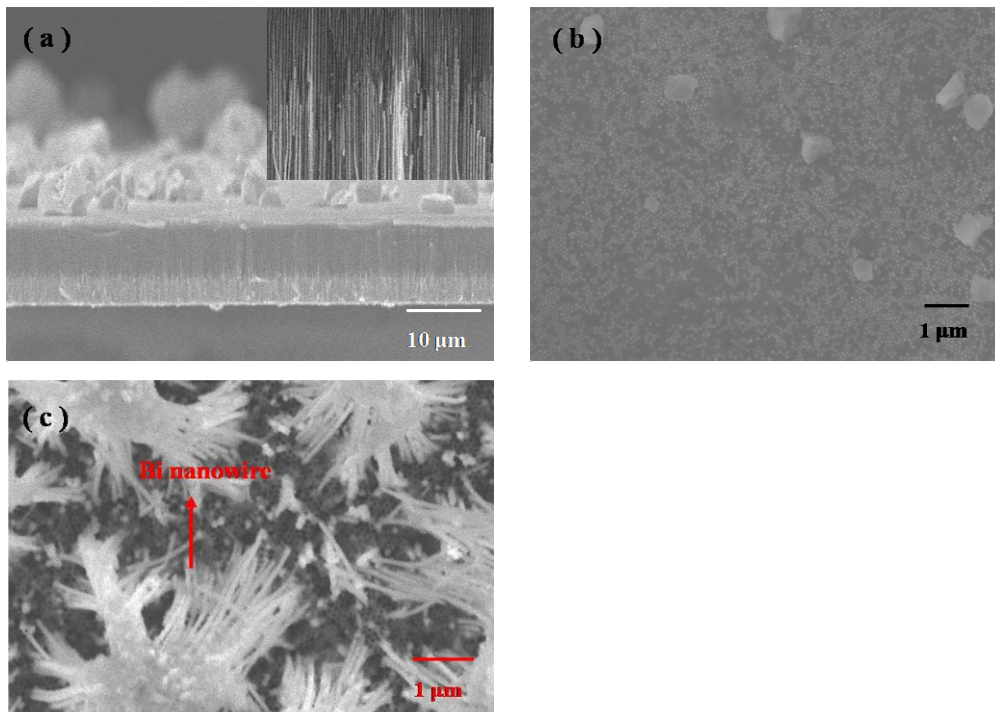


Figure 4.2. SEM image of (a) a cross-sectional view of Bi nanowires in AAO and the inset image shows the enlargement of Bi nanowires filled, (b) top surface view after ion milling and (c) free standing Bi nanowire arrays in partially etched AAO

To gain information on the band structure of the synthesized samples, we performed Fourier-transformed infrared (FT-IR) absorption measurements on wires embedded in alumina templates. The measurements were performed in ambient air at room temperature. As the wavelength of incident light is much larger than both the wire diameter and the thickness of the alumina template, both media will in principle contribute to the absorption. In principle, one has to deconvolute their contributions by use of sophisticated models such as, e.g., the Effective Medium Theory.^[4,4] However, since the energy bandgap of alumina (~ 5.94 eV) is much larger than that of semiconducting bismuth nanowires (~ 100 meV), it is reasonable to assume that the measured absorption is mainly due to the Bi nanowires.

Two arrays of nominally 30-nm-thick nanowires showed clear absorption edges, E_A , at 87 meV (blue line) and at 83 meV (green line). The corresponding value for an array of 50-nm wires (red line) cannot be evaluated unambiguously from the absorption data, yet E_A here has an apparently smaller value than those for thinner wires. The precise value of the energy gap, however, can be estimated through electrical measurements, as will be discussed below. On the other hand, the obvious lack of any absorption edge for 200-nm-thick nanowires (black line) points at the metallic character of these samples. The observed red-shift of E_A for semiconductor wires and the eventual transition to the semimetallic regime as the wire diameter increases are in accordance with the predictions of theoretical models.^[4,1-4] To shed more light on the details of the measured optical data, below we discuss the origin of the additional absorption peaks detected at higher energies.

The clearly visible absorption peaks in the sub-50-nm wires cannot be attributed to the inter-sub-band transitions, neither are they indicative of excitonic states. In both cases, contrary to what was observed, in the first place, one would anticipate a variation of the peak positions and their spacing with the wire diameter. Furthermore, these peaks have linewidths of about 5-10 meV. This has to be compared to the thermal broadening at around room temperature, $k_B T \sim 25$ meV. Accordingly, the clear separation of the first peaks, less than 20 meV apart, excludes attribution of the measured behavior to the inter-sub-band transitions. On the other hand, at higher energies, just below the conduction band edge at the gap region, the interspacing of suspected excitonic states should become much tighter. This is, again, in contrast to the experimental observations. Attribution of the observed peaks to excitonic states would also lead to an estimation of unrealistically large value for the energy gap. Based on the above arguments, we conclude that the observed peaks are not intrinsic to the bismuth nanowires and arise mainly from the presence of ambient molecules in the environment of the wires. While

the enhancement of absorption at around 290 meV most likely originates from CO₂ molecules in the surrounding air, the other peaks are probably due to the presence of various forms of water in the embedding alumina and in the air.^[4.5] Vibrational energies of nitrogen molecules do not match to the observed absorption range. Also, the native oxide layer formed around the tip of the wires, Bi₂O₃, has a much higher energy gap and its contribution to the absorption can be neglected here.

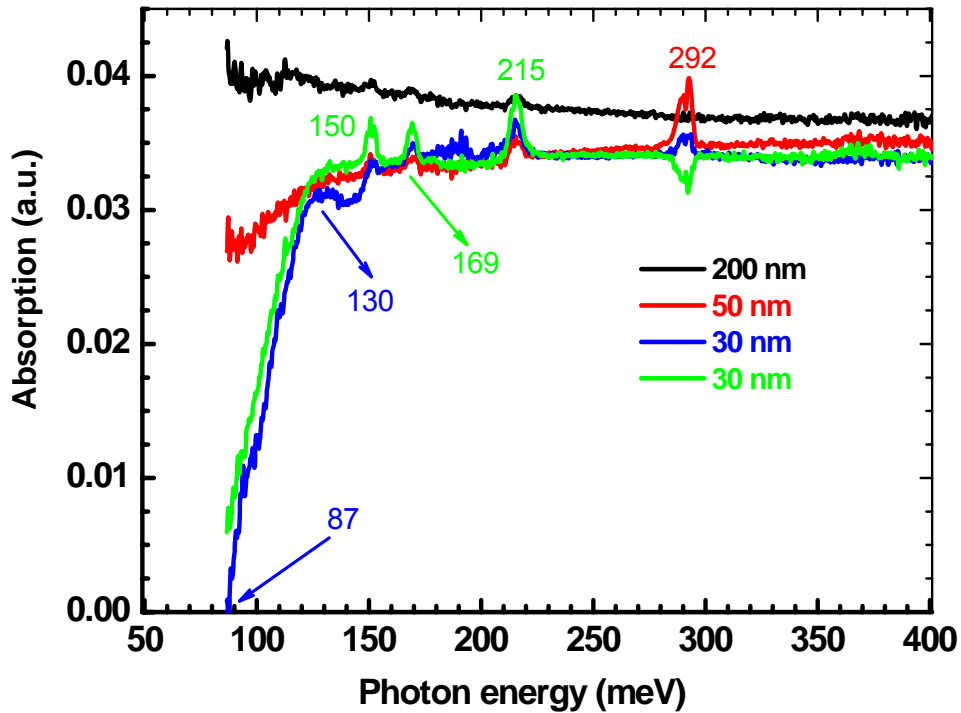


Figure 4.3. Measured Fourier-transformed infrared optical absorption of Bi nanowire with various diameters. The clearly visible absorption edge for two 30-nm nanowire samples, at 87 meV (blue solid line) and 83 meV (by extrapolation of the green solid line) are indicative of semiconducting behavior and suggest an energy gap of about 85 meV for the 30-nm thick wires. The thickest wire, 200 nm in diameter, shows no sign of an absorption edge, in accordance with a metallic behavior. The array with 50 nm nanowires is still semiconducting, but due to the experimental limitations, its absorption edge cannot be estimated unambiguously.

4. 2 Conclusions of Chapter 4

Free standing Bi wires holding together by the partially etched AAO were prepared for optical characterization. The dependence of the band edge absorption energy on the wire

diameter was investigated by FT-IR spectroscopy. In particular, no energy variations of the absorption peak around 100 meV were observed in dependence on the diameter of the nanowires, which would be an indication of quantum confinement effect as reported by the Dresselhaus group.^[4,6] Nevertheless, the band edges of nanowires with diameters equal to 30 and 50 nm were observed, proving the semiconducting characteristic, in contrast to those with 200-nm thickness (no existence of band edge) which showed a semimetallic behavior. Furthermore, these conclusions will be cross checked by electrical measurements which will be discussed in chapter 5.

Chapter 5

Electrical Characterization of Bi_2Te_3 and Bi Nanowires

In this chapter we demonstrate the measurement of the absolute resistivity (electrical conductivity) as well as the normalized electrical resistance behavior as a function of temperature in bulk Bi_2Te_3 , Bi nanowires and individual nanowires. First, the sample preparation method is discussed and then experimental results for 2-point and 4-point measurements are presented.

5. 1 Electrical Conductivity

In semiconductors, the electrical conductivity (δ) is limited by the density of majority carriers (electrons or holes) in the conduction band or valence band. At 0 K, electrons fill up the valence band, and the conduction band is empty. When the temperature increases, some electrons in undoped semiconductors are thermally excited from the valence band to the conduction band, increasing electrical conductivity. The concentrations of electrons n and holes p in intrinsic (undoped) semiconductors are proportional to $\exp(-E_g/2k_B T)$, where E_g is the bandgap and k_B the Boltzmann constant. Therefore, the electrical conductivity of semiconductors increases with an inverse exponential relationship to temperature.^[5.1]

5. 2 2-Point Measurement for Bi_2Te_3 Nanowire Arrays

The simplest way to measure the electrical conductivity that can be done on nanowires is to measure the whole nanowire array by attaching contacts to both sides of a filled AAO membrane using a thin copper wire and silver paste. This 2-point measurement of nanowire arrays has the advantage of an easy handling without special equipment. However, only the resistance behavior [$R(T) / R(300\text{ K})$] can be measured due to the unknown number of nanowires contributing to the conduction. The overall preparation for the measurement of the electrical resistance for Bi_2Te_3 nanowire arrays is described in figure 5.1. As mentioned in chapter 1, after the electrodeposition of Bi_2Te_3 nanowires, even in pulsed electrodeposition type, overgrown Bi_2Te_3 films usually formed on the top surface of the AAO membrane. In order to measure an electrical resistance from Bi_2Te_3 nanowire arrays with uniform length, the overgrown film as well as empty pores of AAO membranes, shown in figure 5.1(a), are required to be removed.

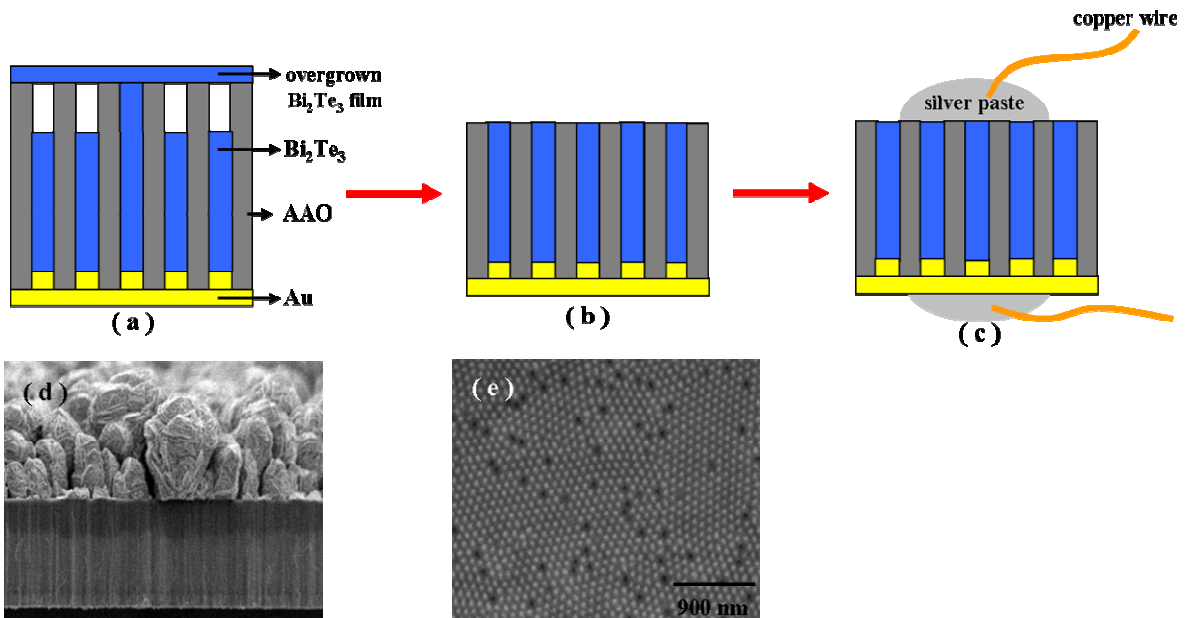


Figure 5.1. Schematic diagram of the preparation of samples for the measurement of the electrical resistance of Bi_2Te_3 nanowire arrays as a function of temperature [(d): SEM photograph of Bi_2Te_3 nanowires after fabrication by pulsed electrodeposition in AAO and (e): after removal of the overgrown Bi_2Te_3 film by ion-milling and mechanical polishing performed on the top surface of the AAO membrane, respectively]

The overgrown Bi_2Te_3 film was selectively eliminated by an ion milling process for 30 min for the removal of material on the scale of a few micrometers. Mechanical polishing was successively performed for the preparation of a uniform nanowire length. Alumina polishing suspension (Pro.656, Gatan) was used for mechanical polishing. A

scanning electron micrograph of the top surface view showed Bi_2Te_3 nanowires with a high filling ratio, ready for the measurement of the electrical resistance of nanowire arrays. Silver paste was placed onto the etched AAO membrane for the connection of the Bi_2Te_3 nanowires with a copper wire connected to a power supply.

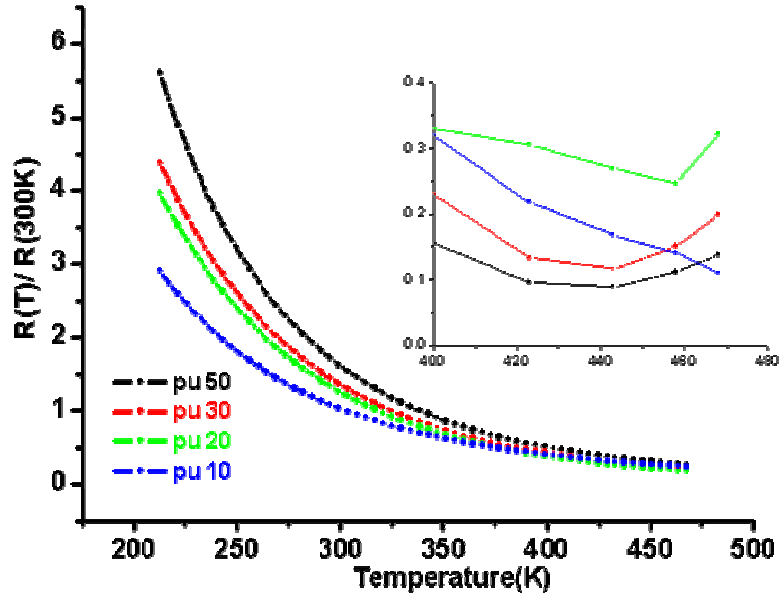


Figure 5.2. Dependence of the electrical resistance, R , on temperature, T , for different samples. The solid lines are theoretical fits to the measured data (see text). The enlarged view shows the R - T characteristics at higher temperatures. (“pu” in figure indicates Bi_2Te_3 nanowires grown by pulsed electrodeposition and the index numbers (10, 20, 30 and 50) give the relaxation (off) time in ms)

The small current ($1\mu\text{A}$) passed through the Bi_2Te_3 nanowires from the power supply and the corresponding potential were recorded. Therefore, the electrical resistance could be calculated via Ohm’s law. The normalized electrical resistance as a function of temperature is shown in figure 5.2. As the temperature falls, the sample resistances increase. This is a typical semiconducting behavior. As shown in chapter 1, Bi_2Te_3 nanowires fabricated in pulsed electrodeposition showed a single crystalline structure. However, for a poly crystalline structure, theoretical calculation indicates the resistance increase with temperature in the framework of the relaxation time approximation, with a metal-like characteristics.^[5.2] For the single-crystalline structure, the scattering process of the carriers is expected to be different from a polycrystalline structure, and both the carrier mobility and concentration affect the behavior of the temperature-dependence. Here, the increased carrier concentration and decreased mobility with increasing temperature play an important role in determining the temperature dependence of the

electrical resistance behavior.

The resistance enhancement at lower temperatures can be due to two distinct mechanisms, *i.e.*, a deactivation of the charge carriers of impurity levels, and/or the reduction of the intrinsic charge carriers in the specimen. To investigate these possibilities in more detail, assuming a $R=R_0\exp(E_a/2k_B T)$ dependence for the resistance, we have made numerical fits to the measured data. Here, R_0 is the asymptotic value of electrical resistance at $1/T \rightarrow 0$, E_a is the impurity activation energy or the energy gap of the semiconductor, and k_B is the Boltzmann constant. The obtained values for E_a are 287 meV, 276 meV, 243 meV, and 215 meV for the pu 50, pu 30, pu 20, and pu 10 samples, respectively. Comparing these values to the energy gap of bulk semiconducting Bi_2Te_3 at room temperature, 145 meV,^[5,3] and to the corresponding thermal energies, $k_B T \sim 25$ meV, we conclude that E_a should correspond to a semiconducting energy gap. The inset in figure 5.2 displays an enlarged view of the resistance-temperature characteristics at higher temperatures. From $T \approx 440$ K upward, except for the pu 10 sample, the resistances increase. We believe that this is a sign for the enhanced carrier-phonon scattering at higher temperatures.

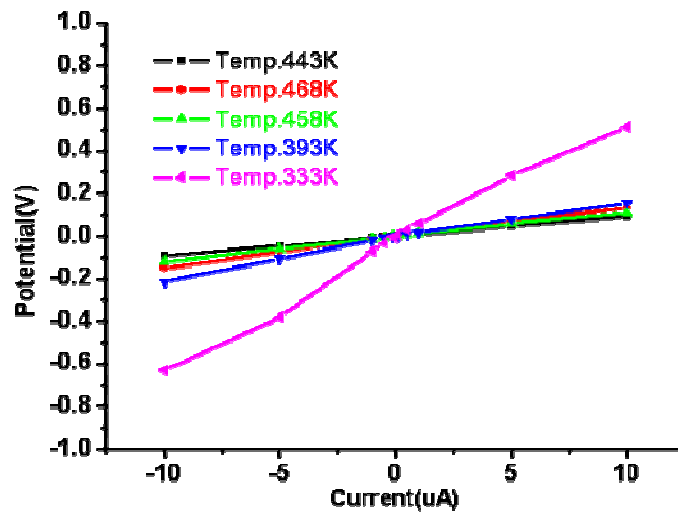


Figure 5.3. The current (I)-voltage (V) characteristic of a pu 30 sample for different temperatures. Please note the good linearity.

To exclude the possible existence of artificial effects, we have also measured the current-voltage (IV) characteristics of the samples at different temperatures. Fig. 5.3 shows results of such a measurement. The IV -curves are linear up to the highest temperatures and down to the smallest bias currents. These observations confirm the formation of good ohmic contacts to the embedded nanowires.

Due to the large uncertainties in the number of electrically contacted nanowires in the

membrane, N , a determination of the electrical resistivity ρ of a single nanowire is not reliable. For an array of about 15 μm long, 40 nm thick wires grown in an alumina template with a 110-nm pore periodicity, one arrives at a ratio $\rho / N \sim 10^{-5} \Omega\text{m}$. As the total number of nanowires over a 1 mm^2 area is about 3×10^8 , and assuming that the electrical resistivity of nanowires is not very much different from the bulk value, $\rho \sim 10^{-5} \Omega\text{m}$,^[5.4] the fraction of electrically contacted wires can be estimated to be as low as 1:10⁸. Unambiguous values for the resistivity, as well as for certain other transport properties, can only be reliably obtained by performing local measurements on individual nanowire.

5.3 2-Point Measurements for Bi Nanowire Arrays

The way to measure an electrical resistance behavior of Bi nanowire arrays is similar to Bi_2Te_3 nanowires. As discussed in chapter 2, the diameter of Bi nanowires depends on the cycle number of ALD of SiO_2 . In this part, the electrical resistance behavior of Bi nanowire arrays with different diameter is discussed. The preparation method is described in figure 5.4.

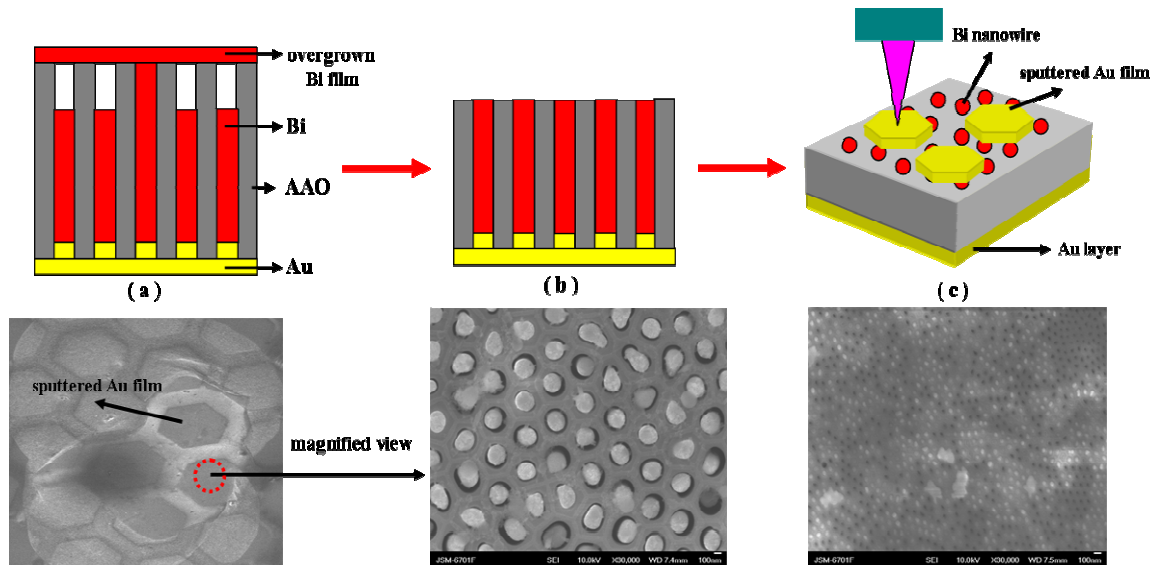


Figure 5.4. Schematic diagram of the preparation of Bi nanowire arrays for the measurement of the electrical resistance as a function of temperature. It is similar to the preparation of Bi_2Te_3 nanowires except for the last step. After ion milling and mechanical polishing (b) for the removal of the overgrown Bi film and empty AAO membrane (a), an Au layer is sputtered via a hexagonally shaped mask on the Bi nanowire arrays with different diameter in the AAO membrane (c). A needle with a few micrometer tip diameter contacts the sputtered Au layer.

Bi nanowire arrays with different diameters (magnified view shown in figure 5.4 SEM image, left (200 nm), right (30 nm+ SiO₂ 20 nm) and 50 nm diameter (not shown in here) were prepared for the measurement of the electrical resistance as a function of temperature. Concerning the filling factor, there is a difference between 200 nm and 30 nm shown in the figure 5.4 SEM image. It could be explained by observation that the nanowire growth of 200 nm wires is more homogeneous than that of 30 nm wires. Therefore, the filling factor of Bi nanowire arrays with 200 nm diameter is higher than those of 50 and 30 nm one. The electrical resistance behavior of Bi nanowire arrays with diameter of 200 nm is shown in figure 5.5.

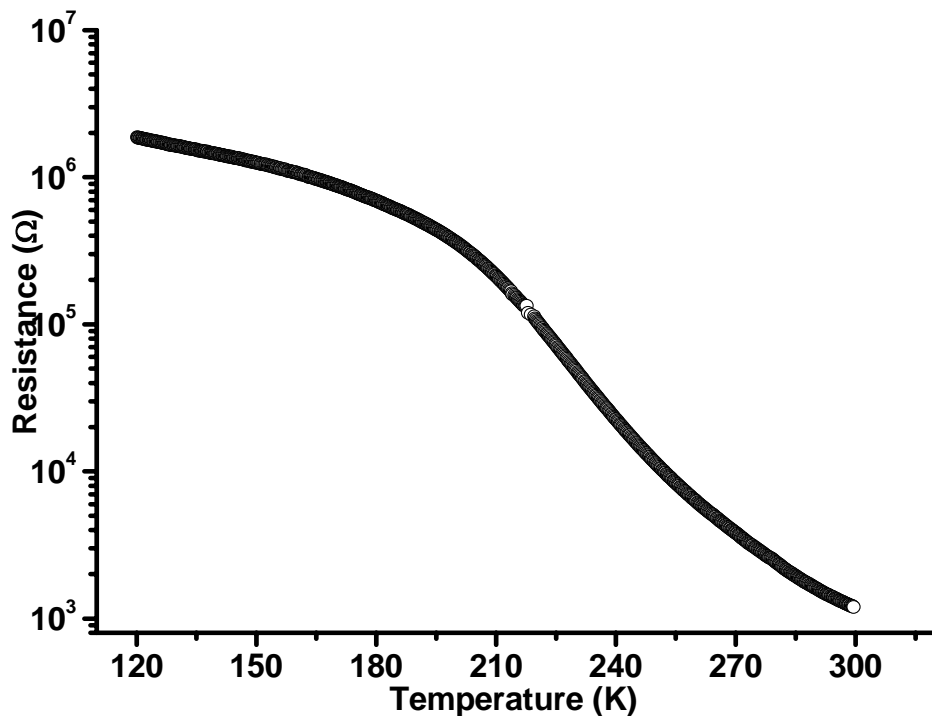


Figure 5.5. Electrical resistance characteristic of Bi nanowire arrays with diameter of 200 nm as a function of temperature (130-300 K)

$R(T)$ increases monotonically as the temperature decreases indicating a typical semiconducting characteristics. In general, a large change in $R(T)$ was found. The inconsistency with FT-IR data (semimetallic characteristic, figure 4.3) can be explained by the polycrystalline nature of the nanowires as discussed in chapter 2 as well as related to the mean free path dependence on temperature. $R(T)$ is increasing as the temperature decreases due to the increased boundary scattering which comes from the polycrystalline structure of Bi nanowires with a diameter of 200 nm, leading to a

monotonic resistance behavior as shown in figure 5.5.^[5.5]

Another possible explanation is that the resistance is determined by a delicate balance between the carrier concentration $n(T)$ and the mobility $\mu(T)$, which generally increases with decreasing temperature as the mean free path $l(T)$ grows. In bulk Bi, $l(T)$ grows from 0.2 to 0.3 μm at room temperature to as large as $\sim 100\mu\text{m}$ at $T = 4.2\text{ K}$, and the resistance decreases with decreasing temperature. In low dimensional Bi, $l(T)$ has less temperature dependence so that $n(T)$ has a large effect on $R(T)$.^[5.6] Therefore, the increase of resistance at low temperature shown in figure 5.5 indicates that $l(T)$ is cut off in this wires as well, that $n(T)$ determines $R(T)$ in our Bi nanowire with a diameter of 200 nm.

The temperature dependence of the resistance of Bi nanowires with diameters of 50 and 30 nm is shown in figure 5.6.

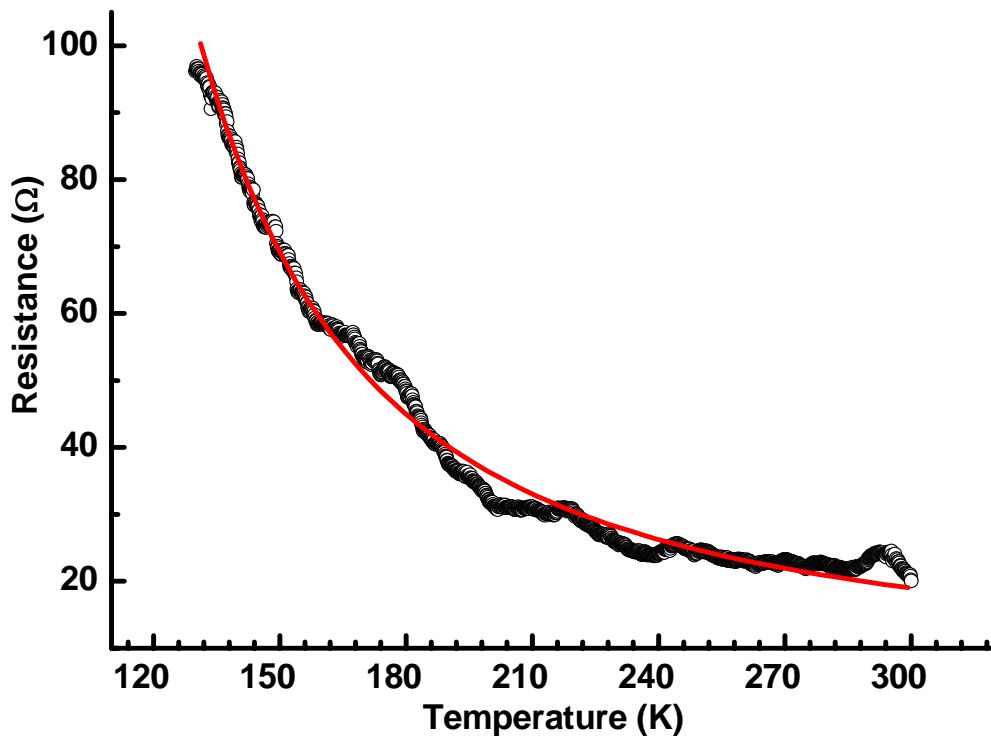


Figure 5.6. Electrical resistance characteristic of Bi nanowire arrays with diameter of 50 as a function of temperature (130-300K)

$R(T)$ is monotonically increasing as temperature decreases for the 50 nm arrays showing a typical semiconducting characteristic, consistent with FT-IR data (figure 4.3). Figure 5.6 exhibits the measured data (black squares) together with a theoretical fit

$=R_0 \exp\left(\frac{E_g}{2k_B T}\right)$ to it (solid red line). Here, R_0 is the asymptotic resistance value at $1/T$

$\rightarrow 0$, T is the temperature, k_B is the Boltzmann constant, and E_g stands for the semiconducting energy gap. Consequently, one arrives at $R_0 = 5.2 \Omega$ and $E_g = 67$ meV. The latter value, as expected, is smaller than the corresponding values (83 and 87 meV) obtained from optical absorption data for 30-nm-thick wires. The resistivity of 50-nm wires can now be estimated as follows. The resistance of an array can be written as $R = \left(\frac{4l}{\pi d^2}\right) \left(\frac{\rho}{N}\right)$. Here, $l = 15 \mu\text{m}$ is the wire length, $d = 50$ nm is the diameter, ρ is the electrical resistivity, and N designates the number of wires in the contacted area (around $700 \mu\text{m}^2$). Substituting for the corresponding values and with $R = 19 \Omega$ at room temperature, one gets $\rho / N \approx 2.5 \times 10^{-9} \Omega\text{m}$. With the pore density in our oxalic acid membranes of about $\sim 100 / \mu\text{m}^2$, and assuming a perfect electrical contact to all the wires, we obtain $\rho \sim 0.2 \times 10^{-5} \Omega\text{m}$. This value has to be compared to those obtained from the Hall measurements performed on high quality Bi slabs ($\rho \sim 0.5\text{-}2 \times 10^{-5} \Omega\text{m}$) presented in Ref. [5.7]. A comparison of this result to the former reports, in which no etching of the AAO surface and sputtering of a conductive contact electrode prior to electrical measurements were performed, as well as to the corresponding values for individual Bi nanowires deduced from 4-probe measurements ($1.12 \times 10^{-5} \Omega\text{m}$)^[5.8], proves the efficiency of this approach.

5. 4 2-Point Measurement at a Single Bi₂Te₃ Nanowire

For the measurement of the electrical conductivity of single nanowires, typically a metal (Pt) electrode is contacted by e-beam lithography or focused ion beam lithography technique^[5.9-11] to dispersed single nanowires in a vacuum chamber after selective dissolution of the template. However, the conducting AFM technique also allows to measure the electrical properties of individual nanowires without any complicated preparation procedure. Therefore, it is much easier to prepare the measurement of the electrical conductivity of individual nanowires. However, a native oxide layer may form on the top surface of the nanowire since the measurements are performed at ambient atmosphere. As already discussed in chapter 3, time dependent native oxide layer formation (Bi₂O₃ or TeO₂) may occur on the surface of Bi₂Te₃ nanowires when they are exposed to air. This problem can be overcome by an increased applied potential which

makes electrons tunnel through the oxide layer towards the Bi_2Te_3 nanowire, allowing to measure an electrical conductivity which however contains the effect of the tunneling resistance. The brief sample preparation procedure is illustrated in figure 5.7.

After the fabrication of the Bi_2Te_3 nanowires grown by pulsed electrodeposition at different off times, ion milling has been performed for the removal of the overgrown film as well as empty pores of the AAO matrix as shown in figure 5.7 (b). Subsequently, we employ an electrically conductive type AFM (AE-100 Park System AFM) which can be operated at ambient conditions.

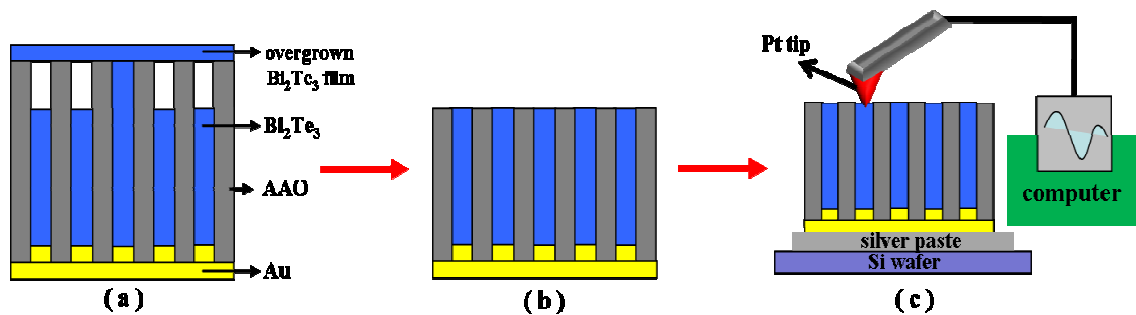


Figure 5.7. Illustration of the preparation of samples for the measurement of electrical conductivity of individual Bi_2Te_3 nanowires via an AFM tip

The feedback loop and data acquisition are implemented using a digital control system, which allows us to simultaneously monitor the desired input signal (applied potential). The platinum AFM tip (CSC18/Ti-Pt, MikroMasch) with a radius of 20-30 nm is approaching single Bi_2Te_3 nanowires, which are sticking out of the AAO. As the tip contacts an individual nanowire with 150 nN force, the potential is applied in the range of -5 and +5 V and then the corresponding current signal is recorded.

Figure 5.8 shows the topography of a nanowire array in the AAO membrane and the $I-V$ characteristics of a single Bi_2Te_3 nanowire fabricated by pulsed electrodeposition which is measured via the AFM tip.

An AFM topography, figure 5.8 (a), is investigated over a $4 \mu\text{m}$ square area with 1 Hz scan speed. The surface is somewhat rough and the bright spots are at a relatively higher plateau than the dark spots. Therefore, the tip is contacted to a bright spot. Figure 5.8 (b) displays the $I-V$ characteristic of a single nanowire. The way to obtain the corresponding current from the applied potential is that the applied potential starts at -5V and scans up to +5 V firstly and the next scan starts at +5 V and goes down to -5 V again.

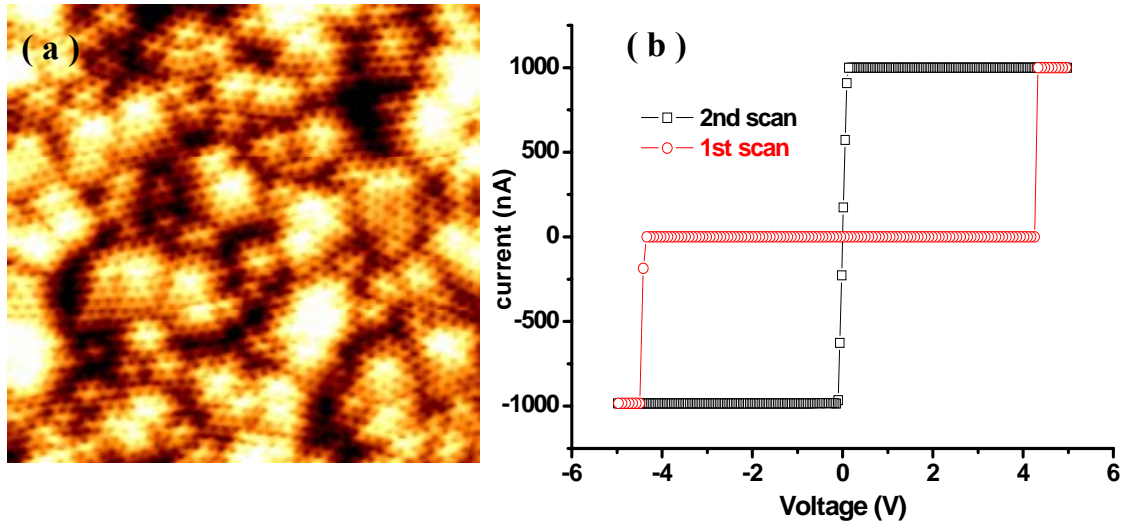


Figure 5.8. (a) A representative AFM topography of Bi_2Te_3 nanowire arrays in AAO after ion milling to top surface of AAO and (b) I - V characteristic of a single Bi_2Te_3 nanowire grown by pulsed electrodeposition with 50 ms off time (pu 50) [Note that the plateaus at the second scan comes from a current limitation of the measurement system]

Unlike a linear slope in the second scan (black line), the current hardly flows in most of potential range except significant rising current at -4.3 and +4.3V, indicating a breakdown phenomena.^[5.12-14] It indicates that electron carriers originated from the first scan can not penetrate through the Bi_2Te_3 nanowire due to the thin native oxide layer covering its top surface. However, the carriers can migrate through the oxide layer and nanowire during the second scan due to the breakdown effect caused by the first scan. The second scan shows a very good linear slope in the operating potential of -0.1 and +0.1 V range as an evidence of a good ohmic contact.

As shown in figure 5.9, a representative cross-sectional image of nanowires (pu 20) is observed for the measurement of the nanowire length (25 μm). A good preparation, ready to contact an AFM tip, is demonstrated in figure 5.9 (b). Figure 5.9 (c) shows a good ohmic contact of every single Bi_2Te_3 nanowire grown by pulsed electrodeposition with different off times. Finally, the electrical resistance can be obtained from figure 5.9 (d) according to Ohm's law. The electrical conductivity can be deduced from the resulting electrical resistance and the length and diameter of the nanowire. The electrical conductivity (δ) is proportional to length of nanowire and inversely proportional to area and resistance:

The measured electrical resistance is summarized table 5.1 and the calculated electrical conductivity is shown in figure 5.10.

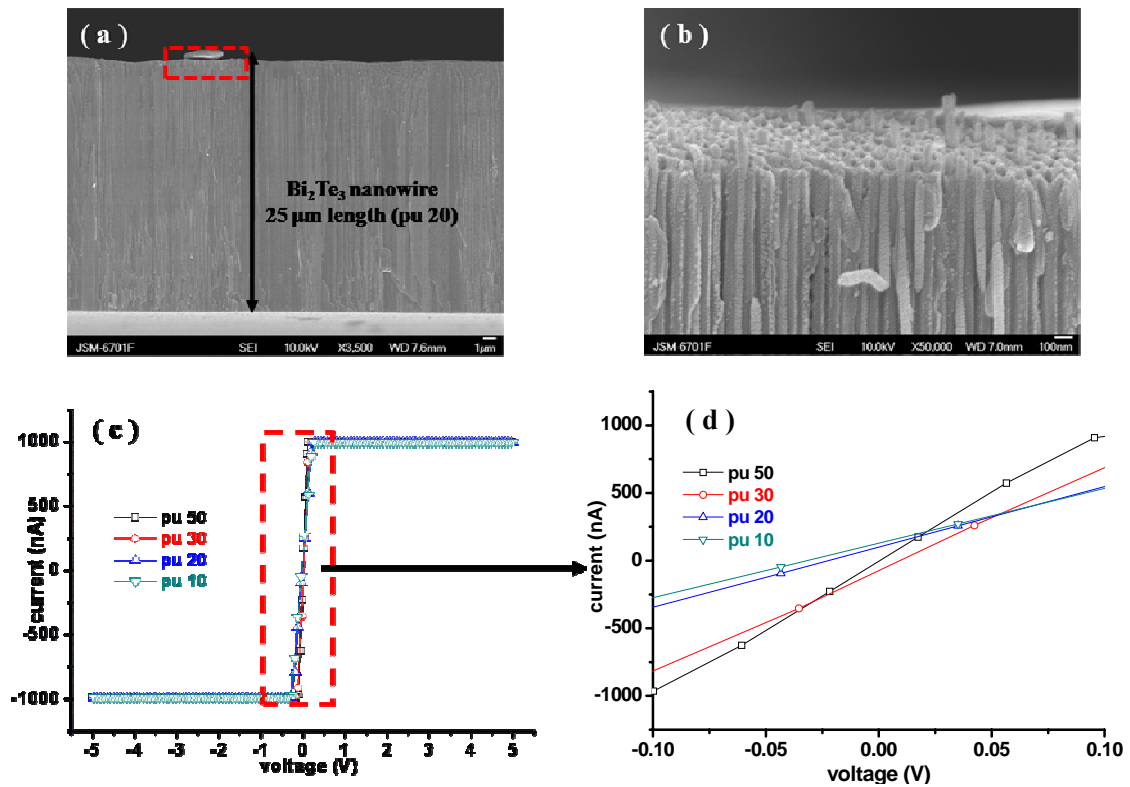


Figure 5.9. (a) A cross-sectional SEM image of Bi_2Te_3 nanowires grown by pulsed electrodeposition with 20 ms off time, (b) a magnified view of the rectangular area marked in (a), (c) I - V characteristic of single Bi_2Te_3 nanowires fabricated by pulsed electrodeposition with different off time (10, 20, 30 and 50 ms, pu 10, 20, 30 and 50 already abbreviated in chapter 1) and enlargement of the rectangular area marked in (c) (-0.1 ~ +0.1 V range)

$$\sigma = \left(\frac{L}{\pi d^2} \right) \left(\frac{1}{R} \right), \text{ < } d = \text{radius of nanowire, } L = \text{length of nanowire}$$

and $R = \text{electrical resistance}$ >

	pu 10	pu 20	pu 30	pu 50
resistance ($\times 10^5 \Omega$)	2.47	2.24	1.26	0.97
length (μm)	25	25	26	29

Table 5.1. The electrical resistance of single nanowires resulting from I - V characteristics measured by AFM-tip together with the individual length of the different nanowires (Note that the lengths of nanowires are slightly different caused by different ion-milling times)

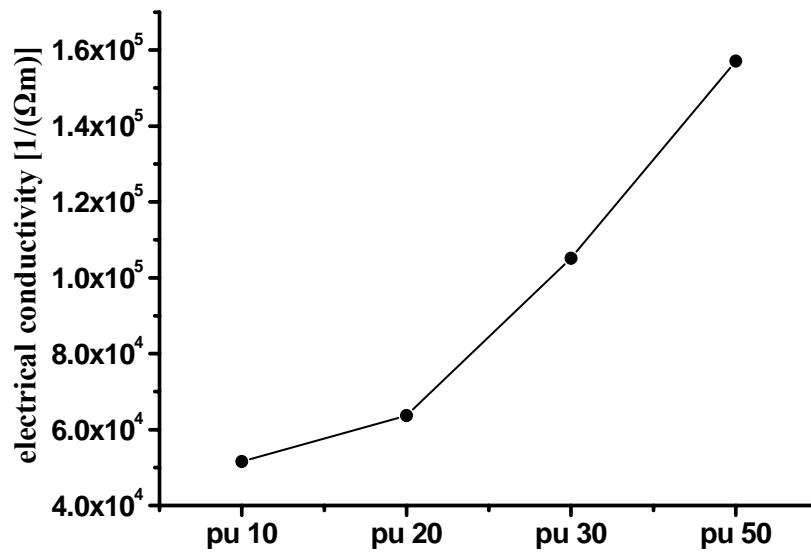


Figure 5.10. The electrical conductivity variations of Bi₂Te₃ nanowires fabricated by pulsed electrodeposition with different off times

The electrical resistance value is relatively higher than the one measured from a 4 point probe system due to the high contact resistance between the AFM-tip and the nanowires. Nevertheless, the electrical conductivity (0.05~0.16 [10⁶ / (Ω*m)]) is in a good agreement with previously reported values.^[5,15] Additionally, the electrical conductivity is enhanced with increasing off time, consistent with previous crystalline structure data (electron diffraction pattern, figure 1.8). It is verified that a longer off (relaxation) time has a positive effect on an improved crystalline structure of the Bi₂Te₃ nanowires.

This electrical conductivity is also measured for single Bi₂Te₃ nanowires annealed at different temperatures by means of the same method. After the samples are prepared following the previous procedure (figure 5.7), the AFM tip contacts the single nanowires exposed out of the AAO.

As shown in figure 5.11 (a), a thin oxide layer is observed forming a shell structure covering the nanowires. Two reasons can be assumed for the formation of this oxide layer: (1) a formation during the annealing process, with a varying thickness due to the different annealing temperatures (2) a formation due to an exposure of the sample to air.

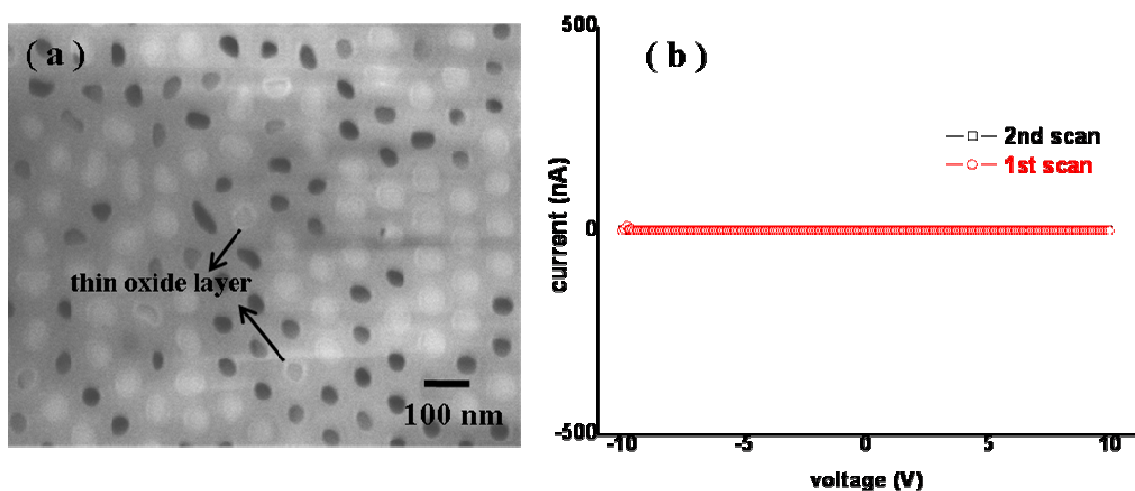


Figure 5.11. (a) A representative top surface image of Bi_2Te_3 nanowires annealed at 150°C and (b) I - V characteristics of a single nanowire measured by an AFM tip (Different colors of the left image are caused by the rough surface of the AAO martix)

The I - V characteristics of a single Bi_2Te_3 nanowire annealed at 150°C is shown in figure 5.11(b). As expected, a linear plot is not found in the cyclic potential scan due to a thin oxide layer which does not allow any breakdown at voltages below 10 V. Although the applied potential is increased (-10 to +10V), the current hardly flows, indicating that the carriers can not penetrate through the oxide layer despite of an increased driving force (the applied potential range is limited by the power supply). In contrast to the linear plot for single nanowires, which are not annealed, despite of the existence of an oxide layer, annealed nanowires are covered by oxide layers in such a way that no tunneling is possible for the voltage range investigated.

5.5 4-Point Measurement of Single Bi_2Te_3 Nanowire

A 4-point probe electrical measurement on individual nanowires is performed to evaluate the conductivity of the nanowire. Electrical contacts between the nanowire and the microelectrode (Pt) are achieved with the help of a focused ion beam (FIB) lithography process. The preparation process is described in figure 5.12.

Similarly as for the preparation for TEM samples, nanowires are dispersed in ethanol after selective dissolution of the AAO membrane. Several droplets of this solution are placed on a Si substrate with a circuit pad.

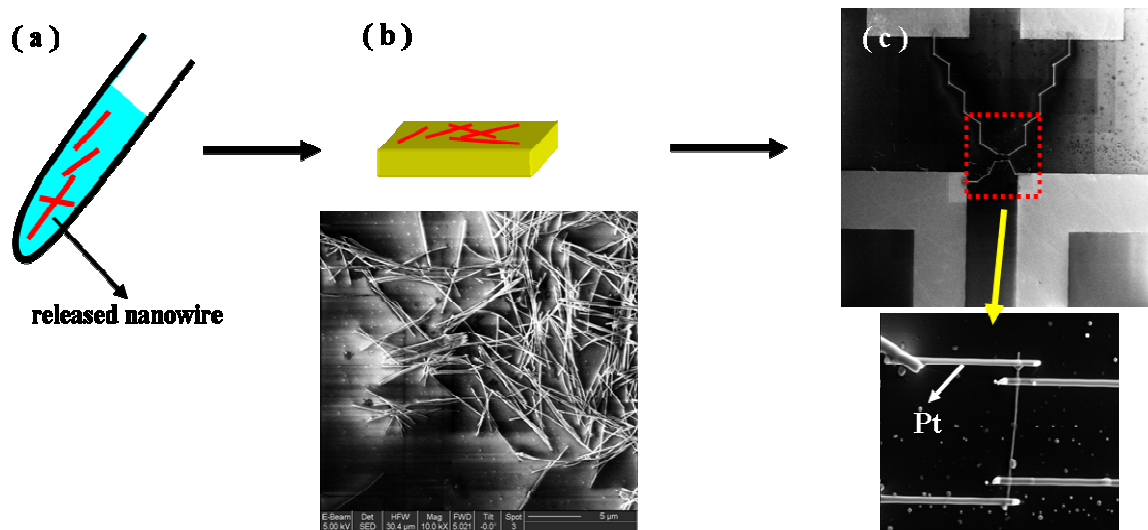


Figure 5.12. (a) Dispersed nanowires in ethanol (C_2H_5OH) after selective etching away the AAO in 2 M NaOH, (b) dispersed nanowires on Si substrate with circuit pad and (c) Bi_2Te_3 nanowire contacted with Pt microelectrode by using FIB lithography

Subsequently, a single nanowire which is dispersed at a convenient position is contacted with Pt metal microelectrodes via FIB lithography. In this state, a small current ($-100 \sim +100$ nA) is applied through the individual nanowire and the corresponding voltage is recorded. Figure 5.13 shows the I - V characteristics for this single nanowire. Unfortunately, only a Bi_2Te_3 nanowire grown by galvanostatic methods is investigated.

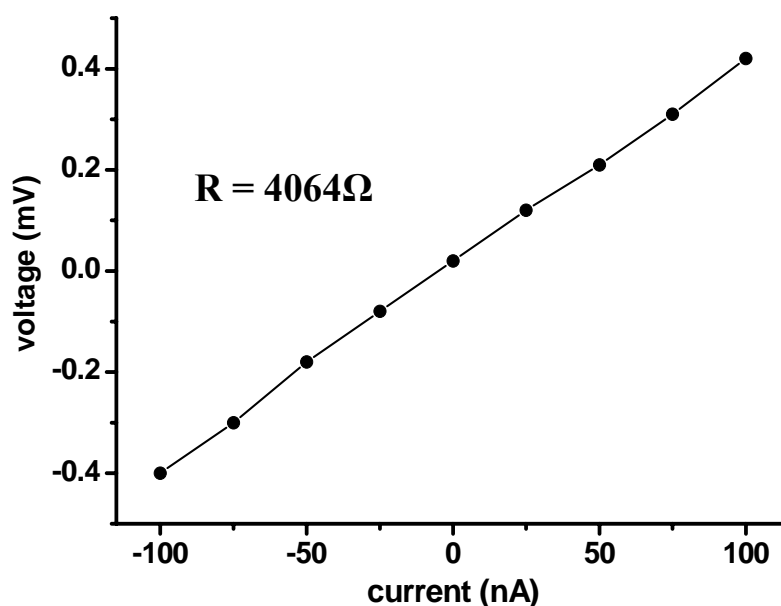


Figure 5.13. I - V characteristic for single Bi_2Te_3 nanowire grown by the galvanostatic (2.5 mA/cm^2) method

The calculated resistance via Ohm's law gives 4064 Ω . From this resistance, the electrical conductivity can be deduced. The essential parameters for the calculation of electrical conductivity (length and diameter of nanowire) are 1.5 μm and 50 nm, respectively. Finally, we can obtain the electrical conductivity (0.188 [$10^6 / (\Omega \cdot \text{m})$]). This value is higher than the one measured by the AFM-tip for the pu 50 sample (0.16). The eliminated contact resistance contribution in the 4-probe measurement system should lead to a higher conductivity that measured via 2-point probe measurement system.^[5.11]

5. 6 Conclusions of Chapter 5

Several methods have been evaluated in order to characterize the electrical resistance of Bi_2Te_3 nanowire arrays and of individual Bi_2Te_3 nanowire(s) as well as arrays of Bi nanowires. The electrical resistance of arrays of Bi_2Te_3 nanowires fabricated by pulsed electrodeposition with different off time decreases with increasing temperature (200 ~ 470 K). This is an indication of a typical semiconducting characteristics. In addition, the electrical resistance behavior of Bi nanowire arrays with diameters of 200 and 50 nm also indicates a semiconducting characteristics. Unexpectedly, a semiconducting resistance behavior of the polycrystalline structure of Bi nanowires with a diameter of 200 nm is found an interpreted routine as deriving from an increased boundary scattering.

For a precise investigation of the electrical conductivity of Bi_2Te_3 nanowires, a conductive AFM tip with a radius of 20 ~ 30 nm is employed to measure the electrical conductivity of individual nanowires. This approach has the advantage of an easier sample preparation and a conventional measurement. The electrical conductivity of Bi_2Te_3 nanowires fabricated by pulsed electrodeposition with different off times is in the range of 0.05~0.16 [$10^6 / (\Omega \cdot \text{m})$], in agreement with literature. However, the electrical conductivity of thermally annealed nanowires can not be obtained due to an oxide layer on the surface of the annealed nanowires. Consequently, several approaches can be suggested: (1) production of an Au- Bi_2Te_3 -Au nanowire structure or (2) FIB deposition of a Pt layer on a micrometer scale area on Bi_2Te_3 nanowire arrays in order to prevent the formation of an oxide layer. Finally, the electrical conductivity (0.18 [$10^6 / (\Omega \cdot \text{m})$]) of a single Bi_2Te_3 nanowire grown by the galvanostatic method is also obtained from a 4-probe measurement system with Pt microelectrodes contacted to an individual nanowire by focused ion beam lithography.

Chapter 6

Measurement of the Seebeck Coefficient in Bi_2Te_3 Nanowires

In this chapter we demonstrate how to measure the Seebeck coefficient of Bi_2Te_3 nanowire arrays at room temperature. The description of the preparation method is introduced as well as the measurement system. The obtained data on the power factor ($S^2 \cdot \sigma$) of Bi_2Te_3 nanowires fabricated by pulsed electrodeposition with different off time is discussed.

6. 1 Seebeck Coefficient

The Seebeck coefficient S has two contributions, $S = S_d + S_g$. S_d is the contribution from the charge carrier diffusion and S_g from the phonon drag effect due to additional charge carriers dragged by the phonon flow.

As mentioned in the introduction, the hot electrons diffuse from the hot end to the cold end whereas the cold electrons diffuse in the opposite direction due to different charge carrier concentration of the hot and cold side assuming that a temperature gradient exists across a material in which no net current flows. The electrons scatter with phonons, impurities, crystalline defects and boundaries in the diffusion process. If the scattering rate is energy dependent, the diffusion rates for the hot electrons with higher energy and the cold ones with lower energy are different. The net flow of diffused electrons leads to an accumulation of electrons at one end and leaves the other end to be

positively charged.^[6.1] The electrical field built across this conductor opposes the net diffusion of the electrons. When an equilibrium state is reached, the net diffusion flux of electrons equals the net drift flux of electrons under the electrical field in the opposite direction. Finally, the difference of potential between the hot and cold ends of the material is determined by the Seebeck coefficient as $\Delta V = S\Delta T$.

For a p-type semiconductor with holes as the major charge carriers, a temperature gradient drives the holes from the hot end to the cold one, and the potential at the hot end is measured to be negative. Therefore, the p-type semiconductor has a positive S. In the case of n-type semiconductor, these processes apply vice versa, with a negative S.

S_d can be derived from the Boltzmann transport equation.^[6.2] Assume the mean free path of carriers l depends on energy ε and has a form

$$l \sim l_0 \varepsilon^r \quad [1]$$

where l_0 and r are constants. The quantity r is often referred to as the scattering constant. The scattering mechanisms in the carrier diffusion process include carrier-phonon scattering, carrier-impurity scattering, carrier-crystal defect scattering and alloy scattering. Carrier scattering usually is not important in the range of temperature of interest.^[6.3]

For non-degenerate semiconductors, S_d is a function of the Fermi energy measured from the band edges and can be expressed as

$$S_d = \frac{-k_B}{|e|} \left(r + \frac{5}{2} + \frac{E_c - E_f}{k_B T} \right) \quad \text{for n - type} \quad [2]$$

$$\frac{k_B}{|e|} \left(r + \frac{5}{2} + \frac{E_f - E_v}{k_B T} \right) \quad \text{for p - type}$$

where E_c , E_v are the conduction band edge (for electrons) and the valence edge (for holes) energies.^[6.4]

The other contribution to the Seebeck coefficient arises from the so-called phonon drag effect. When a temperature gradient is applied to a solid, phonons moving from the hot end to the cold one outnumber phonons moving in the opposite direction, and there is a net phonon flow from the hot end to the cold end.^[6.2] As a result of interactions between phonons and carriers, this flow of phonons drags a flow of charge carriers in the same direction. Consequently, the accumulation of carriers in the cold end forms an electrical field which works against the motion of the charge carriers. At equilibrium, the potential difference is established across the solid and makes an additional phonon drag

contribution (S_g) to the Seebeck coefficient.

In a semiconductor, S_d and S_g have the same signs because they both take the sign of the majority charge carriers. If impurities are introduced into the solid, S_g may drop off sharply while S_d may increase or decrease.^[6,3]

6.2 Preparation for the Measurement of Seebeck Coefficient

In figure 6.1, the preparation for the measurement of the Seebeck coefficient is described.

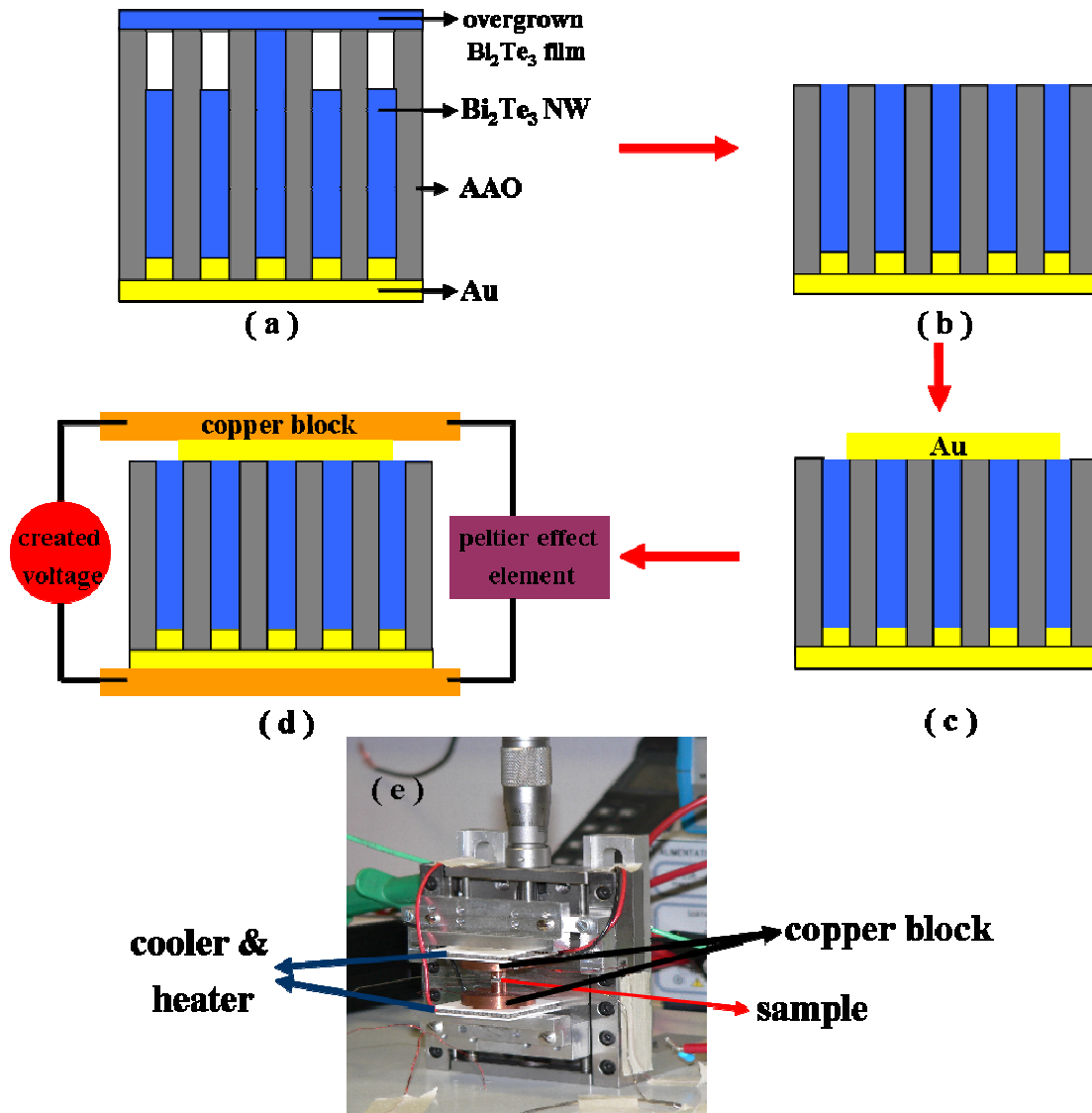


Figure 6.1. Schematic diagram of the preparation procedure (a~d) for the measurement of the Seebeck coefficient and (e) a photograph of the measurement set-up

Bi_2Te_3 nanowires overgrown by electrochemical deposition and empty pores of the AAO membrane are eliminated by an ion-milling process and subsequently a thin Au layer is sputtered onto the AAO membrane through a circular mask with an area of 0.78mm^2 . The Au layer should be deposited very carefully in order to prevent the deposition of a Au layer on the edge of the AAO membrane which would cause a short circuit during the measurement of the Seebeck coefficient. This prepared sample is placed in between 2 pieces of a copper block whose temperatures are individually controlled with Peltier elements. The temperature difference is kept to 15 K. As soon as a stable temperature gradient (15 K) has been reached, the voltage between two ends of the nanowires is measured with a multimeter.

6.3 Seebeck Coefficient Variations for Bi_2Te_3 Nanowires

Firstly, the Seebeck coefficients of bismuth telluride nanowires, which have not been annealed, are measured and plotted as a function of relaxation time of the pulsed electrodeposition as shown in figure 6.2.

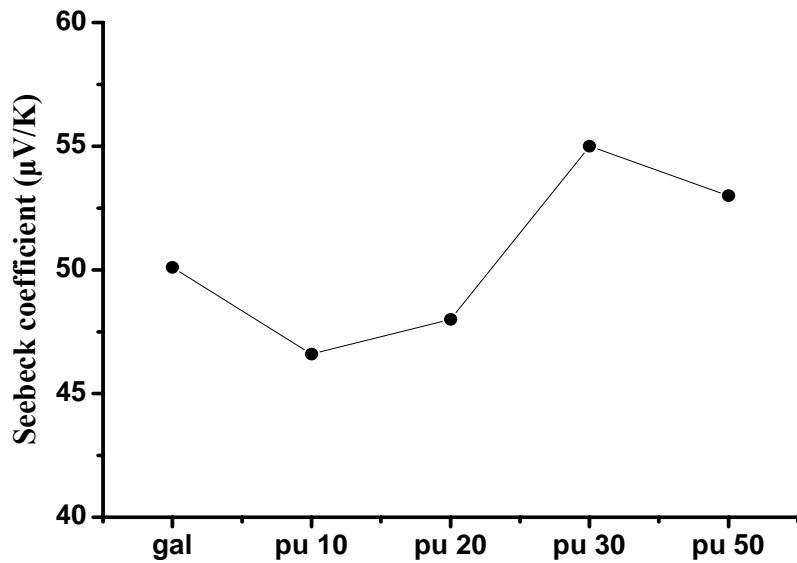


Figure 6.2. Seebeck coefficient values of bismuth telluride nanowires grown by galvanostatic and pulsed electrodeposition with different relaxation time

Since the measurements of the Seebeck coefficient are independent of the number of measured nanowires, these measurements are as informative as single nanowire measurements.^[6.5] All the nanowires show a positive value indicating that bismuth telluride nanowires grown at this condition have a p-type semiconducting characteristics.

Since the thermopower (Seebeck coefficient) depends on the material's temperature and crystal structure as well as chemical composition of nanowires, an elemental analysis is performed by EDX attached to a TEM. Bismuth telluride nanowire arrays are dispersed on a TEM grid after dissolving the AAO membrane selectively for the detection of the atomic amounts of Bi and Te as shown in figure 6.3. The two peaks at ~ 5.3 and ~ 8.1 eV arise from the copper TEM grid. Additionally, the atomic ratio in the nanowires is summarized in table 6.1.

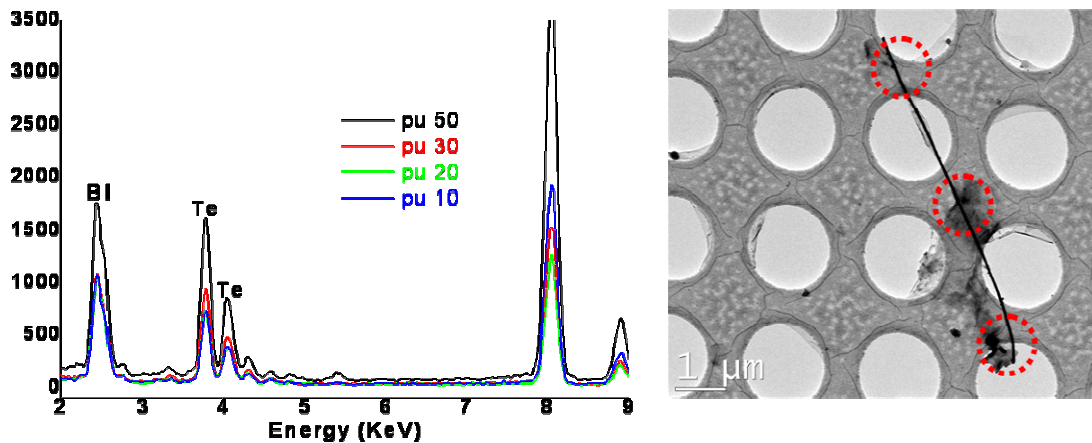


Figure 6.3. Energy dispersive x-ray spectroscopy (left) and TEM image (right) of bismuth telluride nanowires grown by pulsed electrodeposition with different off time

Sample	Cu K	Te L	Bi L	Atomic ratio (Te/Bi)
pu 10	68.22	16.12	15.66	1.029
pu 20	66.69	18.15	15.18	1.195
pu 30	62.52	21.26	16.22	1.311
pu 50	66.69	19.04	14.29	1.332

Table 6.1. The atomic percentage and atomic ratio in the nanowires (pu series)

As shown in figure 6.3, 3 indicated areas are measured and the detected values are summarized as an average in table 6.1. Bi and Te are detected in all nanowires with different atomic ratios. The atomic ratio of Te to Bi becomes stoichiometrical near to 1.5 as the relaxation time increases in the pulsed electrodeposition, indicating that the composition can be controlled by relaxation time.

Compared to the values (260, 160 $\mu\text{V/K}$) measured by other groups^[6.3, 5.3], the lower values in figure 6.2 are attributed to an unoptimized doping concentration, leading to a low carrier concentration. Nevertheless, pu 50 has the highest (55 $\mu\text{V/K}$) value among

all data, most likely due to an increased hole concentration caused by the Bi-rich composition of the nanowire.

The Seebeck coefficient of Bi_2Te_3 nanowires annealed at different temperatures is investigated by means of the same method.

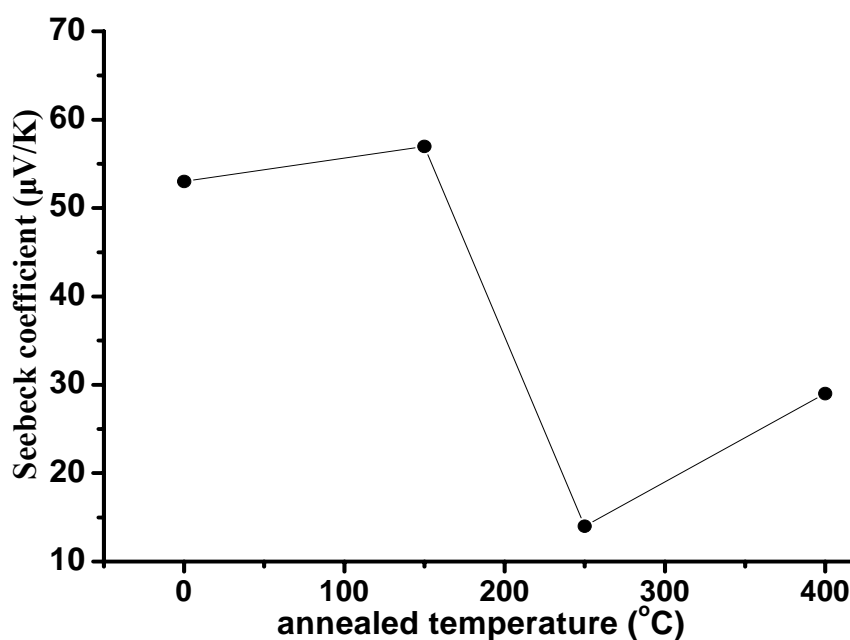


Figure 6.4. The seebeck coefficient variations of Bi_2Te_3 nanowires as a function of annealing temperature

The Seebeck coefficient of nanowires annealed at different temperatures is determined from the plot of the measured Seebeck voltage versus the temperature difference across the specimen. The Seebeck coefficient of nanowires annealed at 150°C shows the highest value ($57\mu\text{V/K}$) with an around 8 % increase compared to as-prepared nanowires (pu 50), and is significantly decreased down to $19\mu\text{V/K}$ (64% reduction) with increasing annealing temperature. The reduction of the Seebeck coefficient with increasing annealing temperature is presently not understood well. Nevertheless, an assumption can be suggested. The Seebeck coefficient is decreasing due to the change of the composition, as already discussed in chapter 3. The ratio of surface to volume is quite high in 1D nanostructures. Therefore, the composition of the nanowire can be easily changed during the annealing at certain temperatures. It is well known that the seebeck coefficient is inversely proportional to the carrier concentration. The carrier concentration is increased with increasing annealing temperature because of an increasing Te deficiency (figure 3.3 indicates that the composition of nanowires become

Bi-rich with increasing annealed temperature).

Finally, the power factor of Bi_2Te_3 nanowires fabricated by pulsed electrodeposition with different off time can be calculated from the Seebeck coefficient and the electrical conductivity. The power factor P is given by $P = S^2 \times \sigma$ (P = power factor [W/mK^2], S = Seebeck coefficient [V/K] and σ = electrical conductivity [$1/(\Omega\text{m})$]).

Unfortunately, the power factor of the annealed nanowires can not be obtained because of the failure to measure the electrical conductivity.

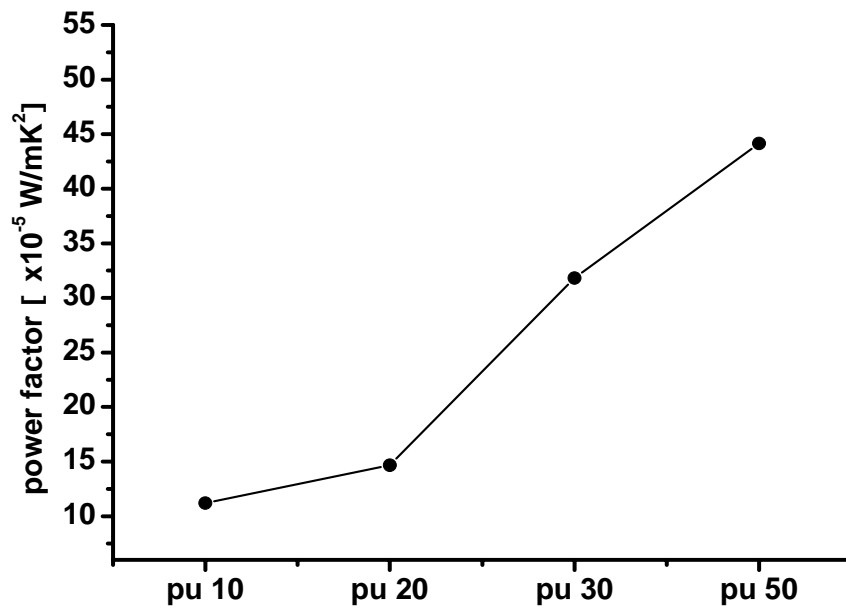


Figure 6.5. The power factor (PF) variations of Bi_2Te_3 nanowires fabricated by pulsed electrodeposition with different off time

The power factor of Bi_2Te_3 nanowires grown by pulsed electrodeposition with an off time higher than 30 ms is distinctly increased. The significant increase of the electrical conductivity mainly affects the value of the power factor as well as the small increase of Seebeck coefficient. The largest value of power factor ($4.41 \times 10^{-4} \text{ W}/\text{mK}^2$) is obtained for the pu 50 sample with the most stoichiometric composition (ref. table 6.1), where the carrier concentration is optimized and the electrical conductivity and the Seebeck coefficient have their maxima in the scope of the present experimental condition.

6. 4 Conclusions of Chapter 6

The Seebeck coefficient of Bi_2Te_3 nanowires fabricated by pulsed electrodeposition

with different off times and annealed at different temperatures is investigated by a simple method. All Seebeck coefficients show a positive value, indicating a p-type semiconductor. The Bi₂Te₃ nanowires annealed at 150°C have the highest Seebeck coefficient (57μV/K). Additionally, the power factor variation can be deduced from the electrical conductivity and the Seebeck coefficient of Bi₂Te₃ nanowires fabricated by pulsed electrodeposition with different off time. The nanowires with 50 ms off time (pu 50) show the highest value (441.4 μW/m-K²), indicating the relatively optimized carrier concentration within the experimental conditions investigated in this thesis.

sample (type)	diam.(nm)	S (μV/K)	δ [$10^6/(\Omega\text{m})$]	PF (μW/m-K ²)	Ref.
pu 10 (Bi _{0.49} Te _{0.51})	50	46.6	0.052	112.0	-
pu 20 (Bi _{0.46} Te _{0.54})	50	48	0.064	146.7	-
pu 30 (Bi _{0.44} Te _{0.56})	50	55	0.105	318.1	-
pu 50 (Bi_{0.43}Te_{0.57})	50	53	0.157	441.4	-
150C (Bi _{0.42} Te _{0.58})	50	57	-	-	-
250C (Bi _{0.52} Te _{0.48})	50	14	-	-	-
400C (Bi _{0.55} Te _{0.45})	50	29	-	-	-
Bi _{0.46} Te _{0.54} (NW)	100	260	-	-	[6.6]
Bi _{0.46} Te _{0.54} (NW)	57/43	-	0.17 / 0.20	-	[6.6]
Bi _{0.46} Te _{0.54} (bulk)	-	160	0.1	2560	[6.7]
Bi _{0.54} Te _{0.46} (NW)	81	-30	0.07	63	[6.6]
Bi _{0.45} Te _{0.55} (film)	-	-45.5	0.16	331.2	[6.8]
Bi _{0.45} Te _{0.55} (film)	-	-58.2	0.08	270.1	[6.8]
Bi _{0.08} Sb _{0.44} Te _{0.48} (bulk)	-	210 at 100°C	0.088 at 100°C	3750 at 100°C	[6.9]

Table 6.2. Thermoelectric properties (Seebeck coefficient and electrical conductivity) of individual nanowires, film and bulk materials compared to our measured values and the values measured by other groups. Their values are taken from literature (last column)
**(Thermal conductivity (κ) of bulk and nanowire: $\kappa_{\text{bulk}}^{[6,6]} = 1.7$ and $\kappa_{\text{NW}}^{[6,6,9]} = 1.05$ [W/m-K])*

A more detailed comparison is summarized in table 6.2 between our measured values (Seebeck coefficient and electrical conductivity) and the previously reported ones (including bulk and two film structures). The electrical conductivities found in our experiments are somehow similar and even better but the Seebeck coefficient is much lower than reported in the literature. This indicates that the composition of our nanowires is not optimized. In particular, there appears to be a large Te deficiency in our

annealed nanowires.

The low Seebeck coefficient can be overcome by doping with other materials, such as Antimony (Sb) or Selenium (Se), or by an annealing under controlled Te atmosphere for the optimization of the nanowire composition, leading to an increased Seebeck coefficient. The Seebeck coefficient of bulk Bi-Sb-Te nanocomposites shows 210 $[\mu\text{V}/\text{K}]^{[6.9]}$, 4 times higher than our best value.

Assuming that the thermal conductivity of our nanowires has the range of bulk $(1.7[\text{W}/\text{m}\cdot\text{K}])^{[6.6]}$ to nanowire $(1.05[\text{W}/\text{m}\cdot\text{K}])^{[6.6,9]}$ reported by other groups, the dimensionless thermoelectric efficiency, figure of merit of the pu 50sample has the range of **0.0793** to **0.129** at room temperature. In particular, if antimony would be appropriately doped in our nanowires like the Bi-Sb-Te nanocomposites given by the reference 6.9, the figure of merit could increase significantly to the range of **1.26** to **2.09**.

Chapter 7

Rough Bi₂Te₃ Nanowires Fabrication in Pulse-anodized AAO

The thermoelectric efficiency depends on the thermal conductivity in an inverse relationship.^[1,2] Recently, silicon nanowires with rough surfaces have been demonstrated as good candidates for low dimensional thermoelectric materials showing a significant reduction of their thermal conductivity.^[1,24] The roughness at the nanowire surface behaves like secondary scattering phases.^[7,1-2] The surface roughness may contribute to higher rates of diffuse reflection or backscattering of phonons at the surfaces. In other words, it is suspected that the roughness plays a strong role in screening a broad spectrum of phonons, fundamentally altering phonons transmission through the confined structure. Consequently the ZT (thermoelectric figure of merit) enhancement can be attributed to a reduction in thermal conductivity.^[1,2] Independently, the theoretical assumption that a rough surface of the nanowire can reduce the thermal conductivity is demonstrated by using the specular parameter included in the formula of Ziman.^[7,3]

Based on this idea, rough Bi₂Te₃ nanowires are fabricated by pulsed electrochemical deposition in porous templates grown by pulsed anodization. Pulsed anodization consists of a combination of mild (MA) and hard anodization (HA). All nanowires were fabricated in alumina template prepared by mild anodization with smooth pore wall and constant pore diameter. On the other hand, the pore diameter of the pulsed anodized AAO membrane can be periodically modulated due to the combination of mild and hard anodization.^[7,4] Recent studies have shown that the inter-pore distance of AAO formed

under mild anodization conditions using H_2SO_4 , $\text{H}_2\text{C}_2\text{O}_4$ and H_3PO_4 is linearly dependent on the applied potential, with a proportionality constant $\zeta_{\text{MA}} = 2.5 \text{ nmV}^{-1}$.^[E.1] The proportionality constant $\zeta_{\text{HA}} = 1.8\text{-}2.0 \text{ nmV}^{-1}$ for AAO films formed by hard anodization turned out be lower than for the mild anodization.^[7.5-7] Therefore, as different potentials are applied periodically for mild and hard anodization, the pore diameter is modulated during the pulse anodization process. Consequently, rough nanowires can be fabricated from pulse-anodized alumina templates by electrochemical deposition.

7.1 Fabrication of Pulse-anodized AAO Membrane

The electropolished Al chip was first anodized under an applied voltage of 25 V from 0.3 M H_2SO_4 for 24 hrs (at 8°C). Subsequently, the anodized alumina film was selectively dissolved in a mixture of 1.8 wt% chromic acid and 6 wt% phosphoric acid (H_3PO_4). The pulse anodization was performed on the textured Al substrate. Pulse anodization was carried out under potentiostatic conditions by applying a series of potential pulses comprising a MA pulse (25 V and 180 sec) followed by a HA pulse (35 V and 0.5 sec) in 0.3 M H_2SO_4 acid. The pulsed potential anodization process and its modulated pore structure are described in figure 7.1.

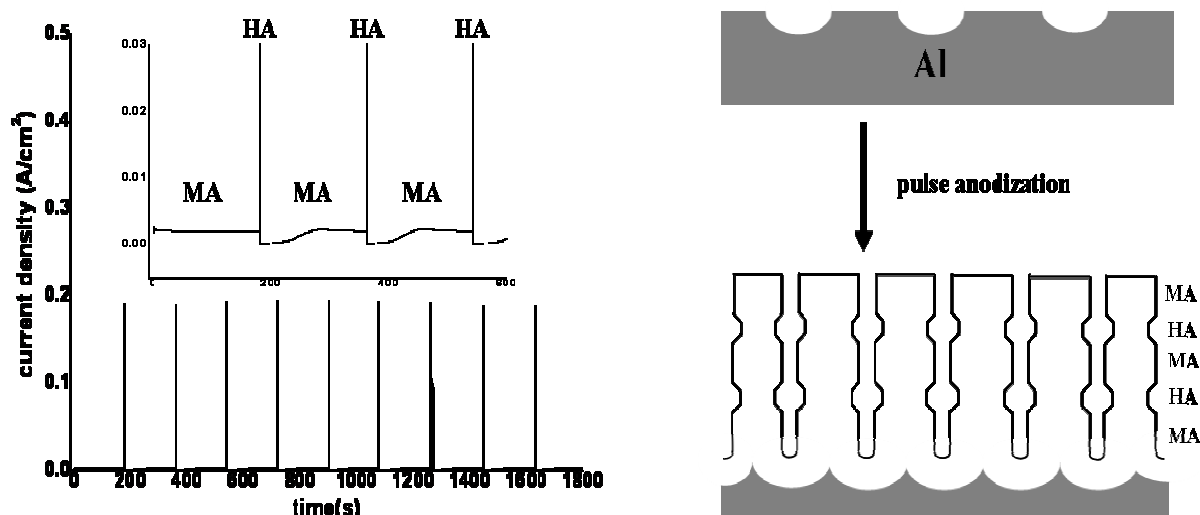


Figure 7.1. The corresponding current density profile during pulse anodization (left) and schematic of the fabrication of AAO with modulated pore diameters by pulse anodization (right)

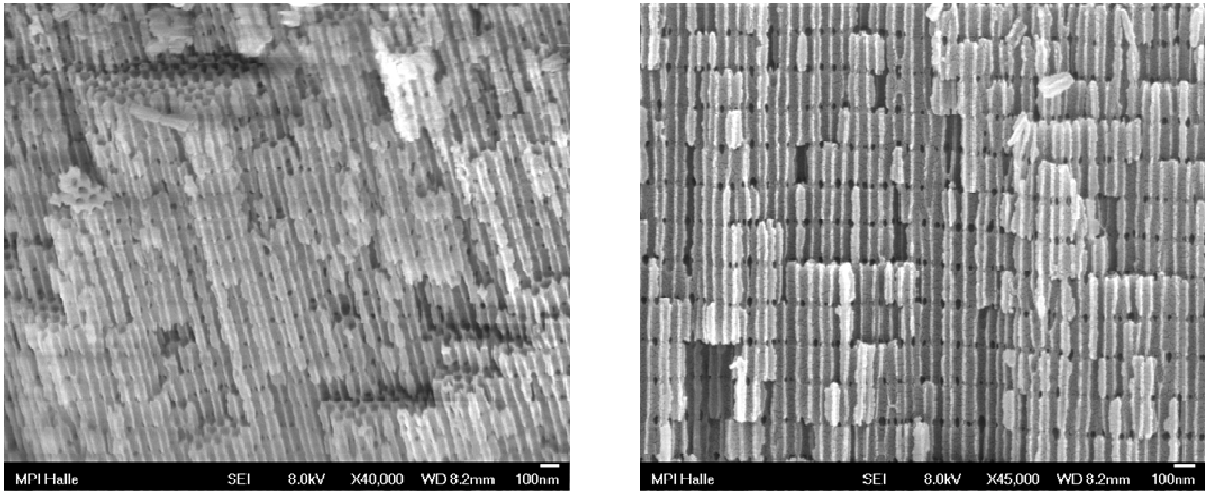


Figure 7.2. A representative cross-sectional SEM image of AAO prepared by pulsed potential anodization

As shown in figure 7.2, pore modulation is observed in the cross-sectional SEM image. The MA-AAO and HA-AAO exhibit different fracture modes due to the different applied potential at each anodization process (MA: 25 V and HA: 35 V).

7. 2 Fabrication of Rough Bi_2Te_3 Nanowires

After pulsed AAO is fabricated, a barrier layer still remains at the bottom of the AAO. For a growth of nanowires in the pores, it is necessary to accomplish an etching of the barrier layer. Therefore, reactive ion etching (RIE) is exploited, as mentioned in chapter 2, in order to remove a barrier layer. The previously applied wet chemical removal procedure with 5 wt% phosphoric acid (H_3PO_4) is not employed here due to the weak stability of pulsed AAO toward acidic bases. In the channel structure of the pulse-anodized AAO, Bi_2Te_3 nanowires are fabricated by pulsed electrodeposition from aqueous solution following the previous procedure (pu 50 sample) after Au sputtering and electrodeposition.

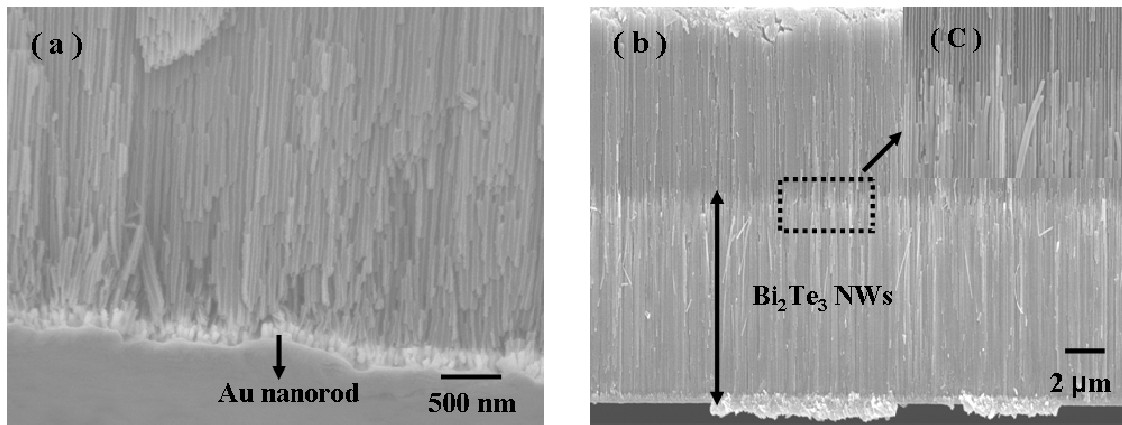


Figure 7.3. (a) Au nanorods prepared by sputtering and galvanostatic (1 mA/cm²) electrochemical deposition and (b) a cross-sectional SEM image of Bi₂Te₃ nanowires grown by pulsed electrodeposition in pulsed anodized AAO (inset (c): selectively magnified area).

After the preparation of Au nanorods, Bi₂Te₃ nanowires are fabricated very well by pulsed electrodeposition in pulse-anodized AAO as shown in figure 7.3. Subsequently, the elemental analysis of individual rough Bi₂Te₃ nanowires is performed by EDX attached to a TEM using a point scan.

Rough Bi₂Te₃ nanowires are dispersed on a TEM Cu grid after the selective etching of the Au nanorods and the pulse-anodized AAO matrix by using KI₃ solution and 2 M NaOH, respectively. The diameter of the nanowires is periodically modulated by means of the alternative use of the mild and hard anodized process as shown in figure 7.4(a). In addition, EDX data (figure 7.4(b)) indicate that the composition of this nanowire is done to the ratio of bismuth to tellurium of 2:3 as expected for a stoichiometrical Bi₂Te₃ phase.

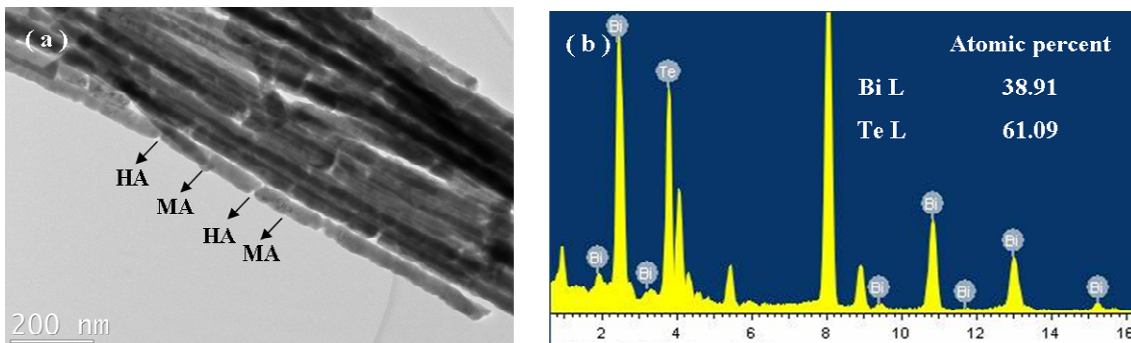


Figure 7.4. (a) Dispersed rough Bi₂Te₃ nanowire arrays on a TEM grid and (b) the composition of individual nanowires under EDX investigation

7.3 Conclusions of chapter 7

Bi_2Te_3 nanowires with rough surface are fabricated in pulse-anodized AAO membranes by using a pulsed electrodeposition. The pore structure of the AAO template is modulated by pulse anodization consisting of a series of mild and hard anodization. Rough Bi_2Te_3 nanowires grown by pulsed electrodeposition in such templates show a stoichiometrical Bi_2Te_3 composition from EDX.

In future work, the thermal conductivity of nanowire should be measured for the investigation about increased phonon scattering due to the periodically modulated nanowires from pulsed anodized alumina template. It is expected that the modulation of the diameter of nanowires acts as a secondary phonon scattering. Therefore, it should affect to an increased phonon scattering, leading to reduced lattice thermal conductivity of the nanowire, as observed for silicon nanowires.^[1,24]

Summary

This thesis has focused on the synthesis of thermoelectric bismuth telluride and bismuth in 1-dimensional structures by electrochemical deposition based on anodic aluminum oxide (AAO) membranes as a template as well as the investigation of the electronic properties of the nanowire. The synthesis of bismuth telluride and bismuth nanowires was discussed in chapter 1 and 2. Our attempts to enhance the electrical properties of bismuth telluride nanowires by means of annealing at different temperatures were discussed in chapter 3. The optical characterization of bismuth nanowires with different diameters was the subject of chapter 4. The electrical properties of bismuth telluride nanowires fabricated by pulsed electrodeposition with different off times and bismuth nanowires with different diameters was discussed and a novel approach to measure the electrical conductivity of individual nanowires by using an AFM tip with a radius of 20~30 nm was introduced in chapter 5. The Seebeck coefficient of bismuth telluride nanowire arrays was dealt with in chapter 6 as well as the synthesis of bismuth telluride nanowires with rough surfaces in chapter 7.

Bismuth is a semimetal with a highly anisotropic Fermi surface. Its physical properties depend strongly on the size and the crystal structure of the specimen. At lower dimensions, these dependencies become even more important. Therefore, having a precise control of the size and growth of low-dimensional bismuth structures would be of vital importance for a systematic study of this material at reduced dimensions. Therefore, a novel approach, Atomic Layer Deposition (ALD) was employed for the fabrication of diameter reduced Bi nanowires. In this thesis, the method involves of ALD of an insulating silicon dioxide (SiO_2) layer directly onto the pore wall. The pore diameter was tuned very precisely by the applied number of ALD cycles. Bi nanowire arrays with wire diameter of 200, 50 and 30nm are optically characterized by the FT-IR measurement as an evidence of the transition from semimetallic to semiconducting characteristic. The electrical resistance behavior was investigated simultaneously. In this study, the electrical resistance behavior of Bi nanowire arrays with a wire diameter of 200 nm displayed an unexpected semiconducting characteristics which is likely to originate from the increased boundary scattering and increased grain size due to the polycrystalline structure of these nanowires. Besides providing a way for an atomically accurate size control of nanowire diameters, the SiO_2 coating can also act as a protective layer on the surface of the wires, against surface oxidation or mechanical damage. Such

factors are of importance, especially in the study of single free standing wires removed from the alumina template. Furthermore, the ALD of SiO₂ around thermoelectric nanowires could play a role for thermoelectric devices due to the lower thermal conductivity of SiO₂ than the alumina template.

Judging from the uniform nanowire growth and a good crystalline structure of the bismuth telluride nanowires obtained here, it was demonstrated that pulsed electrodeposition is a more effective method to obtain nanowires with tunable properties compared with other electrodeposition techniques (galvanostatic and potentiostatic electrodeposition). Furthermore, the duration of the off time in pulsed electrodeposition plays an important role in the control of composition, crystalline structure and the electrical conductivity of nanowires.

An annealing process at different temperatures was adopted in order to improve the crystalline structure of bismuth telluride nanowires, which should lead to an enhanced electrical conductivity. As the annealing temperature increased, the nanowires annealed at 150 °C showed an enhanced single crystalline structure. However, by a further temperature increase, the composition and the phase of nanowires were changed. Tellurium compounds showed a decreased concentration as the temperature increased to more than 150 °C, indicating a Bi-rich material. It was found that the Bi₂Te₃ phase of the nanowires (before annealing) transformed to Bi₄Te₅ (250 °C) and finally to Bi₄Te₃ (400 °C) as shown by XRD and selected area electron diffraction patterns (SAED).

The electrical conductivity of single crystalline bismuth telluride nanowire arrays and individual nanowires were measured. The electrical resistance behavior for bundles of bismuth telluride nanowires fabricated by pulsed electrodeposition increased as the temperature decreased, indicating a typical semiconducting behavior. In particular, an AFM-tip was used for the conductivity measurement at individual nanowires in AAO. In contrast to other methods which consisted of lithographical techniques for the metal contact to individual nanowires in a vacuum chamber, this method had advantages in terms of an easy and simple sample preparation as well as measurement. The electrical conductivity of individual nanowires measured by the AFM-tip method was in the range of 0.05~0.16 [$10^6 / (\Omega \cdot m)$], in agreement with previously reported values. In particular, the electrical conductivity of the pu 50 sample, which has a nearly single crystalline structure, is slightly better than other groups' value, including bulk and film structure. However, as the annealing process has been performed in an Ar atmosphere (non-oxygen atmospheres), the electrical conductivity of annealed nanowires could not be obtained due to the oxide layer which formed on the surface of the nanowires, which derive either from the annealing process itself or the sample exposure to the air.

The Seebeck coefficient of bismuth telluride nanowire arrays with and without heat treatment was measured at room temperature. The value was slightly increased (57 $\mu\text{V/K}$) as the annealed temperature increased up to 150 $^{\circ}\text{C}$ and significantly decreased after a 250 $^{\circ}\text{C}$ annealing. The reduction of the Seebeck coefficient was caused by a change of the composition (especially the Te compound reduction), leading to an increased Te deficiency. Finally the power factor of bismuth telluride nanowires was calculated based on the measured electrical conductivity and the Seebeck coefficient. The power factor of the nanowires fabricated by pulsed electrodeposition with 50 ms off time showed the highest value (**441.4 $\mu\text{W/m-K}^2$**), indicating an optimized carrier concentration at least under our experimental condition. The power factor and the Seebeck coefficient value of these nanowires were still lower than bulk Bi_2Te_3 and other, previously reported values due to the excess of bismuth in our samples. It will be required to find better experimental conditions for the optimized composition of nanowires. An annealing process is required to be performed in a Te ambient atmosphere with an overpressure of Te in order to prevent the evaporation of Te compounds with increasing annealing temperature. Additionally, the Seebeck coefficient can be improved by means of doping the optimized antimony or more Te compounds deposited as discussed in chapter 6. Assuming that the optimized antimony is doped into Bi-Te alloy nanowires, in principle, the power factor can increase around 7000 [$\mu\text{W/m-K}^2$], which is the highest value than others' reported values, expecting to the thermoelectric efficiency more than **1.0** at room temperature.

Finally, a synthesis method for bismuth telluride nanowires with rough surfaces was suggested for a reduction of the thermal conductivity. The thermal conductivity of nanowires should decrease because the rough surface of nanowires should induce secondary phonon scattering, thereby increasing phonon scattering. Unlike the nanowires fabricated in AAO prepared from a mild anodization, pulsed anodization which consisted of a combination of hard and mild anodization, produced a periodically modulated pore diameters. Therefore, after electrodeposition of nanowires in pulse-anodized AAO, nanowire with rough surfaces were obtained. In future work, it will be essential to measure the thermal conductivity of these nanowires.

For the measurement of the thermal conductivity of bulk nanowires and individual nanowires, the following methods are suggested for future research.

Very recently in the method developed by F. Völklein group^[S.1] the two ends of an individual nanowire have been electrically contacted. For preparation, the nanowire has been suspended prior on a SiO_2 -Si wafer. By photolithographic exposure of a

photoresist layer, sputter deposition and lift-off techniques the nanowires are electrically and thermally contacted. In particular, for thermal conductivity measurements non contacted parts of the nanowire are crossing a microchannel to minimize the heat transfer from the nanowire to the substrate. Therefore, the SiO₂ film below the nanowire is eliminated by reactive ion etching (RIE). During the etching process, the metal contact films serve as mask layers. Finally, the nanowire ends are in intimate thermal contact with the metallic contact films and are separated from the bulk Si wafer.

For thin film-like samples of nanowire arrays, the 3-Omega method is very reasonable but requires the deposition of an oxide layer (SiO₂ or Al₂O₃ etc.) by ALD on the nanowire arrays. However, as already mentioned, high porosity values (>70%) of a porous alumina template or a matrix replacement with reduced thermal conductivity are required to measure precisely the thermal conductivity of the composite structure and the nanowire material.

Bibliography

- [I. 1] P. Jena, R.L. Harnish, J. Fischer, and M.S. Dresselhaus, MRS Bul. **33** (2008) 824, “Global views on advancing renewable energies”
- [I. 2] G.S. Nolas, J. Sharp, and H.J. Goldsmid, Springer, New York (2001), “Thermoelectrics: basic principles and new materials development”
- [I. 3] G. Wiedemann, and R. Franz, Ann. Phys. **89** (1853) 497, “Ueber die Wärme-Leitungsfähigkeit der Metalle”
- [I. 4] D.M Rowe edited, CRC / Taylor & Francis, New York (2006), “Thermoelectric Handbook (Macro To Nano)”
- [I. 5] G. Chen, Phys. Rev. B, **57** (1998) 14958, "Thermal conductivity and ballistic-phonon transport in the cross-plane direction of superlattices”
- [I. 6] L.D. Hicks, and M.S. Dresselhaus, Phys. Rev. B, **47** (1993) 12727, “Effect of quantum-well structures on the thermoelectric figure of merit”
- [I. 7] M.S Dresselhaus, T. Koga, X. Sun, S.B. Cronin, K.L. Wang, and G. Chen, in 16th International Conference on Thermoelectrics: Proceedings, ICT’97, Dresden, Germany, edited by A. Heinrich, and J. Schumann, p. 12-20
- [I. 8] M.S. Dresselhaus, G. Dresselhaus, X. Sun, Z. Zhang, S.B Cronin, and T. Koga, phys. solid. stat., **41** (1999) 679, “Low-dimensional thermoelectric materials”
- [I. 9] M.E. Toimil, N. Chtanko, T.W. Cornelius, D. Dobrev, I. Enculescu, R.H. Blick, and R. Neumann, Nanotech. **15** (2004) S201, “Fabrication and contacting of single Bi nanowires”
- [I. 10] L.L. Zhao, M. Yosef, M. Steinhart, P. Goring, H. Hofmeister, U. Goesle, S. Schlecht, Angew. Chem. Int. Ed. **45** (2006) 311, “Porous Silicon and Alumina as Chemically Reactive Templates for the Synthesis of Tubes and Wires of SnSe, Sn, and SnO₂”
- [I. 11] T. Thurn-Albrecht, J. Schotter, G.A. Kastle, N. Emley, T. Shibauchi, L. Krusin-Elbaum, K. Gaurini, C.T. Black, M.T. Tuominen, and T.P. Russel, Science, **290** (2000) 2126, “Ultrahigh-Density Nanowire Arrays Grown in Self-Assembled Diblock Copolymer Templates”
- [I. 12] S.A. Sapp, B.B. Lakshmi, and C.R. Martin, Adv. Mat. **11** (1999) 402, “Template Synthesis of Bismuth Telluride Nanowires”
- [I. 13] Z.B. Zhang, D. Gekhtman, M.S. Dresselhaus, and J.Y. Ying, Chem. Mat., **11** (1999) 1659, “Processing and characterization of single-crystalline ultra fine bismuth nanowires”

- [I. 14] J. Heremans, C.M. Thrush, Y.M. Lin, Z. Zhang, M.S. Dresselhaus, and G.S. Mansfield, *Phys. Rev. B*, **61** (2000) 2921, “Bismuth nanowire arrays: Synthesis and galvanomagnetic properties”
- [I. 15] A. Giani, F. Pasca-Delanoy, A. Boyer, A. Foucaran, M. Gschwind, and P. Ancy, *Thin Solid Films*, **303** (1997) 1, “Elaboration of Bi_2Te_3 by metal organic chemical vapor deposition”
- [I. 16] Lopez-Otero, *Thin solid films*, **49** (1978) 3, “Hot wall epitaxy”
- [I. 17] H. Noro, K. Sato, and H. Kagechika, *J. Appl. Phys.*, **73** (1993) 1252, “The thermoelectric properties and crystallography of Bi-Sb-Te-Sn films grown by ion beam sputtering”
- [I. 18] E.J. Menke, M.A. Brown, Q. Li, J.C. Hemminger, and R.M Penner, *Langmuir*, **22** (2006) 10564, "Bismuth Telluride (Bi_2Te_3) nanowires: Synthesis by cyclic electrodeposition/stripping, Thinning by electrooxidation, and electrical power generation”
- [I. 19] I. Ohno, and S. Horuyama, *Bul. Japan. Inst. Met.* 30. p. 735
- [I. 20] J.M. Lee, S. Fahrangfar, J. Lee, L. Cagnon, R. Scholz, U. Gösele, and K. Nielsch, *Nanotech.* **36** (2008) 365701, “Tuning the crystallinity of thermoelectric Bi_2Te_3 nanowire arrays grown by pulsed electrodeposition”
- [I. 21] S. Li, M.S. Toprak, H.M.A. Soliman, J. Zhou, M. Muhammed, D. Platzek, and E. Muller, *Chem. Mat.* **18** (2006) 3627, "Fabrication of nanostructured thermoelectric bismuth telluride thick films by electrochemical deposition”
- [I. 22] C. Jin, X. Xiang, C. Jia, W. Liu, W. Cai, L. Yao, and X. Li, *J. Phys. Chem B*, **108** (2004) 1844, “Electrochemical fabrication of large-area, ordered Bi_2Te_3 Nanowire arrays”
- [I. 23] M. Dahnke, Diploma thesis, Institute of applied physics, University of Hamburg, (2009), “Wärmeleitfähigkeitsmessungen mit der 3 Omega-Methode”
- [I. 24] A.I. Hochbaum, R. Chen, R.D. Delgado, W. Liang, C. Erik, M. Najarian, A. Majumdar, and P. Yang, *Nature*, **451** (2008) 163, “Enhanced thermoelectric performance of rough silicon nanowires”
- [E. 1] H. Masuda, and K. Fukuda, *Science*, **268** (1995) 1466, “Ordered metal nanohole arrays made by a two-step replication of honeycomb structures of anodic alumina”
- [E. 2] F. Keller, M.S. Hunter, and D.L. Robinson, *J. Electrochem. Soc.*, **100** (1953) 411, “Structural features of oxide coatings on aluminum”
- [E. 3] R.C. Furneaux, W.R. Rigby, and A.P. Davidson, *Nature*, **337** (1989) 147, “The

formation of controlled-porosity membranes from anodically oxidized aluminium”

- [1. 1] M. Takahashi, Y. Katou, K. Nagata, and S. Furuta, *Thin solid films*, **240** (1994) 70, “The composition and conductivity of electrodeposited Bi-Te alloy films”
- [1. 2] M. Takahashi, Y. Oda, T. Ogino, and S. Furuta, *J. Electrochem. Soc.*, **140** (1993) 2550, “Electrodeposition of Bi-Te alloy films”
- [1. 3] P. Magri, C. Boulanger, and J.M. Lecuire, *J. Mat. Chem.* **6** (1996) 773, “Synthesis, properties and performances of electrodeposited bismuth telluride films”
- [1. 4] S. Michel, S. Diliberto, C. Boulanger, N. Stein, and J.M. Lecuire, *J. Crys. Growth*, **277** (2005) 274, “Galvanostatic and potentiostatic deposition of bismuth telluride films from nitric acid solution: effect of chemical and electrochemical parameters”
- [1. 5] S. Michel, S. Diliberto, C. Boulanger, and B. Bolle, *J. Cry. Growth*, **296** (2006) 227, “Effect of electrochemical deposition conditions on the crystallographic texture of bismuth telluride alloy”
- [1. 6] K. Tittes, A. Bund, W. Pileth, A. Bientien, S. Paschen, M. Plotner, H. Grafe, and W.J. Fischer, *J. Solid. Stat. Electrochem.*, **7** (2003) 714
- [1. 7] A.L. Prieto, M.S. Sander, M. Martin-Gonzalez, R. Gronsky, T. Sands, and A.M. Stacy, *JACS*, **123** (2001) 7160, “Electrodeposition of ordered Bi₂Te₃ nanowires”
- [1. 8] M.S. Sander, R. Gronsky, T. Sands, and A.M. Stacy, *Chem. Mat.*, **15** (2003) 335, “Structure of bismuth telluride nanowire arrays fabricated by electrodeposition into porous anodic alumina template”
- [1. 9] W.L. Wang, C.C. Wan, and Y.Y. Wang, *J. Phys. Chem. B*, **110** (2006) 12974, “Investigation of electrodeposition of Bi₂Te₃ nanowires into nanoporous alumina templates with a rotating electrode”
- [1. 10] L. Li, Y.W. Yang, X.H. Huang, G.H. Li, and L.D. Zhang, *Nanotech.*, **17** (2006) 1706, “Pulsed electrodeposition of single-crystalline Bi₂Te₃ nanowires”
- [1. 11] E.J. Menke, M.A. Brown, Q. Li, J.C. Hemminger, and R.M Penner, *Langmuir*, **22** (2006) 10564, "Bismuth Telluride (Bi₂Te₃) nanowires: Synthesis by cyclic electrodeposition/stripping, Thinning by electrooxidation, and electrical power generation”
- [1. 12] E.J. Menke, Q. Li, and R.M. Penner, *Nano Lett.* **4** (2004) 2009, “Bismuth Telluride (Bi₂Te₃) nanowires synthesized by cyclic electrodeposition/stripping coupled with step edge decoration”
- [1. 13] L. Li, Y. Zhang, G. Li, and L. Zhang, *Chem. Phys. Lett*, **378** (2003) 244, “A route to fabricate single crystalline Bi nanowire arrays with different diameters”

- [1. 14] Z. Zhang, D. Gekht, M.S. Dresselhaus, and J. Ying, *Chem. Mat.*, **11** (1999) 1659, “Processing and characterization of single-crystalline ultrafine bismuth nanowires”
- [1. 15] L. Li, G. Li, Y. Zhang, Y. Yang, and L. Zhang, *J. Phys. Chem. B*, **108** (2004) 19380, “Pulsed electrodeposition of large-area, ordered $\text{Bi}_{1-x}\text{Sb}_x$ nanowire arrays from aqueous solutions”
- [1. 16] Y. Peng, D.H. Quin, R.J. Zhou, and H.L. Li, *Mater. Sci. Eng. B*, **77** (2000) 246, “Bismuth quantum-wire arrays fabricated by electrodeposition in nanoporous anodic aluminum oxide and its structural properties”
- [1. 17] J. Wang, X. Wang, Q. Peng, and Y. Li, *Inorg. Chem.* **43** (2004) 7552, “Synthesis and characterization of Bismuth single-crystalline nanowires and nanospheres”
- [1. 18] M. Martin-Gonzalez, A.L. Prieto, R. Gronsky, T. Sands, and A.M. Stacy, *Adv. Mat.*, **15** (2003) 1003, “High-density 40 nm diameter Sb-rich $\text{Bi}_{2-x}\text{Sb}_x\text{Te}_3$ nanowire arrays”
- [1. 19] M. Martin-Gonzalez, G.J. Snyder, A.L. Prieto, R. Gronsky, T. Sands, and A.M. Stacy, *Nano Lett.*, **3** (2003) 973, “Direct electrodeposition of highly dense 50 nm $\text{Bi}_2\text{Te}_{3-y}\text{Se}_y$ nanowire arrays”
- [1. 20] K. Nielsch, F. Muller, A. Li, and U. Gösele, *Adv. Mat.*, **12** (2000) 582, “Uniform nickel deposition into ordered alumina pores by pulsed electrodeposition”
- [1. 21] K.H. Choi, H.S. Kim, and T.H. Lee, *J. Power. Sources*, **75** (1998) 230, “Electrode fabrication for proton exchange membrane fuel cell by pulsed electrodeposition”
- [1. 22] J.C. Puipe, and F. Leaman edited, *AESF, Florida*(1986), “Theory and practice of pulse plating”, J.C. Puipe, Chapter 1.
- [1. 23] H.Y. Cheh, *J. Electrochem. Soc.*, **118** (1971) 551, “Electrodeposition of gold by pulsed current”
- [1. 24] M. Pierre, B. Clotilde, and L. Jean-Marie, *J. Mat. Chem*, **6** (1996) 773, “Synthesis, properties and performances of electrodeposited bismuth telluride films”
- [1. 25] M. Martin-Gonzalez, L.P. Amy, R. Gronsky, T. Sands, and A.M. Stacy, *J. Electrochem. Soc.*, **149** (2002) C546, “Insights into the electrodeposition of Bi_2Te_3 ”
- [1. 26] A.M. Prieto, M.S. Sander, M.S. Martin-Gonzalez, R. Gronsky, T. Sands, and A.M. Stacy, *JACS*, **123** (2001) 7160, “Electrodeposition of ordered Bi_2Te_3 nanowire arrays”
- [1. 27] J.C. Puipe, and F. Leaman edited, *AESF, Florida* (1986),

- “Theory and practice of pulse plating”, D. Landolt, Chapter 5.
- [1. 28] Y. Miyazaki, and T. Kajitani, *J. Cry. Growth*, **229** (2001) 542, “Preparation of Bi₂Te₃ film by electrodeposition”
- [1. 29] S.H. Kim, H.J. Sohn, Y.C. Joo, Y.W. Kim, T.H. Yim, H.Y. Lee, and T. Kang, *Surf. Coat. Tech.* **199** (2005) 43, “Effect of saccharin addition on the microstructure of electrodeposited Fe-36wt% Ni alloy”
- [1. 30] J. Dheepa, R. Sathyamoorthy, S. Velumani, A. Subbarayan, K. Natarajan and P. J. Sebastian, *Solar Energy Mat. & Solar Cells*, **81** (2004) 305, “Electrical resistivity of thermally evaporated bismuth telluride films”
- [1. 31] J.C. Puipe, and F. Leaman edited, AESF, Florida (1986),
“Theory and practice of pulse plating”, J.C. Puipe, Chapter 3.
- [1. 32] L. Domnikov, *Metal Finishing*, 61 (1963) 96
- [2. 1] M.S Dresselhaus, and J.P. Heremans, “Recent developments in low-dimensional thermoelectric materials”, In *Thermoelectric handbook: Macro To Nano*, D.M Rowe ed. CRC Press, Boca Raton, FL (2004), Chapter. 39.
- [2. 2] M.S. Dresselhaus, G. Chen, M.Y. Tang, R. Yang, H.H. Lee, D. Wang, Z. Ren, J.P. Fleurial, and P. Gogna, *Adv. Mat.*, **19** (2007) 1043, “New directions for low dimensional thermoelectric materials”
- [2. 3] C.F. Gallo, B.S. Chandrasekhar, and P.H. Sutter, *J. Appl. Phys.*, **34** (1963) 144, “Transport properties of Bi single crystals”
- [2. 4] J.P. Issi, “Thermoelectric properties of the group V semimetals”, In *Thermoelectric handbook: Macro To Nano*, D.M Rowe ed. CRC Press, Boca Raton, FL (2004), Chapter. 30.
- [2. 5] L.D. Hicks, T.C. Harman, X. Sun, and M.S. Dresselhaus, *Appl. Phys. Lett.*, **63** (1993) 3230, “Use of quantum-well superlattices to obtain a high figure of merit from nonconventional thermoelectric material”
- [2. 6] T. W. Cornelius, M. E. Toimil-Molares, R. Neumann, G. Fashsold, R. Lovrincic, A. Pucci and S. Karim, *Appl. Phys. Lett.* **88** (2006) 103114., “Quantum size effects manifest in infrared spectra of single bismuth nanowires”
- [2. 7] S. Farhangfar, *Phys. Rev. B* **74** (2006) 205318,
“Quantum size effects in a one-dimensional semimetal”
- [2. 8] V. B. Sandormirskiĭ, *Sov. Phys. JETP* **25** (1967) 101
- [2. 9] H. Kimin, F.Y. Yang, K. Liu, D.H. Reich, P.C. Searson, C.L. Chien, F.F. Balakirev, and G.S. Boebinger, *J. Appl. Phys.*, **85** (1999) 6184, “Giant positive magnetoresistance of Bi nanowire arrays in high magnetic fields”

- [2. 10] Y. M. Lin, X. Sun, and M. S. Dresselhaus, *Phys. Rev. B* **62** (2000) 4610, “Theoretical investigation of thermoelectric transport properties of cylindrical Bi Nanowires”
- [2. 11] W. S. Boyle and F. K. Rodgers, *Phys. Rev. Lett.* **2** (1959) 338, “De Haas-van Alphen Type Oscillations in the Infrared Transmission of Bismuth”
- [2. 12] S. Takoka and K. Murase, *J. Phys. Soc. Jpn.* **54** (1985) 2250.
- [2. 13] J. Heremans, C. M. Thrush, Y.-M. Lin, S. Cronin, Z. Zhang, M. S. Dresselhaus and J. F. Mansfield, *Phys. Rev. B.* **61** (2000) 2921., “Synthesis and galvanomagnetic properties bismuth nanowire arrays”
- [2. 14] J. Heremans and C. M. Thrush, *Phys. Rev. B.* **59** (1999) 12579., “Thermoelectric power of bismuth nanowires”
- [2. 15] T. Suntola and J. Hyvarinen, *Annu. Rev. Mater. Sci.* **15** (1985) 177., “Atomic layer epitaxy”
- [2. 16] S. M. George, A. W. Ott, and J. W. Klaus, *J. Phys. Chem.* **100** (1996) 13121, “Surface chemistry for atomic layer growth”
- [2. 17] D. Schiferl, and C.S. Barrett, *J. Appl. Crystallogr.*, **2** (1969) 30, “The crystal structure of arsenic at 4.2, 78 and 299K”
- [2. 18] S.B Cronin, Dissertation, Dept. Physics, MIT (2002), “Electronic properties of Bi nanowires”
- [2. 19] J. Heremans, and O.P. Hansen, *J. Phys. C*, **12** (1979) 3483, “Influence of non-parabolicity on intravalley electron-phonon scattering; the case of bismuth”
- [2. 20] Y.M. Lin, X. Sun, and M.S. Dresselhaus, *Phys. Rev. B*, **62** (2000) 4610, “Theoretical investigation of thermoelectric transport properties of cylindrical Bi nanowires”
- [2. 21] Y.M. Lin, Dissertation, Dept. electrical engineering and computer science, MIT (2000), “Fabrication, characterization and theoretical modeling of Te-doped Bi nanowire systems for thermoelectric application”
- [2. 22] M.P. Vecchi, and M.S. Dresselhaus, *Phys. Rev. B.*, **10** (1974) 771, “Temperature dependence of the band parameters of bismuth”
- [2. 23] C.F. Gallo, B.S. Chandrasekhar, and P.H. Sutter, *J. Appl. Phys.*, **34** (1963) 144, “Transport Properties of Bismuth Single Crystals”
- [2. 24] J. Heremans, C. M. Thrush, Y.-M. Lin, S. Cronin, Z. Zhang, M. S. Dresselhaus and J. F. Mansfield, *Phys. Rev. B.* **61** (2000) 2921., “Synthesis and galvanomagnetic properties Bismuth nanowire arrays”
- [2. 25] S. Lin-droos, T. Kanninen, and M. Leskela, *Appl. Surf. Sci.*, **75** (1994) 70, “Growth of ZnS thin films by liquid-phase atomic layer epitaxy”

- [2. 26] J.L. Stickney, *Electroanal. Chem*, **21** (1999) 75
- [2. 27] A.M. Hoyas, J. Schuhmacher, D. Shamyryan, J. Waeterloos, W. Besling, J.P. Celis, and K. Maex, *J. Appl. Phys.*, **95** (2004) 381, "Growth and characterization of atomic layer deposited $WC_{0.7}N_{0.3}$ on polymer films"
- [2. 28] T.S. Suntola, A.J. Pakkala, and S.G. Lindfors, U.S. Patent, No. 4389973
- [2. 29] S.I. Kol'tsov, *Zh. Prikl. Khim, J. Appl. Chem. USSR.*, **42** (1969) 975
- [2. 30] B.S. Lim, A. Rahtu, and R.G. Gordon, *Nat. Mater.*, **2** (2003) 749, "Atomic layer deposition of transition metals"
- [2. 31] R. Matero, A. Rahtu, M. Ritala, M. Leskela, and T. Sajavaara, *Thin solid films*, **368** (2000) 1, "Effect of water dose on the atomic layer deposition rate of oxide thin films"
- [2. 32] F.P. Incropera, D.P. Dewitt, T.L. Bergman, and A.S. Lavine, 5th ed, "Introduction to heat transfer", John Willey&Sons, (2007) NJ. USA., Appendix A, Table A.6
- [2. 33] W.Y. Shim, J.H. Ham, K.I. Lee, W.Y. Jeung, M. Johnson, W.Y. Lee, *Nano. Lett.*, **9** (2009) 18, "On-Film Formation of Bi Nanowires with Extraordinary Electron Mobility"
- [2. 34] J. Bachmann, R. Zierold, Y.J. Chong, R. Hauert, C. Sturm, R. Schmidt-Grund, B. Rheinlander, M. Grundmann, U. Goesle, and K. Nielsch, *Angew. Chem. Int. Ed.* **47** (2008) 6177, "A Practical, Self-Catalytic, Atomic Layer Deposition of Silicon Dioxide"
- [2. 35] R.L. Puurunen, *J. Appl. Phys.*, **97** (2005) 121301, "Surface chemistry of atomic layer deposition: A case study for the trimethylaluminum / water process"
- [2. 36] Z. Ye, H. Zhang, H. Liu, W. Wu and Z. Luo, *Physica B*, **403** (2008) 1529, "Evidence for superconductivity in single crystalline Bi nanowires"
- [3. 1] W. Wang, X. Lu, T. Zhang, G. Zhang, W. Jiang, and X. Li, *JACS*, **129** (2007) 6702, " Bi_2Te_3/Te multiple heterostructure nanowire arrays formed by confined precipitation"
- [3. 2] I. Barin, O. Knacke, Springer, Berlin-Heidelberg-NewYork; stahleisen Dusseldorf (1976), p. 738, "Thermodynamical properties of inorganic substances"
- [3. 3] E.J. Menke, M.A. Brown, Q. Li, J.C. Hemminger, and R.M Penner, *Langmuir*, **22** (2006) 10564, "Bismuth Telluride (Bi_2Te_3) nanowires: Synthesis by cyclic electrodeposition/stripping, Thinning by electrooxidation, and electrical power generation"
- [3. 4] H. Bando, K. Koizumi, Y. Oikawa, K. Daikohara, V.A. Kulbachinskii,

H.J. Ozaki, *J. Phys. Condens. Matter*, **12** (2000) 5607, “The time-dependent process of oxidation of the surface of Bi₂Te₃ studied by x-ray photoelectron spectroscopy”

[3. 5] NIST Electron Inelastic-Mean-Free-Path Database, version 1.1; Powell, C. J., Jablonski, A., Eds.; National Institute of Standards and Technology: Gaithersburg, MD (2001).

[4. 1] V. B. Sandomirskii, *Sov. Phys. JETP* **25**, (1967) 101

[4. 2] S. Farhangfar, *Phys. Rev. B* **74** (2006) 205318,
“Quantum size effects in a one-dimensional semimetal”

[4. 3] S. Farhangfar, *Phys. Rev. B* **76** (2007) 205437,
“Quantum size effects in solitary wires of bismuth”

[4. 4] M. R. Balck, Y.M. Lin, S.B.Cronin, O.Rabin, and M.S. Dresselhaus, *Phys. Rev. B* **65** (2002) 195417, “Infrared absorption in bismuth nanowires resulting from quantum confinement”

[4. 5] http://science.widener.edu/svb/ftir/ir_co2.html

[4. 6] M. R. Black, Dissertation, Dept. Electrical Engineering and Computer Science, MIT (2003), “The optical properties of bismuth nanowires”

[5. 1] M.P. Singh, and C.M. Bhandari, *Solid. State. Comm.*, **127** (2003) 649,
“Thermoelectric properties of bismuth telluride quantum wire”

[5. 2] J.R. Drabble, R.D. Grove, and R. Wolfe, *Proc. Phys. Soc., London*,
71 (1958) 430

[5. 3] W. Wang, F. Jia, Q. Huang, and J. Zhang, *Microelectron, Eng.* **77** (2005) 223,
“A new type of low power thermoelectric micro-generator fabricated by nanowire arrays thermoelectric material”

[5. 4] D.L. Greenaway, and G.J. Harbeke, *Phys. Chem. Solids*, **26** (1965) 1585,
“Band structure of bismuth telluride, bismuth selenide and their respective alloys”

[5. 5] Z. Zhang, Dissertation, Dept. Physics, MIT (1999),
“Fabrication, characterization and transport properties of bismuth nanowire systems”

[5. 6] N. Garcia, Y.H. Kao, and M. Strongin, *Phys. Rev. B.*, **5** (1972) 2029,
“Galvanomagnetic Studies of Bismuth Films in the Quantum-Size-Effect Region”

[5. 7] S. Farhangfar, *Phys. Rev. B.*, **76** (2007) 205437, “Quantum size effects in solitary wires of bismuth”

[5. 8] S.B. Cronin, Dissertation, Dept. Physics, MIT (2002), “Electronic properties of Bi nanowire arrays”

[5. 9] A.L. Schmitt, J.M. Higgins, and S. Jin, *Nano. Lett.*, **8** (2008) 810,

“Chemical synthesis and magnetotransport of magnetic semiconducting $\text{Fe}_{1-x}\text{Co}_x\text{Si}$ alloy nanowires”

[5. 10] F. Zhou, J. Szczech, M.T. Petters, A.L. Mare, and S. Jin. *Nano. Lett.*, **7** (2007) 1649, “Deterioration of transport properties in chromium disilicide nanowires via combined thermoelectric and characterization”

[5. 11] F.H. Ramirez, A. Tarancon, O. Casals, J. Rodriguez, A.R. Rodriguez, J.R. Morante, S. Barth, S. Mathur, T.Y. Choi, D. Poulikakaos, V. Callegari, and P.M. Nellen, *Nanotech.*, **17** (2006) 5577, “Fabrication and electrical characterization of circuits based on individual tin oxide nanowires”

[5. 12] J.D. Prades, R.J. Diaz, F.H. Ramirez, L.F. Romero, T. Andreu, A. Cirera, A.R. Rodriguez, A. Cornet, J.R. Morante, S. Barth, and S. Mathur, *J. Phys. Chem. C*, **112** (2008) 14639, “Toward a systematic understanding of photodetectors based on individual metal oxide nanowires”

[5. 13] M.N. Ou, T.J. Yang, S.R. Harutyunyan, .Y.Y. Chen, C.D. Chen, and S.J. Lai, *Appl. Phys. Lett.*, **92** (2008) 063101, “Electrical and thermal transport in single nickel nanowire”

[5. 14] L. Shi, C. Yu, J. Zhou, *J. Phys.Chem. B*, **109** (2005) 22102, “Thermal characterization and sensor applications of one-dimensional nanostructures employing micro-electromechanical systems”

[5. 15] Landolt-Bornstein-Group III Condensed Matter, Numerical data and functional relationships in science and technology nontetrahedrally bonded elements and binary compounds (1985), I10.1007/10681727_962

[6. 1] J. Zhou, Dissertation, Dept. Mechanical Engineering, Univ. Texas, USA, (2005), “Thermal and thermoelectric transport measurement of one-dimensional nanostructure”

[6. 2] A.F. Ioffe, and L.S. Stil’bans, *Rep. Prog. Phys.*, **22** (1959) 167, “Physical problems of thermoelectricity”

[6. 3] G.S. Nolas, J. Sharp, and H.J. Goldsmid, Springer, Berlin, (2001) “Thermoelectrics: Basic principles and new materials developments”

[6. 4] H.J. Goldsmid, Butler & Tanner Ltd, Frome and London, (1960), “Applications of thermoelectricity”

[6. 5] Y.M. Lin, O. Rabin, S.B. Cronin, J.Y. Ying and M.S. Dresselhaus, *Appl. Phys. Lett.*, **81** (2002) 2403, “Semimetal–semiconductor transition in $\text{Bi}_{1-x}\text{Sb}_x$ alloy nanowires and their thermoelectric properties”

[6. 6] L. Shi, C. Yu, J. Zhou, *J. Phys. Chem B.*, **109** (2005) 22102,

"Thermal characterization and sensor applications of one-dimensional nanostructures employing micro-electromechanical systems"

- [6. 7] J.P. Fleurial, L. Gailliard, R. Triboulet, H. Scherrer, S. Scherrer, *J. Phys. Chem. Sol.*, **49** (1988) 1247, "Thermal properties of high quality single crystals of bismuth telluride-Part 1: Experimental characterization"
- [6. 8] D.H. Kim, and G.H. Lee, *Mat. Sci. Eng. B.*, **131** (2006) 106, "Effect of rapid annealing on thermoelectric properties of bismuth telluride films grown by co-sputtering"
- [6. 9] B. Poudel, Q. Hao, Y. Ma, Y. Lan, A. Minnisch, B. Yu, X. Yan, D. Wang, A. Muto, D. Vashaee, X. Chen, J. Liu, M.S. Dresselhaus, G. Chen, and Z. Ren, *Science*, **320** (2008) 634, "High-thermoelectric performance of nanostructured bismuth antimony telluride bulk alloys"
- [7. 1] J. Zou, and A. Balandin, *J. Appl. Phys.*, **89** (2001) 2932, "Phonon heat conduction in as semiconductor nanowire"
- [7. 2] S. Saha, L. Shi, and R. Prasher, *Proc. ASME. Int. Mech. Eng. Congr. Exp. No. 156681* 1-5, "Monte carlo simulation of phonon backscattering in a nanowire"
- [7. 3] A. L. Moore, S. K. Saha, R. S. Prasher, L. Shi, *Appl. Phys. Lett.*, **93** (2008) 083112, "Phonon backscattering and thermal conductivity suppression in sawtooth nanowires"
- [7. 4] W. Lee, K. Schwirn, M. Steinhart, E. Pippel, R. Scholz, and U. Gösele, *Nature Materials*, **3** (2008) 234, "Structural engineering of nanoporous anodic aluminium oxide by pulse anodization of aluminium"
- [7. 5] W. Lee, R. Ji, U. Gösele, and K. Nielsch, *Nature Materials*, **5** (2006) 741, "Fast fabrication of long-range ordered porous alumina membranes by hard anodization"
- [7. 6] W. Lee, U. Gösele, and K. Nielsch, *Nanotech.*, **18** (2007) 475713, "Self-ordering behavior of nanoporous anodic aluminum oxide (AAO) in malonic acid anodization"
- [7. 7] S.Z. Chou, K. Wada, S. Inoue, M. Isogai, and A. Yasumori, *Adv. Mat.* **17** (2005) 2115, "Fabrication of ideally ordered nanoporous alumina films and intergrated alumina nanotube arrays by high field anodization"
- [S. 1] F. Völklein, H. Reith, T.W. Cornelius, M. Rauber, and R. Neumann, submitted to *Nanotech.*, "Experimental investigation of thermal conductivity and Wiedemann-Franz law on single metallic nanowires"

Lebenslauf

Mr. Jongmin Lee

Max-Planck-Institut für Mikrostrukturphysik

Weinberg 2, D-06120 Halle, Germany

e-mail: jmlee@mpi-halle.de

Geburtsdatum:

23. Jan. 1977, Seoul, Südkorea.

Ausbildung:

Mär. 2006 ~ Present

Max-Planck-Institut für Mikrostrukturphysik and Martin-Luther Universität (Halle/Wittenberg), Halle, Germany

Zentrum für Ingenieurwissenschaften

(Dissertation: Thermoelectric Bi related nanowires based on Anodic Aluminum Oxide)

(Betreuer: Prof. Dr. Ulrich Gösele und Prof. Dr. Kornelius Nielsch)

Mär. 2004 ~ Feb. 2006

Inha Universität, Incheon, Südkorea

Diplom für Chemieingenieurwesen

(Master: "Study on the properties of the solid electrolyte and anode in the all-solid-state microbattery")

(Betreuer: Prof. Y. Tak and Prof. Y.S. Yoon)

Mär. 1997 ~ Feb. 2004

Inha Universität, Incheon, Südkorea

Bachelor für Chemieingenieurwesen (Betreuer: Prof. D. Park)

Berufserfahrung

Sep. 2003 ~ Dez. 2004

Nanomaterial Research Center,

Korea Institute of Science and Technology (KIST), Seoul, Südkorea

Halle, den 15. Apr. 2009

Lee Jongmin

Acknowledgements

First of all, I would like to express my appreciation to my supervisors Prof. Ulich Gösele (Director in MPI-Halle) and Prof. Kornelius Nielsch (University of Hamburg), for helpful and fruitful discussions and their manifold support (financially and careful reading the manuscript etc.) and encouragement throughout the years.

Especially, I would like to appreciate to Prof. Lee Jaeyoung (Gwangju Institute of Science and Technology, Korea) and Prof. Choi Jinsub (Inha University, Korea) for their introduction, motivation and encouragement to study a Ph. D in Germany.

Mr. William Töllner (University of Hamburg), Mr. Renbin Yang (MPI-Halle), Dr. Tomohiro Shimizu and Dr. Mato Knez are thanked for their friendship and enlightening discussions.

I am greatly indebted to all the colleagues who have contributed to this thesis. I would like to thank very much:

- Dr. Shadyar Fahrangfar (University of Hamburg) for his fruitful discussions about the general electrical properties and optical properties of nanowires,
- Dr. Laurent Cagnon (CNRS, France) for his Seebeck coefficient measurement of nanowires,
- Dr. Marin Alexe and Dr. Kim Yoonseok (MPI-Halle) for their electrical resistance measurement of nanowires and individual nanowire and fruitful discussions,
- Dr. Jullien Bachmann (University of Hamburg) for his fruitful discussions about ALD process and its derivative chemical reactions,
- Dr. Roland Scholz (MPI-Halle) for his fruitful discussions about TEM analysis,
- Dr. Fernando Hernandez (University of Barcellona) for his electrical resistance measurement of individual Bi₂Te₃ nanowire,
- Mr. Kim Dongsik (MPI-Halle) for his annealing process of nanowires,
- Mrs. Sigrid Hopfe and Claudia Münx (MPI-Halle) for their ion-milling process,
- Dr. Monika Kaempfe (MPI-Halle) for her kind considerations about living in Halle as a coordinator of International Max-Planck Research School (IMPRS).

In addition I would like to thank my family for their dedicated love and continuous supports. Finally, I would like to thank my wife, Gwangsun Park for all her love and supports.